Investigation of Post-Processing Resistivity Modification Methods for HV-CMOS Pixel Detectors

William Holmkvist

A thesis submitted for the degree of Doctor of Philosophy

Physics Department, Lancaster University

May 2022

Declaration of Authorship

I hereby declare that the this thesis and the work presented in it are my own, and has not been submitted elsewhere for any reward of degree. Where the published work of others have been used or quoted, they have been acknowledged and the source has always been given.

May 31, 2022
William Holmkvist

Abstract

Silicon detectors plays a key-role in the measurement of particle trajectories in current particle collision experiments. Future colliding experiments will impose even larger demands on the performance of the detectors. To meet these demands, while simultaneously keeping costs low, monolithic active silicon sensors using HV-CMOS technology are currently investigated. While showing good promise, many semiconductor foundries do not allow for custom substrate resistivity, making it interesting to investigate whether standard substrate HV-CMOS sensors are a viable option for future high energy particle detectors.

To this end, this thesis presents a study on how the charge collection and effective doping concentration are affected by hadron irradiation in HV-CMOS detector prototypes. The investigated prototypes were produced at two different foundries, Austria Micro Systems and LFoundry, and were irradiated with either protons or reactor neutrons. Edge-TCT, using pulsed IR light injection, was the main tool of investigation. Proton irradiated samples were found to perform significantly better after fluences of $5 \cdot 10^{14}$ n_{eq}/cm^2. The neutron irradiated samples had a significant reduction charge collection in spite of an increased depletion region after 10^{15} n_{eq}/cm^2. Additionally, all samples showed a decrease in charge collection in the fluence region 10^{13} - 10^{14} n_{eq}/cm^2. Following these, low-resistivity HV-CMOS detectors might not be optimal for some particle collider environments, but could be of use for prototyping with foundries not offering custom resistivity substrates.

Additionally, as an attempt to improve performance Thermal Donor introduction was investigated as a method to increase the active region in low resistivity HV-CMOS sensors. Samples were annealed at 450 °C at increasing time intervals, and measured using edge-TCT. Introduction rates were found to deviate greatly from estimated values, and Thermal Donor introduction was ultimately concluded not viable as a method to improve detector performance.

Acknowledgements

First and foremost I would like to thank my supervisor Daniel Muenstermann for providing me with this opportunity, guidance on many interesting topics within the pixel detector community and for the continuous support throughout this journey.

I am deeply grateful to Michael Moll for having me in his group during my two years at CERN and for all the invaluable guidance within the field of silicon detectors he offered. Further I want to thank Marcos Fernández Garcia for helping me both with instructing me on data collection and analysis using the TCT system. Thanks to his help, the obstacles during this journey were reduced tenfold. A special thank you is also given to Matteo Centis Vignali for being an excellent office mate at CERN and giving a lot of valuable insights on silicon. Additionally, I want to show my appreciation to Yana Grumiskaya and Isidre Mateu for helping me navigate setups in the SSD lab, and also with data taking. I also want to extend a heartfelt thank you to the rest of the SSD team not already mentioned, for all the valuable discussions, cake sessions and memorable activities. My time at CERN would have been a bit more grey without all of you.

I need to thank all the assistance I received from the ED/DT bond lab, and in particular Florentina Manolescu, for all excellent bonding and patience with my not too seldom last-minute requests. Likewise, I want to extend much thanks to Stephen Holt, and his team in the electrical workshop at the Physics department, and Ian Mercer in the mechanical workshop for all the crucial assistance during installation and troubleshooting of experimental setups. Many thanks goes to Gregor Kramberger in his support during troubleshooting of the particulars TCT setup and valuable insights to measurement and detector physics in general.

Furthermore, I must thank Igor Mandic and Eva Vilella Figueras for insightful comments on some of the results presented in this work, and interesting collaboration meetings. This also extends to the wider RD50-collaboration for all the interesting workshops throughout these years.

I also greatly appreciate all the assistance Deborah Dunne and Lynne Haley have given for making all the paperwork very smooth.

Massive thanks to Owen Colgrove for being awesome. Also massive thanks to 161, José Luis Muños, Daniel Bjrkman, Branko Popovic, Eino Juhani Oltedal and the rest of the Geneva gang for all the shenanigans. Life would not be the same without all our shared experiences.

Also, many thanks to Dave Shaw, Steven Williams, Ben Whitmore, Neža Ribarič-Lasnik, Amy Tee, and all the other garduate students and staff in the particle physics group for making my time in Lancaster a delight, through many a board game and pub nights.

Ola Kenji Forslund and Johan Widenkvist, you guys!

Lastly, making it all the way here would not have been possible without my parents and siblings, who has given me invaluable support during some of my struggles, which for I am forever grateful.

Contents

List of Figures

List of Tables

Chapter 1

Introduction

Particle Physics is the pursuit of understanding the universe through the study of the particles that constitute matter and radiation. In recent years this is mainly done through colliding particles at high energies and studying the by-products of these collisions. So far, all our efforts to understand the world around us on a fundamental level has accumulated to what is known as the Standard Model. This model describes 12 fermions constituting all matter, 4 Gauge Bosons mediating the known forces excluding gravity and the newly discovered Higgs Boson, related to the Higgs mechanism that explains how the fundamental particles have mass. Currently the largest particle collider, LHC[1] situated underground beneath CERN on the outskirts of Geneva, is accelerating protons up to 6.5 TeV to accommodate for a total collision energy of 13 TeV. To achieve this magnitude of energy, the acceleration process starts with a gas cylinder of hydrogen. The hydrogen atoms are first passed through a strong electric field to strip them of their electrons to create bare protons, which are then accelerated through a linear accelerator reaching 50 MeV. The protons are then fed in turn to three successively larger synchrotrons, the booster, PS[2], and the SPS[3], accelerated incrementally at each step to finally reach an energy of 450 GeV before they are injected into the LHC. The LHC divides the particle current into two opposite directions, clockwise and anti-clockwise, along the 27 km circumference. The LHC incorporates four collision points where the two beams are brought together to collide the opposite travelling protons. At normal operations, LHC is designed to have a bunchcrossing every 25 ns, yielding an inelastic collision rate at nominal luminosity of $6 \times 10^8 s^{-1}$. This magnitude of collision rate

---

[1] Large Hadron Collider

[2] Proton Syncrotron

[3] Super Proton Syncrotron

puts significant demands on the performance of the detectors used at the LHC. The two largest detectors are CMS[4] and ATLAS[5], both being general-purpose physics detectors that were mainly designed with the discovery of the Higgs Boson in mind. The ATLAS Experiment have an onion like structure, with different sub-detectors built in layers, each with its own purpose. Sharing similarities, only the ATLAS Experiment will be described briefly below.

A major point of interest and driver during the design phase of the ATLAS detector was to investigate the Higgs mechanism, proposed by Peter Higgs and several other physicists in the 1960s. This mechanism implied the existence of a then undiscovered Higgs Boson, and with this in mind the ATLAS detector was optimised to be sensitive for a large range of possible Higgs Boson masses. Apart from the search for the Higgs Boson, other important points of interest were supersymmetric particles, precision measurements of the top quark, searches for heavy W-and Z-like particles, and CP-violation in B-decay [8]. As a general system overview, the ATLAS detector can be divided into three sub-detector systems, the innermost being the Inner Tracker, followed by the calorimeters, and lastly the Muon Spectrometer encapsulating the whole detector. In addition to this, ATLAS incorporates a two-part magnet system consisting of a solenoid magnet encapsulating the Inner Tracker and toroidal magnet system sitting outside the calorimeters, but within the muon spectrometer. Figure 1.1 below is included to give a clear view of the ATLAS detector described here. These systems together can detect a large range of possible signatures for new physics, an important factor considering the high luminosity.

The Muon Spectrometer consists of four individual subsystems totalling over 1.2 million readout channels that together with the magnetic field produced by the toroidal magnets functions like a larger version of the Inner Tracker, described below, to measure the momentum of muons. While muon measurements are essential for discovering certain phenomena and are also well suited for the study of certain physics beyond the standard model [109], a major reason for the intricacy and granularity of the muon spectrometer is due to the $H \to ZZ* \to 4\ell$ decay mode. Here 4ℓ represents 4 leptons, either electrons or muons, and this decay mode provided good sensitivity over a large energy range while searching for the Higgs Boson signifying the importance of the muon spectrometer [1, 109]. Inside the muon spectrometer and the toroidal magnet system sits the calorimeter system, divided into two parts, the outer being the hadronic calorimeter and the inner

---

[4] Compact Muon Solenoid

[5] A Toroidal LHC ApparatuS

being the electromagnetic calorimeter. This system extends up to $|\eta| = 4.9$[6] to achieve efficient missing energy reconstruction and accurate jet energy measurements. These properties are necessary for the studies of missing energy signatures for BSM[7] physics and crucial for the study of the $H \rightarrow \gamma\gamma$ decay.

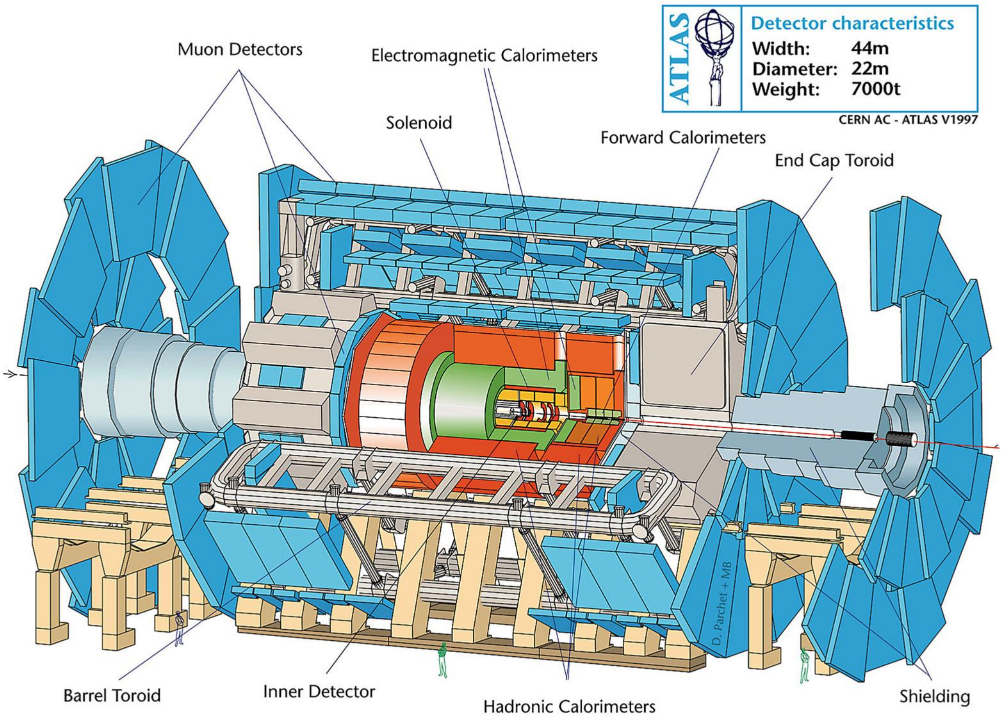

Figure 1.0.1: Overview of the ATLAS detector layout. In *blue*: the muon detector system, *grey*: the toroidal magnet system, *red*: the hadronic calorimeters, *green*: the electromagnetic calorimeter, and in *orange* the solenoid magnet. From [20]

Directly inside of the electromagnetic calorimeter sits the solenoid magnet, producing a magnetic field of 2 Tesla for the Inner Tracker, which is situated inside the magnet. The Inner Tracker is a high-resolution position tracker measuring the momentum of charged particles using three separate detector systems. High resolution and readout speed is a crucial function of the inner detector to keep the single channel occupancy low in the high collision rate environment of the LHC. The track reconstruction performed by the Inner Tracker, together with the other two detector systems, is used for electron, muon and photon recognition. In addition to this, the Inner Tracker was also designed to tag long-lived particles which is a signature of b-quark production. This is interesting with regards to the $H \rightarrow b\bar{b}$ decay channel and the study of CP-violation in the B-system [27].

---

[6] Pseudorapidity, a spatial coordinate describing the angle relative to the beam axis, defined as $-ln(tan(\theta/2))$, where θ is the angle to the beam pipe.

[7] Beyond Standard Model

While the CMS detector experiment utilises a pure silicon-based tracker system, the outer most detector system in the ATLAS Inner Tracker is the TRT[8], which is a combination of a transition radiation detector and a straw tracker. While silicon-based trackers give superior granularity, the TRT provides a large number of tracking points with less material and cost per point [8]. The barrel part, consisting of 4 mm thick by 144 cm long straws with a 30 μm gold wire in the center, achieves a spatial resolution of 200 μm in $R\phi$[9]. The space between the straws are interleaved with polymer fibers (foils in the end caps) to create transition radiation, soft x-rays, and the straws themselves are filled with a xenon gas mixture for a large x-ray cross section. Inside the TRT is the SCT[10], which is a silicon microstrip tracker covering 60 m^2 in four barrel layers and 18 planar end-cap disks. The SCT contains 4088 detector modules, each with four single sided silicon strip sensors. Each sensor contains 768 strips with a 80 μm pitch (57 - 94 μm in the end cap), achieving an accuracy up to 17 μm orthogonal to the strips.

Closest to the beamline lies the pixel detector. Due to its positioning just outside the beam pipe, the pixel detector is required to provide extremely high spatial resolution combined with fast readout electronics to reduce pile-up of tracks. Similarly to the SCT, the pixel detector is made from silicon sensors, but instead of strips, each module contains 46080 pixels. The sensitive region of each pixel is achieved by 50 μm by 400 μm n-implants in a 250 μm thick n-doped bulk. Due to the high density of the active regions on the chip, wire bonding is not an alternative for connecting the chip and bump bonding is used to directly connect each sensor pixel to a readout channel on a corresponding pixel readout chip. This greatly increases the cost of conventional pixel modules making them unsuitable for larger areas, in contrast to the SCT. While the spatial resolution and readout time were the main focus during the pixel design, great effort had to be put into ensuring the radiation hardness of the detector, due to the proximity to the beamline. Float zone silicon enriched with oxygen through diffusion was shown to reduce some effects caused by the high radiation background [67]. Although measures were taken to increase robustness of the original pixel detector, inevitably some pixels in the innermost layers were bound to fail reducing accuracy of the tracking performance. This, together with a few other reasons [7], led to the installation of a fourth pixel layer, IBL[11], inside the current pixel detector during the long shutdown of LHC in 2014. Compared to the original pixel detector, which uses conventional planar pixels, the IBL included so-

---

[8] Transition Radiation Tracker

[9] Perpendicular to the beam pipe.

[10] SemiConductor Tracker

[11] Insertable B-Layer

called 3D silicon sensors as well, which have shown to have superior radiation robustness over conventional planar pixels, making them suitable for more extreme environments. A drawback for 3D sensors currently is the complexity of production and the related increased production cost compared to conventional planar pixels.

Following the discovery of the Higgs Boson, ATLAS has shifted the focus to studying hints of supersymmetry and dark matter, such as looking for WIMPs[12], further precision measurements of the Higgs Boson and other physical phenomena. Many of these searches rely on looking for rare decay events, imposing a time limit on how quickly discoveries can be confirmed with a 5 sigma confidence with the current luminosity of LHC. To mitigate this time problem, the LHC is set to be upgraded in 2026, to HL-LHC[13], in order to increase the instantaneous luminosity, increasing the number of events and thus naturally also increasing the absolute number of rare events occurring. This will allow for precision measurements and discoveries that would have been infeasible on reasonable time-scales with the current luminosity. While being a necessary upgrade, it imposes technical challenges not only on the accelerator itself, but also on the detectors used for studying the particle collisions. With peak instantaneous luminosity reaching $7.5 \times 10^{34} cm^{-2} s^{-1}$, HL-LHC is expected to have an average of 200 collisions per bunchcrossing [98]. At the same time, the expected integrated luminosity over the planned time of operation is 4000 fb^{-1}, translating to an expected fast hadron fluence of $1.75 \times 10^{16} n_{eq}/cm^2$ at the innermost detector layer [98] as seen in figure 1.0.3. While the current pixel detector was designed to operate to at least an accumulated fluence of 10^{15} n_{eq}/cm^2 [6], this level of fluence will be achieved in less than a year during the operation of HL-LHC at planned luminosity [98]. To deal with the increased number of collisions, and accompanying occupancy, ATLAS is replacing the entire inner detector with a new tracker, the ITk, designed exclusively with silicon based detectors,where the new pixel detector consists of five layers as seen in figure 1.0.2.

While HL-LHC is already putting strict requirements on the performance of the proposed detectors, it is simple to draw the conclusion that future colliders will put no less strict requirements. On the contrary, performance requirements will keep on getting more demanding. Initial simulations of the proposed FCC[14] would impose an accumulated fluence of $10^{17} n_{eq}/cm^2$ [95]. Only one study has been done in these fluence ranges, and

---

[12] weakly interacting massive particles

[13] High Luminosity LHC

[14] Future Circular Collider

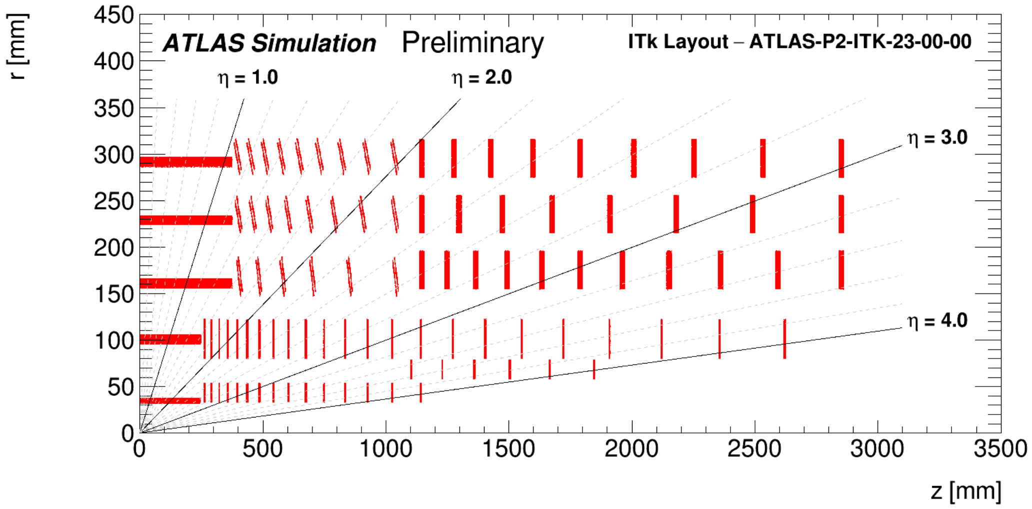

Figure 1.0.2: Planned layout of the ITk pixel detector in the upcoming HL-LHC upgrade [20].

silicon sensors shows significant degradation at these fluences [4]. The proposed ILC[15], or similar lepton linear colliders focusing on precision measurements, would instead put restraints on the total mass of the tracking system to accommodate for high precision vertex detection [12]. While highly radiation tolerant detectors, such as 3D silicon sensors, are being researched as solutions to the high fluence, the high occupancy of future colliders will demand many m^2 of detectors, which in turn will imply large budget constraints.

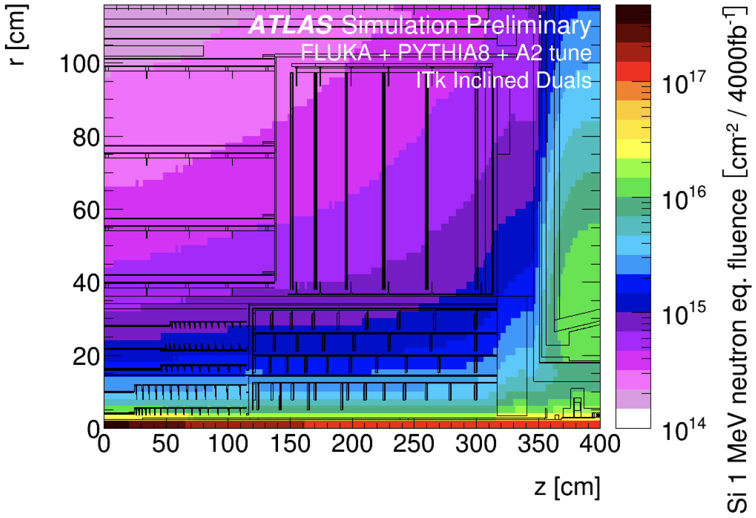

Figure 1.0.3: Simulated fluence for the ITk detector over the expected LH-LHC data taking lifetime [20]. The pixel detector is situated between 3 and 30 cm, and the innermost layer of the strip detector is around 40 cm.

One effort to address these performance requirements while keeping costs down is to

---

[15] International Linear Collider

merge the readout chip with the sensing chip, reducing the total mass particles have to traverse while at the same time eliminating the readout chip and the bump bonding required, significantly reducing pixel production cost. Such sensors are called MAPS[16], or simply CMOS[17] sensors, reflecting the fact that the signal processing electronics utilises CMOS technology. Multiple designs exists, and one that is showing good promise is the so-called large fill factor design, where the active circuitry is housed in a deep implant that functions as charge collection electrode during operation [84]. This is described in more detail in the next chapter. Interest in CMOS detectors, initially as an imaging sensor, and studies of the viability for use in high energy physics started in the 1990s when the first MAPS was introduced [102]. While showing good promise and high fill factor, initial detectors suffered from small active regions, slow readout speeds, and poor radiation tolerance [24, 103].

Recent developments in CMOS technology and silicon fabrication techniques has allowed for larger depletion regions to be achieved either through using a high resistivity silicon for the bulk or processing techniques allowing for high bias voltage without affecting the active circuitry [84]. In contrast to early versions where a partially depleted p-doped epitaxial layer was used as the sensing layer and collection was done in small n-implants separate from the active circuitry, the HV-CMOS[18] design usually has a p-bulk with a deep n-well, functioning both as the electrode for charge collection and as shielding for the circuitry from the high voltage. Normally a smaller p-well is also placed inside the deep n-well in order for the chip to accommodate both NMOS and PMOS circuitry, allowing for more complex signal processing. Another important advantage of a MAPS is the elimination of the need for bonding to another chip. This opens up possibilities for much smaller pixel size, subsequently increasing granularity of the pixel detector beyond what is achievable with a conventional hybrid pixel [102].

In recent developments of MAPS, HV and HR[19] technologies are showing good promise both in detection capabilities and radiation tolerance, catching up to conventional detectors in performance [14, 91]. While both HV and HR technologies focus on increasing the depleted region to allow for faster charge collection and larger signals, the difference is in how they achieve this. HR-CMOS utilises lowly doped silicon wafers for processing, resulting in chips with high resistivity and thus larger depletion at lower bias voltages.

---

[16] Monolithic Active Pixel Sensors

[17] complementary metal oxide semiconductor

[18] High Voltage CMOS

[19] High resistivity

HV-CMOS on the other hand focuses on the implant and sensor design to increase the possible operational voltages, and thus allow for larger depleted regions. Sensors utilising the design for higher breakdown voltage together with high resistivity bulks are also being explored [100, 105]. While both have their advantages and disadvantages, commercial CMOS foundries normally use silicon wafers with resistivities in the order of 10 - 20 Ωcm. Detectors using the standard substrate commonly only achieve an active region of 10 - 20 μm when applying a reverse bias of 100V, limiting the magnitude of the signal strength, making high-resistivity custom wafers desirable. However, many foundries do not offer the selection of custom resistivity, and in case they do, production costs will be higher and limits to possibilities for doing MPW[20] runs for prototype chips can be expected. If the standard processes and standard resistivity wafers could be used while still achieving necessary tracking performance in HV-CMOS based pixel detectors, large cost savings could be made which is necessary when 10s of square meters have to be covered with high-granularity tracking detectors.

This thesis aims to investigate the viability of using standard substrate HV-CMOS detectors, first and foremost from a radiation tolerance view. The key here is to understand how the depletion region in standard-substrate CMOS chips develops with irradiation, by analysing the signal generated by charge injection through light. Understanding this in detail might open up the possibility of pre-irradiating the sensors as a post-production method to increase performance of standard substrate resistivity. In addition to this, TD[21] generation is explored as another potential-post production method to increase the viability of standard-substrate CMOS detectors. Thermal donors are oxygen agglomerates generated in silicon by oxygen impurities when silicon heated to 330 - 500 °C, and act as donors. This could potentially offset some of the p-doping in the sensor bulk, lowering the effective doping concentration. While this has been shown to be true for MCz[22] silicon diodes, even resulting in space charge sign inversion after extended annealing [101], it has yet to be tested in HV-CMOS sensors.

---

[20] Multi Project Wafer

[21] Thermal Donor

[22] Magnetic Czochralski

Chapter 2

Silicon detectors

Tracking detectors have been an essential part of HEP experiments since the beginning of particle physics. Early trackers consisted of cloud chambers, bubble chambers, and drift chambers amongst others, but with with the rapid and extensive development made in the micro electronics and related interconnections technologies, silicon-based tracking detectors were first introduced in the 1980s and have since grown to become a key device in particle tracking technology, thanks to the superior tracking resolution in comparison to other technologies [57]. While many different semiconductor materials exist, silicon being the most abundant solid element on the planet offers low costs, together with desirable properties and the extensive study of the material within the micro technology field has made it a standard material for tracking systems. This chapter gives a brief introduction to the basic operation of a silicon tracking detector, first describing the principle of charge deposition in the material, followed by a short introduction to the signal formation. The chapter is then concluded with a brief introduction to different CMOS detector technologies. This chapter will only regard non-irradiated detectors, with radiation damage and its macroscopic effects being discussed in chapter 3.

2.1 Semiconductor basics

2.1.1 Intrinsic and extrinsic semiconductor

The electrical properties of a semiconductor falls between a conductor and an insulator, being neither good nor bad at conducting electricity. This section will give a small introduction to the electrical properties of the semiconductor, but for a more detailed and comprehensive explanation please refer to any textbook covering the topic, such as [56, 71, 96]. The difference in electrical properties between materials can be described through Pauli's exclusion principle stating that each electron in a quantum system must have a unique quantum state. For large systems, such as a piece of solid material, this aggregates into distinct energy ranges, called bands, where electrons are allowed. The probability of a certain state, with energy E, being filled is governed by the Fermi-Dirac distribution function, which states

$$F(E) = \frac{1}{e^{(E-E_F)/k_BT} + 1} \tag{2.1.1}$$

where T is the temperature, k_B is the Boltzmann's constant, and E_F is the so-called Fermi Energy, which corresponds to the energy of the state that has 50% probability of being occupied. In the semiconductor, E_F lies inside of a forbidden energy region, commonly called *band gap.* The first energy band directly below E_F is called the *valance band* and the first energy band above is called *conduction band.* With few free states in a filled band, the intrinsic semiconductor is a poor conductor. However, by exciting electrons from the valance band into the conduction band, which simultaneous creates a free space in the valance band, labelled *hole*, the movement of charge is made possible. Together the electron, n, and the hole, p, are commonly called charge carriers.

As described below in section 2.2, a charged particle traversing matter excites electrons from the valance band to the conduction band, thus creating free charges. One might think of constructing a detector similar to an ionization chamber, such that an external electric field is applied to collect these generated charges. For wide band gap semiconductors, such as diamond[29], this is possible. However, for silicon, which has a relatively small band-gap, E_g[1]$= 1.12eV$, this is not possible, due to the large amount of thermally stimulated intrinsic charge carriers, n_i, at room temperature. The amount of n_i can be derived from the Fermi-Dirac distribution to be:

$$n_i^2 = np = N_C N_V e^{-\dfrac{E_g}{k_BT}} \quad , \quad where \quad N_{C,V} = \frac{2}{h^3}\left(2\pi m^*_{e,h} k_B T\right)^{\dfrac{2}{3}} \tag{2.1.2}$$

Here $N_{C,V}$ expresses the effective densities of states in the conduction and valance band, h the Planck's constant, and $m^*_{e,h}$ are the respective effective masses of electrons and

---

[1] This is the band gap energy, and is defined as the energy difference between the lowest state in the conduction band and the highest state in the valance band.

holes.

At room temperature this translates into approximately $1.45 \cdot 10^{10} cm^{-3}$ intrinsic carriers, effectively drowning out any $e^{-}h^{+}$ pairs created by a MIP or similar particle as is seen below. To deal with the noise created by the intrinsic carriers the detector could be cooled to reduce the amount of thermally excited charge carriers. However, due to the small band gap, the amount of cooling needed would be structurally and economically infeasible. This is circumvented by doping the silicon and creating a diode structure where all intrinsic charge carriers can be depleted. Doping is done by introducing elements with more or fewer valance electrons, introducing energy levels close to the bands assisting in creating either holes or electrons respectively, as seen in figure 2.1.1 below.

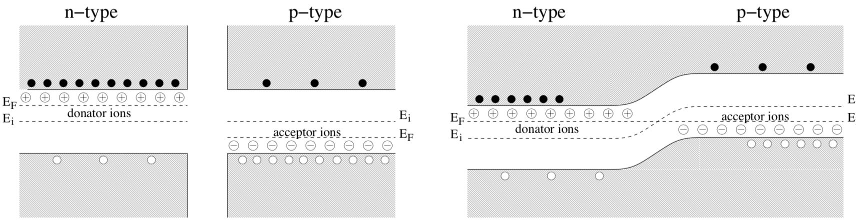

Figure 2.1.1: Band strucutre of a PN junction. Left side shows band structure of stand alone extrinsic silicon. From [63].

Silicon, being an element from group 14 in the periodic table, has 4 valance electrons and forms a crystal by creating 4 covalent bonds with neighbouring Si atoms. By introducing an element from group 15, commonly Phosphorus, with 5 valance electrons, 4 covalent bonds will be created with one left over electron introducing an energy level close to the conduction band. Such an element in silicon is called a donor. Analogously, by introducing an element from group 13, commonly Boron, with 3 valance electrons, 3 covalent bonds will be formed and the neighbouring Si atom will have one left over electron. This introduces energy levels close to the valance band, effectively promoting the creation of holes. Like the previous example, an element introducing holes is known as an acceptor. If the concentration of donors, N_D, is larger than the concentration of acceptors, N_A, the silicon is said to be an n-type silicon. Contrarily, if $N_A > N_D$ the silicon is said to be a p-type silicon. Introducing dopants into the silicon will change the resistivity, resistivity being defined as the inverse of the conductivity, σ, we get

$$\rho = \frac{1}{\sigma} = \frac{E}{J} \tag{2.1.3}$$

where E is the electric field and J the current density. The current density is dependent on the amount of charge carriers and the respective velocity such that.

$$J = qnv_e + qpv_h = q(n\mu_e + p\mu_h)E \tag{2.1.4}$$

Here q represents the elementary charge, and v_e and v_h are the electron and hole velocities. μ_e and μ_h are the electron and hole mobilities, and the last step is done using the relationship $v = \mu E$. Using eq. 2.1.4 with eq. 2.1.3 we arrive at

$$\rho = \frac{1}{q(n\mu_e + p\mu_h)} \tag{2.1.5}$$

Considering a p-type material, with holes as majority carriers, one can assume $p \gg n$ and that the amount of holes, p, is close to the acceptor concentration, N_a, 2.1.5 can be simplified to

$$\rho = \frac{1}{q(N_a\mu_h)} \tag{2.1.6}$$

This relation comes in handy when estimating the initial doping concentration, as silicon foundries developing sensors commonly label the silicon with its resistivity. It should be noted that the donors and acceptors considered above are so-called *shallow* impurities. An impurity is generally considered *shallow* when then ionisation energy is $< 100\, meV$, and is ionised by the thermal energy at room temperature [92]. Common dopants, such as, *Boron* and *Phosphorous* are *shallow* impurities. Impurities with ionisation energy larger than 100 meV are considered to be *deep* impurities, and will be discussed in chapter 3. Now, by bringing n-type and p-type silicon together a PN junction is formed, with quite desirable properties as we shall see below.

2.1.2 The PN Junction

A PN junction is normally, in industry, formed by introducing the opposite doping into an already doped silicon. This creates a gradient transition region where the material goes from one type of doping gradually into the other. However, for simplicity, we shall imagine that we are dealing with abrupt junctions such that a homogeneously doped p-type silicon is intimately connected to a homogeneously doped n-type silicon. In the junction region, the difference in the carrier concentration on either side of the junction causes the carriers to diffuse across the junction. Electrons diffusing into the p-type region combine with the holes, turning the acceptor atoms into negative ions. This creates a negative space charge region on the p-type side close to the junction. Vice versa, holes diffusing into the n-type region create positively charged ions generating a positive space charge region on the n-type side close to the junction. The difference in electrical potential in the two regions erects an electric field causing carriers to drift in the opposite direction of the diffusing carriers. The electric field increases with the increase in the space charge region and an equilibrium between diffusing and drifting carriers is reached causing the space charge region to stop expanding. The overall net charge is zero.

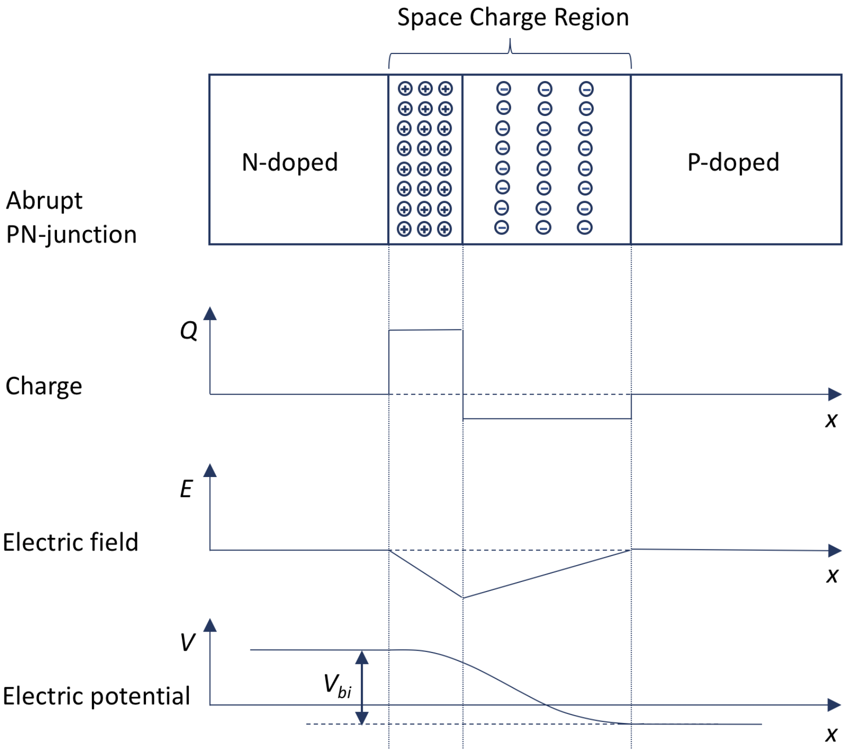

Figure 2.1.2: Qualitative visualisation of electric field, electric potential and space charge region in the PN junction

This region is also commonly labelled as the depletion region, being devoid of any mobile carriers. Without any externally applied voltage, the depth of this region solely depends on the doping concentration of each side. Solving the Poisson equation in the region [96]

$$\frac{dE}{dx} = \frac{\rho}{\epsilon} = \frac{q}{\epsilon}\left(N_D - N_A\right) \quad \Rightarrow \quad -\frac{d^2V}{dx^2} = \frac{q}{\epsilon_{Si}\epsilon_0}\left(N_D - N_A\right) \tag{2.1.7}$$

gives us the voltage created in this region, called the built-in voltage, V_{bi}, to be:

$$V_{bi} = \frac{q}{2\epsilon_{Si}\epsilon_0}\left(N_D x_n^2 + N_A x_p^2\right) \tag{2.1.8}$$

Here the ϵ_0 is the vacuum permittivity, ϵ_{Si} the relative permittivity for silicon, N_D the donor doping concentration, N_A the acceptor doping concentration, and x_n and x_p the width of the depletion region from the PN junction in the n-type and p-type side, respectively. This relationship is achieved by assuming an abrupt junction, as stated above, with $x = 0$ at the junction. Following that the net charge of the whole system is zero, we know that $N_D x_n = N_A x_p$. Using this, x_p and x_n can be isolated individually, and the total depletion width, $w = x_p + x_n$, ends up being:

$$w = \sqrt{\frac{2\epsilon_{Si}\epsilon_0}{q}\frac{N_A + N_D}{N_D N_A}V_{bi}} \tag{2.1.9}$$

However, in a typical silicon based sensor the PN junction is strongly asymmetrical, meaning either $N_A \gg N_D$ or $N_D \gg N_A$. In this case, the depletion region mainly extends into the lowly doped area and the depletion width equation simplifies into

$$w = \sqrt{\frac{2\epsilon_{Si}\epsilon_0}{qN_{D,A}}V_{bi}} \tag{2.1.10}$$

where $N_{D,A}$ takes the doping concentration value of the lowly doped region. As will be seen in the next chapter, some lattice defects are electrically active altering the overall space charge region. $N_{D,A}$ is then substituted by $\mathrm{N_{eff}}$ in equation 2.1.10 to represent the effective space charge in the lowly doped region of the detector.

Charge carriers created by a charged particle traversing the depletion region will be separated by the built-in electric field and start drifting, creating a relatively weak signal. However, outside this region, which makes up the majority of a typical unbiased silicon detector, the created charge carriers will combine with the abundance of intrinsic carriers after a short time of diffusion as described above. By applying an external electric field, with high potential to the n-type side and low potential to the p-type side, each side will be drained of majority carriers, increasing the overall depletion region. A large enough applied voltage extends the depletion region across the whole sensor, maximising the sensing region of the detector. The increased depletion width is calculated by extending formula 2.1.10 into:

$$w = \sqrt{\frac{2\epsilon_{Si}\epsilon_0}{qN_{D,A}}\left(V_{bi} + V_{bias}\right)} \tag{2.1.11}$$

Typically $V_{bias} \gg V_{bi}$, as V_{bi} is commonly around or below 1V, making it normal to omit V_{bi} from equation 2.1.11. Applying a reverse bias to collect charge carriers generated by traversing particles while simultaneously depleting the sensor of free charge carriers is the basis for using silicon sensors in charged particle detection.

It should be pointed out that 2.1.2 is an ideal structure and the realistic PN-junction is more complex. When an implant of opposite doping is made, instead of a perfectly abrupt junction there is a gradient of decreasing concentration, and the junction itself can be defined where there implanted dopants concentration falls below the bulk doping concentration. In the case of a strongly asymmetrical junction, the abrupt model is a good approximation [40], and is what is used in this study.

2.2 Charge deposition in Silicon

When ionising radiation, photons or charged particles, interacts with a silicon crystal, electron hole pairs are created through the excitation of electrons from the valance band to the conduction band. The electron, e^-, and the hole, h^+, are so-called charge carriers, the foundation for signal creation as will be discussed below. The excitation of charge carriers is a reversible process causing no damage to the crystal, as opposed to non-ionising energy loss (NIEL) described in the next chapter. The amount of charge carriers created through the ionising radiation is dependent on the energy deposited and the ionisation energy. The ionisation energy is a material dependent property, with silicon having an ionisation energy of 3.6 eV which is the mean energy required to create one e^-/h^+ pair. The deposited energy is largely dependent on the type and energy of radiation.

2.2.1 Charged particles

A significant amount of the ionising energy deposition inside the tracker of detector experiments are due to traversing heavy charged particles, such as protons and pions. The rate of energy loss through ionisation in matter is described in a relativistic quantum mechanical way by the Bethe Bloch formula [71].

$$\frac{dE}{dx} = 2\pi N_0 r_e^2 m_e c^2 \rho \frac{Z}{A} \frac{z^2}{\beta^2} \left[ln \left(\frac{2 m_e \gamma^2 v^2 W_{max}}{I^2} \right) - 2\beta^2 - \delta - 2\frac{C}{Z} \right] \tag{2.2.1}$$

The parameters here are:

x is the path length in g/cm^2

N_0 is the Avogadro's number

r_e is the classical electron radius

m_e is the electron rest mass

ρ is the medium density

Z is the atomic number of the medium

A is the atomic weight of the medium

z is the charge of the traversing particle

c is the speed of light

v is the velocity of traversing particle

$\beta = v/c$

$\gamma = 1/\sqrt{1-\beta^2}$

W_{max} is the maximum energy transfer in one collision

I is the effective ionization potential averaged of all electrons

δ is a density correction

C is a shell correction

The formula is largely dependent on what material is used as can be seen with the parameters I, Z, A, and ρ, describing the average excitation energy, the atomic number, the relative atomic mass, and the material density respectively. In the case of silicon we get the following energy deposition.

As can be seen in figure 2.2.2, there is a minimum in the energy deposited by charged particles in the relativistic regime between 10^2 and 10^3 MeV. These particles are called MIPs[2] and are a dominant part of the traversing particles in the LHC collider experi-

---

[2] Minimum Ionising Particles

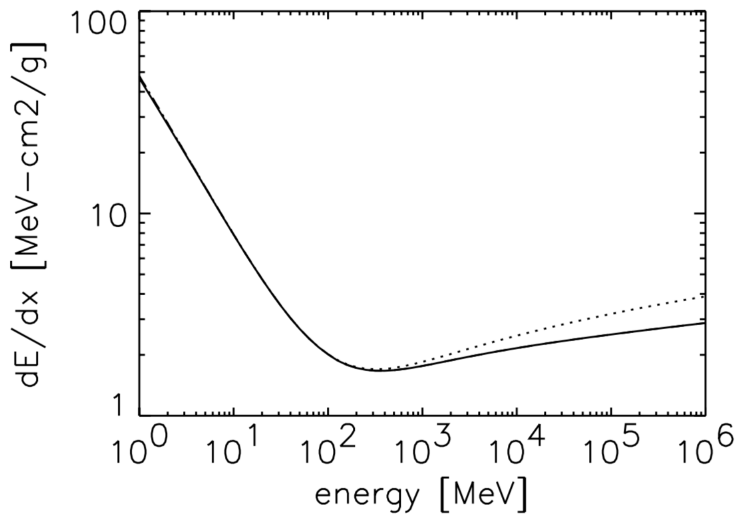

Figure 2.2.1: Energy loss of traversing particle through ionisation in silicon as a function of particle energy. The dotted line is without the density and shell correction. It has to be noted the dE/dx is normalised to ρ of the material here. From [71]

ments. While the energy for minimum ionisation is different for different particle types, the deposited energy by MIPs in silicon, which has a relatively high density of 2.33 g/cm^3, is approximately equivalent to:

$$\left.\frac{dE}{dx}\right|_{min} \approx 3.88 MeV/cm \tag{2.2.2}$$

This translates to approximately 32200 e^-/h^+ pairs are generated in 300 μm thick silicon. However, it has to be noted that the Bethe-Bloch formula only provides the *mean* energy loss of a traversing particle. The actual energy loss in a thin semiconductor by a MIP fluctuates statistically and was early described by the asymmetric Landau distribution, which has a long tail towards higher energies. Due to the asymmetric nature of the distribution, the calculated *mean* from the Bethe-Bloch formula is higher than the *most probable* amount of generated charge for a MIP. The *most probable* value of the Landau distribution is typically 0.7 time the *mean*, however depends on particle energy and measurement range. While some different values are reported, in 300 μm silicon the amount of generated charge carriers is commonly given to be around 22500 e$^-$h$^+$ pairs [35, 10]. It should be pointed out that as the detecting layer gets thinner, the energy loss starts to deviate from the Landau distribution. Around 300 μm the deviation is slight and the Landau distribution is still a good approximation of *most probable* energy loss, but below 150 μm significant deviation is seen [15].

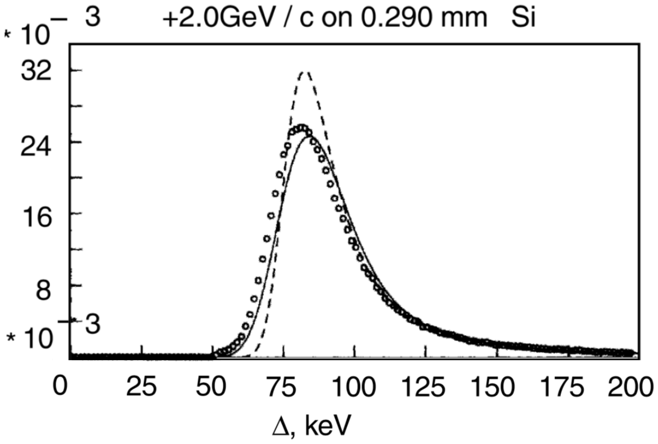

Figure 2.2.2: Measured energy loss for 2 GeV protons in 290 μm silicon. Dots are the measured values, the dashed lined is the Landau distribution, and the solid line represents a more refined model [10].

2.2.2 Laser illumination

In contrast to charged particles, photons create e^-/h^+ pairs through the photo electric effect. This is a useful property when studying silicon as the deposited energy does not differ greatly between pulses of laser illumination, in contrast to charged particles. Although the mean ionisation energy of silicon is 3.6 eV, the band gap of silicon is 1.12 eV at room temperature, meaning light with wavelengths up to 1107 nm can be absorbed to create a e^-/h^+ pairs. However, as silicon has an indirect band gap photons close to the band gap energy require additional momentum, commonly provided by a phonon in the crystal, to be absorbed. The indirect band gap in silicon also means that as the wavelength approaches 1.12 eV, less light is absorbed per unit length. In contrast to red light which gets absorbed within the first few μms of the surface, longer wavelengths can penetrate deeper into silicon, generating e^-/h^+ pairs along the path. The intensity drops according to the formula:

$$I(x) = I_0 e^{-\mu x} \tag{2.2.3}$$

Where I_0 is the initial light intensity, x is the traversed thickness from the surface and μ is the material and energy-dependent absorption coefficient. As can been seen in figure 2.2.3, illumination with red light at around 640 nm will be absorbed close to the surface of the silicon while IR[3] light above 1060 nm will penetrate the full thickness of

---

[3] Infrared

a conventional silicon sensor. While exponentially decreasing within the first 500 μm of the detector the IR can be assumed to homogeneously excite charge carriers.

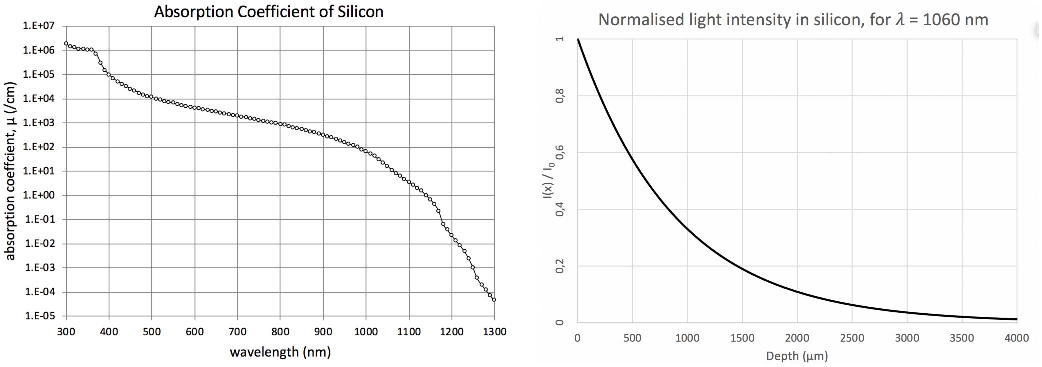

Figure 2.2.3: On the left: The absorption coefficient, μ, in silicon as a function of wavelength. On the right: Normalised light intensity as a function depth into silicon, for light with 1060 nm wavelengths. Active regions studied samples lie within 500 μm of the surface. Data is taken from [39].

2.3 Principle of operations of the silicon detector

A typical silicon sensor used in charged particle tracking operates similarly to an ionisation chamber. Reverse bias is applied to the silicon detector to deplete the whole volume of thermally stimulated charges. Then, charged particles traversing the silicon will generate e^-/h^+ pairs, which will then start to drift under the influence of the electric field in the depleted region. These drifting charges are the basis for the signal formation in the detector as we shall see in the following section. Two main advantages of the silicon detectors are the relatively high number of generated charge carriers, approximately 22500 by a MIP in 300 μm of silicon, and the high carrier mobility[4] at room temperatures. This amount of charge carriers allows for compact detectors, while the high mobility is essential for fast signals which is crucial in the high-occupancy environment of the LHC.

2.3.1 Signal Formation

According to [89], the movement of charges induces a charge in spatially nearby electrodes. As described above, charge carriers inside the silicon lattice can move by means of diffusion or drift. Diffusion is stochastic movement due to thermal energy, while drift is induced by an external force such as an electric field. As seen below, early CMOS

---

[4] $\mu_e \approx 1500\ cm^2V^{-1}s^{-1}$ and $\mu_h = 500\ cm^2V^{-1}s^{-1}$

detectors relied on charge collection through by diffusion [42], silicon detectors today are predominantly based on drift for collecting charge.

Charge carriers inside a biased detector start to drift towards the attracting electrode. The drift velocity is determined by the mobility of the charge carrier and the electric field strength

$$\vec{v} = \mu \vec{E} \tag{2.3.1}$$

This holds at moderate strengths of the electric field. For large $\vec{E}$, the mobility μ in silicon becomes inversely proportional to the electric field strength, $\mu \propto 1/\vec{E}$, and the velocity eventually plateaus, reaching a so-called saturation velocity. As can be seen in figure 2.3.1 below, the electron drift velocity in the bulk at 300 °K starts to decrease above approximately $5 \cdot 10^3 V cm^{-1}$, and later saturates at a drift value close to $10^7 cm \cdot s^{-1}$.

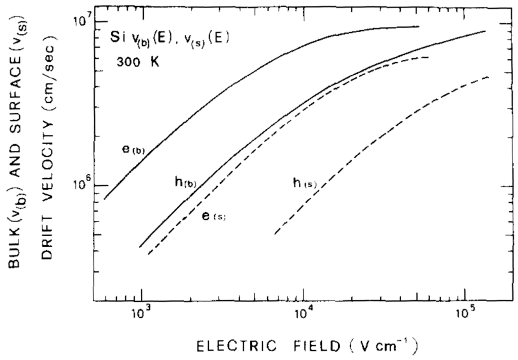

Figure 2.3.1: Electron and hole drift velocities in silicon as a function of electric field strength. From [53]

The drifting charge generates a signal current in spatially close electrodes, through inducing charge. This effect is explained by the Ramo theorem stating that the induced current in the electrode is proportional to the drifting charge such that

$$i(t) = q\vec{E}_R \cdot \vec{v} = q\mu\vec{E}_R \cdot \vec{E} \tag{2.3.2}$$

Here the $\vec{E}_R$ is the so-called Ramo field, which explains how the moving charge electrostatically couples to a given electrode. The Ramo field is purely dependent on the geometrical layout of the detector and is obtained from the the Ramo potential, Φ_R, through:

$$\vec{E}_R = -\vec{\nabla}\Phi_R \tag{2.3.3}$$

Where $\Phi_R = 1$ on the readout electrode, $\Delta\Phi_R = 0$ between the electrodes, and $\Phi_R = 0$ on the remaining electrodes, assuming they are connected to low impedance. In the simple case of a fully depleted diode, where the PN junction plane is assumed to approach infinity, the $\vec{E}_R = 1/x_d$, where x_d is the detector thickness. In a more complex detector geometry, which is almost always the case for actual sensors, the $\vec{E}_R$ has to be solved numerically. Furthermore, it should be noted that eq. 2.3.2 is only valid when the pixels are connected with low impedance to the read-out. In the case where floating electrodes are in proximity to the readout electrode this equation has to be altered. The Ramo field can be extended by considering the induced charge in the floating electrodes by the moving point charge. This will give a Ramo field dependant on the Ramo field of the other electrodes. Additionally, it depends on the voltage response in the other electrodes and is thus time dependent. This new Ramo field on electrode k can be written as

$$\vec{E}'_{Rk}(t) = \delta(t)\vec{E}_{Rk} - \sum_{i\neq k} N_{k,i}(t)\vec{E}_{Ri} \tag{2.3.4}$$

where $\delta(t)\vec{E}_{Rk}$ is the Ramo field when considering the Ramo potential to be 0 on the other electrodes, apart from k, and $N_{k,i}(t)$ is the voltage response in electrode i to a unit voltage pulse (delta) at electrode k. A detailed derivation for this weighting field can be seen in [38]. Considering the reciprocity theorem $N_{k,i}$ must be equal to the fraction q_k/q_i, where q_i is the charge placed on electrode i, and q_k the charge induced in electrode k. Following the charge conservation law, the sum of these fractions needs to add up to one. We consequently get the induced current on electrode k to be

$$i_k(t) = q\vec{E}_{Rk}\vec{v}(t) - q\sum_{i\neq k} N_{k,i}(t)\vec{E}_{Ri}\vec{v}(t) \tag{2.3.5}$$

Thus, in the $N_{k,i}$ terms needs to be calculated in order to evaluate the induced current when floating electrodes are in close to the readout electrode. If all electrodes i are grounded, $N_{i,k}$ becomes 0 and eq. 2.3.5 reduces to eq. 2.3.2. The samples in this work only contains effectively contains one read-out electrode and as such only eq. 2.3.2 is considered in the analysis.

2.3.2 Readout

A conventional hybrid pixel module, such as the one currently used in the original ATLAS pixel detector, consists of a sensing silicon chip and a readout chip containing dedicated signal processing circuitry. The sensor used in ATLAS is a n-in-n sensor, meaning it has a lowly doped n-type bulk with high p and n type implant on back and front side, respectively. The n^+ side is used for readout, and bias is supplied on the p^+ side [6]. For a hybrid pixel module, each pixel on the sensing chip is connected to a corresponding processing pixel on the readout chip through a so called flip chip bonding technique [71]. Tiny bumps of indium, gold, or solder are attached to each pixel on the sensor chip, and the readout chip is then mounted face to face onto these bump by melting the bumps, commonly through hot air reflow, and sometimes through thermosonic means.

There are different readout chips, with various features, but generally a readout chip should include:

- Amplification of signal
- Noise filtering and signal discrimination
- Signal storage and marker setting for readout cycle
- Circuitry reset after signal readout, or at periodic intervals

In addition to the integrated electronics needed for these features, large areas of the chip are used by buses for reading out the stored signal data. A common design is to readout the pixels column-wise, instead of a whole matrix. This has the advantage that in case a faulty pixel being present, only that column will be affected, instead of the whole pixel matrix. In older and comparatively less complex readout designs, the pixel only provided data on whether the signal had exceeded a set threshold or not. The readout chip in the original ATLAS pixel detector, *FE-I3* [85], transfers information on the pixel address, timestamp when signal goes above signal threshold and timestamp when signal falls below the threshold for temporary storage to the chip periphery. From this data, the ToT[5] is calculated, from which the energy deposition by the traversing particle can be estimated.

These detectors generally achieve excellent signal-to-noise ratios, and by having the signal processing electronics on a separate chip, highly complex features can be added.

---

[5] Time-over-Threshold

However, one direct drawback of having a separate processing chip, albeit being thin, is added material which increases the scattering probability and reduces the ability for high precision vertexing and tracking. Furthermore, due to the high density of the connection pads, bump bonding is necessary to connect the sensor chip to the readout. While this technique can accommodate for very fine pitches, down to below 10 μm [72], it is relatively costly and its mechanical fragility adds an additional step where the whole pixel module can fail. To overcome these challenges, research is being done to combine the two chips into a single pixel chip.

2.4 Novel detector technologies

A proposed way to circumvent the obstacles imposed by the current pixel detector concept is to utilise the last decades' advances in micro electronics through having part or all of the signal processing electronics incorporated directly in the sensing pixels, creating a so-called monolithic detector. Such a detector, with active CMOS circuitry in the sensing pixel, was first developed in the 60s for the imaging industry. However, the development of CCD[6] detectors in the 70s quickly stifled the development of CMOS detectors, and not until 1999 was a monolithic CMOS pixel detector proposed to be used for high energy physics applications [84]. Standard CMOS detectors used in the imaging industry at that time commonly consisted of an epi-layer, containing the n-wells and p-wells housing the NMOS and PMOS circuitry. The epi-layer had lower doping than the silicon substrate, causing it to act as a shallow energy well for charge carriers created by traversing particles, allowing them to diffuse around and eventually be collected at an n-well. These sensors had a dedicated n-well for charge collection, while also using separate p- and n-wells for circuitry implementation, causing some of the charge carriers to be collected in the implants dedicated to the active circuitry. This caused the fill factor[7] to drop below 100%, as illustrated in figure 2.4.1. Particle detector experiments require a 100% fill factor, making these early commercial detectors unusable.

Early versions to create a 100% fill factor sensor were made possible through eliminating the PMOS circuitry leaving only one place for the electrons to be collected, eliminating signal loss. However, the lack of PMOS circuitry limits the possible features for signal processing. Additionally, the detectors were still based on the diffusion of charge, re-

---

[6] Charge Coupled Device

[7] The ratio of the sensitive area to the whole detector area.

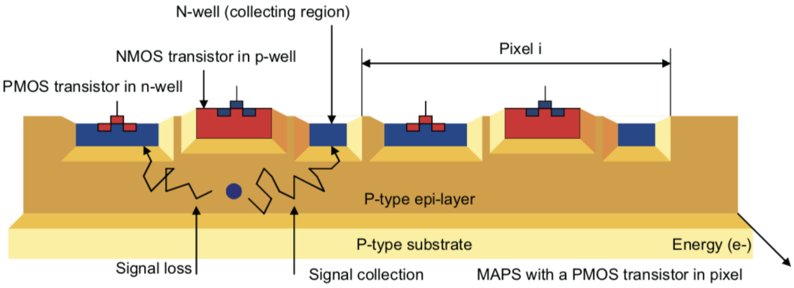

Figure 2.4.1: Electron diffusing in epi-layer. Loss of charge when electron is collected at PMOS n-well, potentially missing particle detection. From [84].

sulting in long collection times (∼100ns), causing the detector to have poor radiation tolerance. Recent developments have addressed these shortcomings through having signal generated by drift while incorporating active NMOS and PMOS circuitry operating under relatively high reverse biases.

2.4.1 High Voltage CMOS

High voltage CMOS technology is widely used in the automotive industry, with extensive commercial development. Specifically, a structure design called "floating logic" was implemented to allow for high bias of the bulk without damaging the active CMOS circuitry. Removing the previously used epi-layer[8], a deep n-well is implanted in the bulk which in turn hosts an even higher doped n-well containing the PMOS and a p-well containing the NMOS electronics as seen in figure 2.4.2. The deep n-well, in addition to shielding the active circuitry, also acts as the collection electrode for the generated charges.

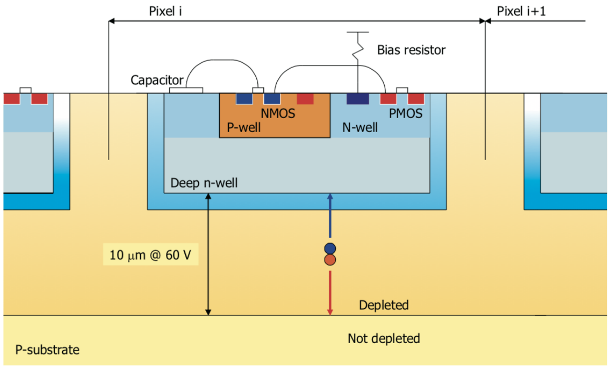

Figure 2.4.2: General layout of a HV-CMOS pixel detector. From [84].

This design requires some design alternations to normal active circuitry where generally

---

[8] Epitaxially grown silicon layer atop the substrate. Seen in figure 2.4.1

an n-well housing PMOS circuitry has a positive voltage applied to reduce transistor leakage current. However, as the N-well in this case also acts as the collection electrode this would drain the generated charge causing a loss of signal. This is solved by incorporating a high resistance to the DC bias, effectively making it ”floating” for fast charges. In addition, such a detector is designed so that a large processed signal in the PMOS does not capacitively couple to the N-well it is housed inside.

Two main readout designs have been explored for the HV-CMOS technology. Most detectors using the HV-CMOS concept incorporate readout electronics at one end of the chip, reading out single pixels to this structure through multiplexing. Multiplexing readout acts as a bottleneck to the readout speed [84]. To circumvent this bottleneck, similarly to a conventional hybrid pixel detector, it is possible to use a separate readout chip. However, in contrast to the conventional detector, this can be achieved without using the bump bonding technique in HV-CMOS sensors. As an amplifier is already incorporated in the sensing pixel, sufficiently large signals for capacitive coupling can be achieved and a readout chip can then simply be glued non-conductively to the sensing chip. This allows for parallel readout and complex signal processing of hybrid pixel detector, while eliminating the need of bump bonding. On the other hand, analogously to the hybrid pixel case more scattering of traversing particle will occur due to the increased material.

Chapter 3

Defects and damage

Silicon detectors commonly impose high demands on the quality of the silicon crystal used. Conventionally, detectors require silicon with high resistivity and high minority carrier lifetime for good efficiency. To meet these requirements, mono-crystalline silicon of high purity is desired. Although production methods have been refined to gradually produce purer silicon over the years, no silicon crystal is perfect. Impurities and lattice defects are unintentionally included during production of large silicon crystals. Additionally, exposing silicon detectors to radiation damages the lattice further. Defects, both from production impurities and those induced by radiation in sufficiently large quantities, have macroscopic effects on various properties of the silicon detector. By understanding how different impurities and defects changes the properties and behaviour of the detector, the detector can be designed to have features counteracting or utilising the effects of the defects. This kind of defect engineering is already used in the current ATLAS and CMS pixel detectors, which are detectors made from FZ silicon that have been heat treated to have high amounts of oxygen diffused into the bulk, making the effective doping concentration of the detector more resilient to radiation damage [69]. On the other hand, instead of making the detector less susceptible to radiation damage, one can imagine using the defects to have the detector improve after radiation. While not studied much until now due to their low initial charge collection efficiency, low resistivity detectors have shown to improve after being exposed to radiation levels around what is expected in the outer layers of the planned ITk for the HL-LHC ATLAS [32, 28], and this will be further explored in this thesis.

3.1 Production impurities

The majority of substrates for silicon-based particle detectors today are grown using the Float Zone (FZ) technique, as it is able to achieve low levels of crystal impurities and doping concentration, leading to high resistivity. Low levels of doping concentration are important in conventional silicon sensors to ensure for full depletion of the sensor at reasonable bias voltages. On the contrary, the majority of the mono-crystalline silicon in the world is produced through the Czochralski (Cz) method, due to the lower production cost and high throughput demanded by the silicon industry.

Cz silicon is produced by firstly melting polycrystalline silicon of high purity and the desired dopants inside a crucible. A mono-crystalline silicon seed is introduced into the melt, acting as a crystallisation point for the silicon melt as the seed is slowly pulled upwards while the crucible is rotating. During crystallisation, the attaching silicon melt follows the same lattice structure of seed crystal resulting in a large single crystal.

During the process, part of the crucible, being made out of SiO_2, dissolves into the melt [21] as is illustrated in figure 3.1.1 below. The majority of the dissolved crucible escapes as SiO gas, but part of the quartz ends up as a oxygen impurities inside the silicon melt. In addition to this, the SiO gas also reacts with the heating rods, being made out of graphite, which causes C atoms to diffuse into the melt. This causes Cz silicon to typically have an impurity concentration of O between $2 \cdot 10^{17}$ and $1 \cdot 10^{18} cm^{-3}$, and C concentration in the $10^{16} cm^{-3}$ range [65].

While a high O concentration is desirable in silicon detectors due to giving the silicon increased radiation tolerance, it can also cause electrically active defects to form if the silicon is exposed to elevated temperatures. These defects are called *thermal donors* and are generally unwanted in the semiconductor industry due to them having the potential to alter the effective doping concentration of the material. However, this study tries to explore the viability of exploiting the thermal donor generation in order to manipulate the effective doping concentration to increase the active region in low-resistivity HV-CMOS chips.

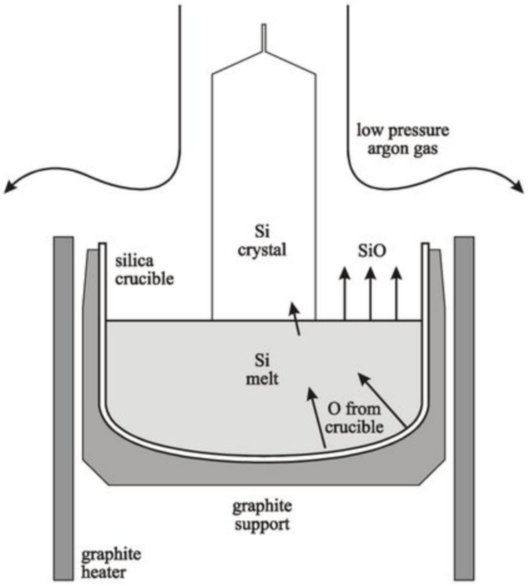

Figure 3.1.1: Schematic of Cz silicon growth, highlighting the oxygen diffusing into the Si melt from the SiO_2 crucible. Adapted from [52].

3.2 Thermal donor generation

When Cz silicon is exposed to temperatures between 330 deg C and 500 deg C, the oxygen impurities in the crystal create electrically active oxygen aggregates, called thermal donors [36, 54]. While thermal donors are still not fully understood, early attempts to model the formation of thermal donors found that the interstitial oxygen forms aggregates of two to four atoms, with the most common structure being SiO_4. The formation kinetics of these aggregates depend predominantly on the annealing temperature and oxygen concentration, while other factors such as carbon concentration also affects the formation of thermal donors, but to a lesser extent [94]. While thermal donors are formed in the whole temperature range stated above, the generation rate is limited at low temperatures and then increases with increasing temperature until the peak generation rate, $\left.\frac{dn_{TD}(t)}{dt}\right|_{max}$, that has been found to be at approximately 450 °C, after which the generation rate starts to decline again. This is attributed to the fact that lower temperatures seem to predominantly create aggregates of two oxygen atoms which do not act as double donors, thus giving a smaller introduction rate of donors [70], along with reduced diffusivity of oxygen interstitials at lower temperatures [83]. At higher energies annihilation of oxygen agglomerates starts to overtake the formation, eventually lowering the introduction rate of donors, together with promotion of less stable larger aggregates, as well as the so called new-donor [43]. This study will however only investigate the classical double donor formed around 450 °C. At temperatures above 500 °C annihilation of the O_4 structure is strictly dominant, and exposure to temperatures above 500 °C is sometimes used in the industry to rid chips of thermal donors formed during both the cooling step of crystal formation and during certain production steps with elevated temperatures. Differentiating from the introduction rate, the equilibrium concentration of thermal donors increases with lower temperatures, due to the absence of annihilation of donors [106]. However, with the introduction rate being significantly reduced, reaching equilibrium concentration with the set up in this study would be infeasible. Extending on the formation kinetics argument introduced with the KFR model [54], which states that thermal donors are predominantly contributed to aggregates of four oxygen atoms, [106] builds on experimental results and introduces a model that takes the electron concentration into account for the introduction rate of thermal donors. At $\left.\frac{dn_{TD}(t)}{dt}\right|_{max}$ experimental data shows good agreement to the generation rate being dependent on the fourth power of the oxygen concentration following

$$\frac{dn_{TD}(t)}{dt} = aD_iO_i^4n^{-m}exp(-bD_iO_it) \tag{3.2.1}$$

where D_i is the diffusion coefficient of oxygen interstitials in silicon, a and b are fitting constants independent of annealing temperature, n is the total electron concentration, and m is the number of electrons given by the formed aggregate. m has been shown to be predominantly 2, which can be interpreted such that the majority of thermal donors formed at 450 °C are double donors. In contrast to the earlier KFR model, this model assumes the electron concentration to have a direct suppressing effect on the formation of the donor-like oxygen aggregates. The electron concentration depends on the doping of the material and for p-type silicon it is calculated with:

$$n = \frac{n_i^2}{0.5\left((N_a - N_d - n_{TD}(t)) + \sqrt{(N_a - N_d - n_{TD}(t))^2 + 4n_i^2}\right)} \tag{3.2.2}$$

Where n_i is the intrinsic electron concentration, which is approximately $2 \cdot 10^{16} cm^{-3}$ at 450 °C. From eq. 3.2.1 it follows that the absolute thermal donor value after an annealing time t depends on the third power of the oxygen concentration, which is also in agreement with data that shows the maximum equilibrium concentration to be proportional to the third power of the oxygen concentration [106]. The diffusivity of isolated interstitial oxygen atoms at 450 °C is achieved by taking extrapolated data from [97], and is $3.4 \cdot 10^{-19} cm^2 s^{-1}$ at 450 °C. Early results show large discrepancy with this value, which, according to [81], can be attributed to presence of dimers and trimers formed at temperatures above 500 °C which increases the formation rate of thermal donors in the 330 - 500 °C region. As such, formation rates calculated using eq. 3.2.1 might underestimate the actual formation rate, depending on the historical exposure to temperatures above 500 °C of the silicon used. The fitting constants a and b have been found to be $2.8 \cdot 10^{-10} cm^4$ and $5 \cdot 10^5 cm^4$, respectively [106].

3.3 Radiation damage

A major concern when operating silicon detectors in a high radiation environment is defects induced by the high energy particles, causing the detectors behaviour to change. These defects can be divided into two categories, surface defects and bulk defects. Surface defects are relatively well studied as they are the main concern for the semiconductor industry. These defects are produced when ionising particles generate charge carriers in the insulating oxide layer at the surface of the detectors. While the generated electrons are quickly collected, the holes, having a significantly lower mobility, are prone to getting trapped in the oxide or oxide-silicon interface. This accumulation of holes leads to electrons being attracted, raising the local conductivity and surface leakage currents [96]. On the other hand, bulk damage is caused by the displacement of silicon atoms in the lattice and changes the fundamental properties of the detector. Understanding how bulk damage is generated and how it affects the detector's characteristics is thus vital in designing effective and radiation tolerant detectors. A further step, explored in this study, is to investigate if generating bulk defects can be used as a possible post production method for enhancing detector properties.

3.3.1 Defect generation

The two principal mechanisms causing a particle to lose energy when traversing silicon, are ionising and non-ionising energy loss (NIEL). Energy loss through ionisation of the material is, as described earlier, through which charged particles are detected. This mechanism does not cause any long term damage to the bulk, as charge carriers either recombine quickly or are collected by the electrodes in the case of a biased PN junction. Contrarily, a particle is said to undergo NIEL when it transfers energy and momentum to the silicon lattice, causing silicon atoms to be displaced. As opposed to ionisation, this can cause irreversible damage to the lattice and permanent change to the detector properties. The silicon atom receiving such energy and momentum, commonly from hadrons or high energy leptons, is called *primary knock-on atom*, PKA. The displacement energy threshold for creating stable Frenkel Pairs in Silicon is on average 36 eV over all lattice directions[1] [47], and the incoming particle must be able to impart greater energy than this for NIEL to take place. Depending on the amount of transferred energy, the PKA can then further migrate into the lattice, knocking out more silicon atoms from their positions in the lattice, causing a chain reaction of silicon atom displacement. The damaged caused by the PKA is largely determined by its energy and a PKA traversing the lattice with high energies generally ends up producing so-called point defects along its path before finally terminating by, commonly, creating a local aggregate of defects, named cluster defects. If the energy transferred to the PKA lies in the region 2 keV - 12 keV, the the PKA terminates by creating one defect cluster. Energies below 2keV primarily causes point defects, and energies above 12 keV produces several cluster defects and point defects [71]. With the energy transfer cross section being dependent on the energy and type of the incoming particle, the induced bulk defects are highly dependent on the type of radiation the silicon is exposed to. This is visualised in figure 3.3.1, where neutrons (right) can be seen to produce more cluster defects, compared to both 10 MeV and 24 GeV protons. Additionally, protons in the lower MeV range create more point defects compared to higher energy protons, where cluster defects become more prominent. In order to be able to compare the change in detector properties as function of irradiation between different particles and energies, the NIEL hypothesis was introduced, and is the subject of the next section. It should be noted that in addition to NIEL, nuclear interactions, such as neutron capture and nucleus transmutations, are also important processes in the lattice. Notable nuclear transmutations are silicon atoms turning into Aluminium or Magnesium, two elements that act as dopants in silicon. However, these processes are generally outweighed by NIEL by two orders of magnitude [93], and can normally be ignored.

3.3.2 NIEL Hypothesis

The NIEL hypothesis was initially developed when comparing defect generation caused by different particles or particle energies, and states that the non-ionising energy loss is

---

[1] It should be noted the displacement damage threshold is dependent on the lattice orientation. The global minimum threshold for Silicon can be considered around 12.5 eV, while the average threshold energy for producing either a bond defect or a Frenkel Pair is around 24 eV[47].

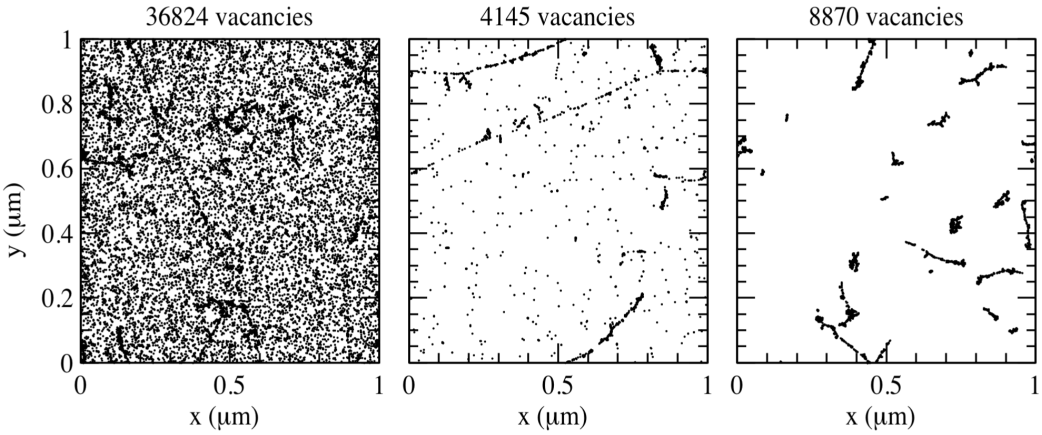

Figure 3.3.1: Simulation of vacancies induced by irradiation to $10^{14} n_{eq} cm^{-2}$ in 1 μm of silicon. Left shows 10 MeV protons, middle 24 GeV protons, and right 1 MeV neutrons. Plot from [50].

the only cause of defect generation in the bulk. This assumption was supported early by experimental results [11, 2], but more recent experiments have shown to violate this hypothesis [58]. Nevertheless, it accurately predicts how leakage current scales with NIEL and as such provides a useful reference when comparing irradiations with different particles and energies [79]. Assuming displacement damage is irrespective of the spatial distribution of the defects caused by a PKA and subsequent annealing, the displacement damage cross section can be calculated as following [64]:

$$D(E) = \sum_k \sigma_k \int_0^\infty f_k(E, E_R) P(E_R) dE_R \tag{3.3.1}$$

This is the sum of all possible interactions between incoming particle and silicon atoms causing displacement defects. σ_k represents the cross section of the interaction k, f_k is the probability that a particle with energy E imparts E_R energy in the silicon atom, and $P(E_R)$ is a partition function based on electronic screening developed in [66] and describes the portion of the imparted energy E_R that is subsequently deposited in form of displacement damage. Using this displacement damage cross section, it is common practice to relate displacement damaged caused by sources of different energy spectra, $\phi(E)$, to each other through a so called hardness factor, κ.

$$\kappa = \frac{\int D(E)\phi(E)dE}{D(E_n = 1MeV)\int \phi(E)dE} \tag{3.3.2}$$

As the D(E) depends on neutron energy, κ is calculated with 1 MeV neutrons as reference point. The 1 MeV *neutron equivalent fluence*, Φ_{eq} is the calculated as.

$$\Phi_{eq} = \kappa\Phi \qquad with \qquad \Phi = \int_{Emin}^{Emax} \phi(E)dE \tag{3.3.3}$$

The unit of Φ_{eq} is given as $\mathrm{n_{1MeV,eq}/cm^2}$, commonly shorted to $\mathrm{n_{eq}/cm^2}$. The Φ_{eq} at different irradiation centres is commonly calculated by irradiating well-defined silicon diodes and measuring their increased leakage current, then deriving the value of κ. Below is a table of hardness factors for the irradiation facilities used in this study.

Irradiation facility	Particle energy	Hardness factor (κ)
LANSCE	800 MeV Protons	0.75
Bern Cyclotron	18 MeV Protons	3.49
IJS (TRIGA Mk. II)	Reactor Neutrons (∼¡ 10 MeV)	0.9

Table 3.3.1: List of hardness factors for irradiation facilities used in this work.

Furthermore, figure 3.3.2 below shows the displacement damage cross section discrepancy between different particles for different energies.

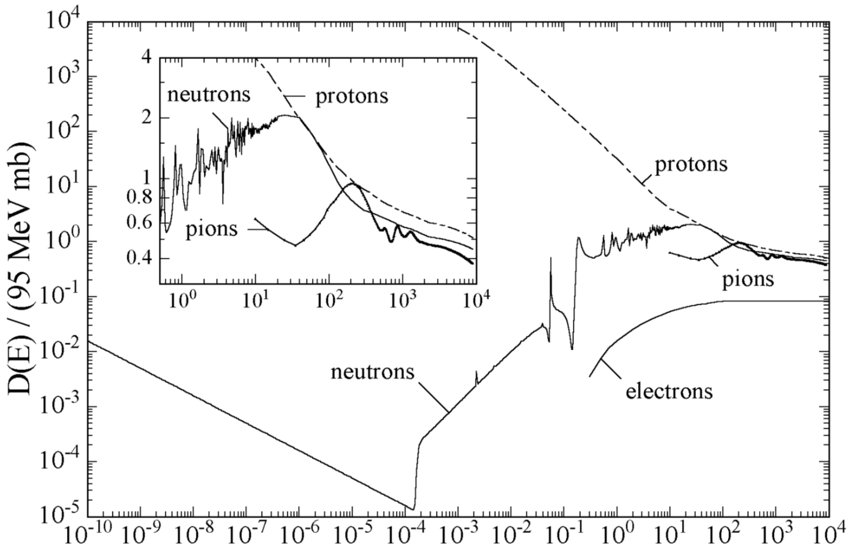

Figure 3.3.2: Displacement damage cross section normalised to $D(E_n = 1MeV)$, which is equal to 95 MeV mb, as a function of energy for protons, pions, electrons, and neutrons. Taken from [79]

3.3.3 Defect classification

As mentioned above, traversing high energy particles will induce point defects, and if sufficiently large energy is transferred to the silicon crystal, cluster defects will be created. Compared to point defects, cluster defects are less studied and the defect structure and implications on the macroscopic electrical properties of the detector are not well understood. Clusters are known to be initially composed of large regions of vacancies and interstitials, and contribute to the recombination rate of minority carriers. Recent studies have shown how certain defect centres of the clusters contribute to the space charge region, both with initial donor defects, as well as deep hole traps that become apparent after substantial annealing [86, 88]. Point defects, on the other hand, are better understood, and this section aims to introduce the most relevant defects and some of their implications to detector operations.

Point Defects

As a PKA with sufficiently large energy cascades through the silicon bulk, it knocks out silicon atoms along its path from their lattice positions causing vacancies in the lattice and interstitially located silicon atoms. These vacancies, V, and interstitials, I, are known as primary defects. At room temperature, these primary defects are mobile and diffuse around in the bulk. This creates the possibility for the I and the V to merge again, effectively restoring the silicon lattice, but also allows for subsequent reactions with other defects or impurities in the lattice. These other reactions can form permanent defects, and some that electrically active and macroscopically alter the characteristics of the silicon detector if they are generated in sufficiently large concentrations. A non-exhaustive range of different possible reactions are listed in table 3.3.2 below. In an n-doped silicon bulk, reactions with Phosphorus are also common, however, as Boron-doped chips are the only samples investigated in this study, the P reactions are omitted from the list.

Primary Vacancies	Primary Interstitials	Replaced impurities
$V + B_s \rightarrow VB_s$	$I + B_s \rightarrow B_i$	$B_i + O_i \rightarrow B_iO_i$
$V + O \rightarrow VO$	$I + VO \rightarrow O$	$C_i + C_s \rightarrow C_iC_s$
$V + V \rightarrow V_2$	$I + V_2 \rightarrow V$	$C_i + O_i \rightarrow C_iO_i$
$V + C_i \rightarrow C_s$	$I + C_s \rightarrow C_i$	

Table 3.3.2: A list of common possible defect reactions [93, 78]. A subscript i denotes the atom being interstitial, and a subscript s denotes the atom being a substitute to a Si atom in the lattice. V_2 is a divacancy.

The various point defects created are generally classified according to their electrical properties. Defects that introduce energy levels inside the band gap may capture or emit electrons and holes. Defects that are neutrally charged when occupied by an electron are called *donors*, and defects that are negatively charged when occupied by an electron are called *acceptors*. Naturally, this encompasses normal semiconductor doping as described in chapter 2, but also includes any defect complex that has the same behaviour. However, not all defects classified as acceptors or donors contribute to altering the resistivity of the semiconductor. Charge occupation of a defect is dependent on the defect energy level E_t in the band gap. Donors with $E_t > E_F$ and acceptors with $E_t < E_F$ are ionised at equilibrium and will thus contribute to the space charge. As seen in figure 3.3.4, common doping elements, B_s and P_s as well as the the donor like B_iO_i defect contribute to the space charge, while acceptor defect VO_i and donor C_iO_i do not. As can also be seen in image 3.3.4, some defects introduce multiple energy levels, one being the thermal donor complex O_4, which is explained above as a double donor, that introduces two energy levels. With both of these energy levels being above E_F, the thermal donor contributes to the space charge at room temperature.

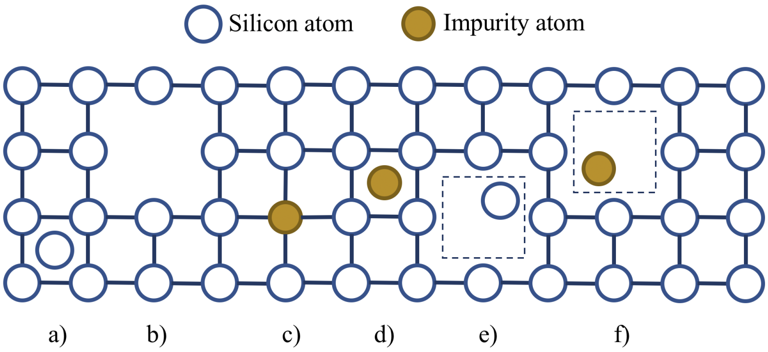

Figure 3.3.3: Example of possible common defects. a) Interstitial silicon atom, *I*. b) Lattice vacancy, *V*. c) Substitutional impurity atom. This also includes doping agents, e.g. B_s. d) Interstitial impurity atom, e.g. O_i. e) Frenkel Pair. f) Interstitial impurity atom and vacancy, e.g. VO_i complex. The silicon lattice presented here is greatly simplified, and in reality silicon has a diamond lattice type [71].

In addition to contributing to the bulk space charge, some defects introduce energy levels close to the middle of the band gap. These mid-levels assist in the generation and recombination of charge carriers. These transitions are facilitated in steps of electron and hole capture or emissions. In the depletion region where the amount of free carriers are negligible, these mid-levels almost exclusively facilitate generation of carriers, while on the other hand, in the non-depleted area the amount of free carriers is reduced by the mid-levels assisting in recombination.

Another important implication of the presence of defects is the so-called trapping of charge. All defects can capture electrons or holes, however, defects with energy levels close to either of the two bands might temporarily trap and subsequently re-release a moving charge carrier. When the emission time exceeds the readout time of the detector, there will be a loss in signal due to trapped charge carriers. Early CMOS detectors that relied on diffusion had limited radiation tolerance due to this fact. With diffusing charge carriers taking significantly longer to be collected compared to drifting charge carriers, the effect of losing signal due to trapping is significant and used to be the main limiting factor for the use of CMOS-based detectors in high energy physics [84].

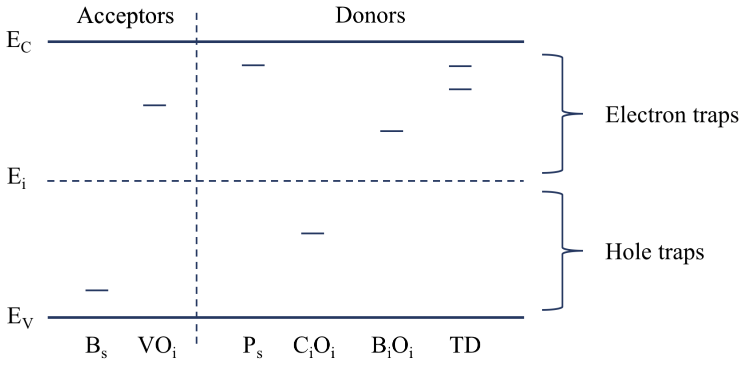

Figure 3.3.4: Energy levels introduced into the band gap by various defects. Not to scale.

Apart from their electrical properties, the defects can be divided into three groups depending on their behaviour after they are created:

- Stable defects, not changing over time
- Defects decaying into other kinds of defects, this process is known as dissociation
- Defects reacting with other defects to form new defects

The defect concentration, N_i, of a given defect i, either a primary defect or a defect generated through dissociation or a reaction from two other defects, is given by the relation:

$$N_i = g_i \Phi_{eq} f_i \tag{3.3.4}$$

Where g_i is the introduction rate and f_i describes the evolution of the defect. Stable damage implies $f_i = 1$, while dissociation defect production is a first order process thus

f_i becomes a function of time. The third group of defects can be described through a second order process, and f_i will depend on both time and Φ_{eq}. In case one of the two defects reacting has a significantly higher initial concentration, the reaction will be reduced to a first order process [58]. It should also be noted that the probability of both dissociation and reaction depends directly on the the lattice vibration energy, which is governed by Maxwell-Boltzmann distribution. Following this, the probability of dissociations and reactions increases with increased temperature. Furthermore, the introduction rate of defects is highly dependent on initial impurity concentrations and the type and energy of irradiation. While most introduction rate investigations have been done on FZ silicon, table 3.3.3 below show some values for common defects in MCz silicon for two kinds of irradiations. It should be noted that while similar Cz and MCz have differences in impurity concentrations and thus these introduction rates cannot be taken to be the same for the samples used in this study.

Defect	26 MeV Protons [cm^{-1}]	Reactor neutrons [cm^{-1}]
IO_2	1.33	0.21
VO	3.5	0.46
V_2	0.69	0.31
C_iO_i	1.18	0.95

Table 3.3.3: Introduction rates of selected defects in 8 kΩcm MCz silicon for two different irradiation sources. From [48].

3.4 Macroscopic effects

After significant irradiation of the silicon detector, the above-mentioned microscopic defects will cause changes in the macroscopic behaviour of the detector. The majority of these changes are seen as negative and hamper effective operation of the detectors, but later we will see that some of the effects might possibly be used to improve performance.

3.4.1 Leakage current

The leakage current generated inside the bulk under reverse bias in a silicon detector is given as:

$$I_{bulk} = \frac{q\omega A n_i}{\tau_g} \tag{3.4.1}$$

Where A and ω make up the area and depth of the depleted volume, n_i the intrinsic carrier concentration and τ_g the lifetime of generated carriers. The bulk leakage current before irradiation in a reverse biased abrupt PN junction consists of two components: the diffusion of charge carriers in the non-depleted region and the generation of charge carriers in the depletion region. The contributions of the two components depend on n_i, which is comparatively low for non-irradiated silicon [71]. This means that the majority of the leakage current before irradiation in silicon is due to the thermal emission of charge carriers in the depletion region. After irradiation, due to the increased carrier generation through the assistance of mid-gap energy levels, the leakage current will also increase. Considering the majority of generated charge carriers in the bulk coming from the introduced defects the change in leakage current is proportional to the fluence and can be described as

$$\Delta I_{bulk} = \alpha\omega A\Phi_{eq} \tag{3.4.2}$$

where α is introduced as proportionality factor and is called *current related damage rate*. As the amount of defects is linearly dependent on the irradiation fluence, we see that the leakage current is linearly dependent on the fluence for a given depletion volume. However, as we will see below, the irradiation changes the effective doping concentration and consequently the depleted volume. Hence the leakage current of a detector where full depletion is never reached might deviate from a linear behaviour to the fluence for a fixed bias voltage. This increase in leakage current is a limiting factor for operating conventional detectors. A significantly large leakage current may drown out the signal, or cause thermal runaway[2] in the chips. This is traditionally circumvented by cooling the detectors to reduce thermally generated charge carriers. The temperature dependence of the generated current can be derived from eq. 3.4.1. In the irradiated detector, n_i is proportional to the temperature such that:

$$n_i\left(T\right) \propto T^{3/2}\exp\left(-\frac{E_g + 2\Delta}{2kT}\right) \tag{3.4.3}$$

Where Δ is close to the absolute value of the difference between trap energy level and the E_F. Only traps with energy levels close to the E_F are considered, as they are the predominant contributors to generated charge carriers, which leads to τ_g being proportional

---

[2] An uncontrolled positive feedback process where the increased leakage current causes an increase in temperature, which in turn increases the leakage current further.

to $1/\sqrt{T}$. More details can be found in [71, 22]. Following this, we get the temperature relation for the leakage current in an irradiated detector to be proportional to:

$$I_{bulk} \propto T^2 \exp\left(-\frac{E_g + 2\Delta}{2kT}\right) \tag{3.4.4}$$

While maximum generation is caused by defects with energy levels equal to the Fermi level, measurements show that the average energy level value of all contributing defects to be slightly deviating from E_F. The effective energy, $E_g + 2\Delta$, for the irradiated detector around 300 °K is approximately 1.2 eV, deviating from the standard 1.12 eV of an un-irradiated detector [22, 79]. While we can see that a low temperature has a significant effect on the leakage current, it should be noted that the large leakage currents that follow increasingly high fluences require increasingly complex cooling systems to reach low operation temperatures, which poses both construction and budget challenges in new detectors.

3.4.2 Trapping and signal loss

Another significant change in device behaviour after irradiation is the loss in signal due to the trapping of charges. As defects and impurities introduce levels in the band gap, these levels act as traps for the drifting charge carriers. As described above, the signal is generated by the movement of charge, making a trapped charge carrier not contributing to the signal for the duration of trapping. All defects have a probability of trapping either electrons or holes. However, in the depletion region defects with energy levels above the Fermi level act as electron traps, and defects with energy levels below the Fermi level act as hole traps. The effective probability of charge trapping can be defined as the inverse of the effective carrier lifetime, τ_{eff}. The charge carrier lifetime is proportional to the inverse of the velocity. Considering that the thermal velocity is much larger than the drift velocity in our case, the effective trapping probability can be expressed as the sum of the probabilities of getting trapped by all present defects such that [61]:

$$\frac{1}{\tau_{eff}} = \sum_i N_i \left(1 - P_i\right) \sigma_i v_{th} \tag{3.4.5}$$

Where, N_i is the concentration of defect i, P_i is the occupation probability, σ_i is the capture cross-section, and v_{th} is the thermal velocity. Generally, P_i can be considered temperature-dependent and σ_i temperature-and velocity-dependent. For limited fluences, the introduced defects will be limited to first order processes as described in section 3.3.3, and using eq. 3.3.4 we can rewrite eq. 3.4.5 and $1/\tau_{eff}$ can be parametrised as:

$$\frac{1}{\tau_{eff}} = \beta_{e,h}\left(t,T\right)\Phi_{eq}, \quad where \quad \beta\left(t,T\right) = \sum_i g_i f_i(t)\left(1-P_i\right)\sigma_i v_{th} \tag{3.4.6}$$

β can be regarded as an effective trapping damage constant for irradiation. Finally, the reduction of drifting charge carriers after irradiation can be expressed as:

$$Q(t) = Q_0 \exp(-t/\tau_{eff}) = Q_0 \exp(-t\beta\Phi_{eq}) \tag{3.4.7}$$

Here Q_0 is the initial amount of introduced charge carriers, is reduced exponentially due to trapping. The trapped charge can then either spontaneously recombine or be re-emitted. If the re-emission time of a trapped charge carrier is less than the total readout time of a detector, it may contribute to the signal again. Recombination results in permanent reduction of signal.

3.4.3 Effective doping concentration

Normally, the doping concentration of a silicon chip is given by the concentration of added doping agent, commonly boron or phosphorous for p-doped or n-doped materials, respectively. As described in section 3.3.3, some energy levels introduced by defects after irradiation act either as donors or acceptors in the space charge region. At sufficiently large concentrations these electrically active defects will alter the space charge, such that a new effective doping concentration can be defined as:

$$N_{eff} = \sum_{acceptors} N_i P_i - \sum_{donor} N_i\left(1-P_i\right) + N_A - N_D \tag{3.4.8}$$

The negative sign on donor defects and N_D is due to assuming initially p-doped silicon. Normally, either N_A or N_D can be neglected depending on the initial doping. Apart from the introduction of electrically active defects, the initial doping can also be reduced due to irradiation. Similarly to the trapping probability, this can be rewritten using eq. 3.3.4

to:

$$N_{eff} = \Phi_{eq}\left(\sum_{acceptors} g_i f_i P_i - \sum_{donor} g_i f_i \left(1 - P_i\right)\right) + N_A\left(\Phi_{eq}\right) - N_D\left(\Phi_{eq}\right) \tag{3.4.9}$$

With significant introduction of electrically active defects, changes in the space charge region of the device will be apparent. This change will alter the depletion region, whose width is dependent on the space charge of the bulk. Following irradiation, eq. 2.1.11 has to be updated to account for the introduced defects, and the PN junction depletion width will be dependent on the absolute value of $\mathrm{N_{eff}}$:

$$\omega \approx \sqrt{\frac{2\epsilon_{Si}\epsilon_0}{q|N_{eff}|}V_{bias}} \tag{3.4.10}$$

It should be noted that this is only an approximate relationship, as an irradiated detector has inhomogeneous space charge distribution and complex electric field distribution. N-doped silicon detectors, similar to the ones used in the current Inner Tracker of ATLAS is, experience a large removal of initial donor levels and an introduction of acceptor-like defects when exposed to irradiation. After sufficiently large irradiation, n-type silicon has shown to undergo a so-called *space charge sign inversion*, SCSI, where $\mathrm{N_{eff}}$ changes sign, effectively making it a p-type silicon [67]. P-type silicon on the other hand has not been studied to the same extent as n-type silicon. Recent findings hint at high-resistivity[3] p-type silicon also undergoing SCSI for fluences greater than $7.3 \cdot 10^{14} n_{eq}/cm^2$ [78, 28], however, this is not seen in the low resistivity samples used in this study. The initial change in $\mathrm{N_{eff}}$ in p-type silicon is largely attributed to complete or near complete removal of the initial acceptors, through what is known as *acceptor removal.*

Acceptor removal

When a boron substitutional, B_s, the common p-doping agent, is knocked out of its lattice position, either through direct knock-out or reacting with an I, it loses its acceptor property. Furthermore, B_i tend to react with other defects to form defect complexes, such as B_iO_i or B_iI, neither of which have acceptor like behaviour. Rather, the B_iO_i defect shows double-donor-like behaviour, accelerating the reduction of $\mathrm{N_{eff}}$, and is stable at temperatures below 170 °C [78]. Similar to an n-doped crystal, there is introduction of acceptor-like defects, however, this process is dominated by the acceptor removal effect. Instead of using eq. 3.4.9, the $\mathrm{N_{eff}}$ for B doped silicon can be simplified to the

---

[3] 50 - 1000 Ωcm.

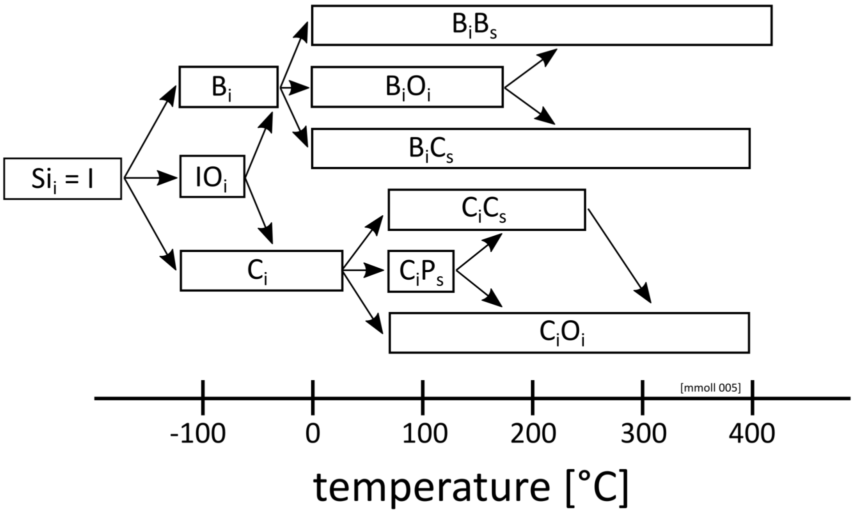

Figure 3.4.1: reaction paths for B_iO_i and C_iO_i, and stability range of the different defects. From [78].

formula:

$$N_{eff} = N_{eff,0} - N_{c0}\left(1 - \exp\left(-c\Phi_{eq}\right)\right) + g_c\Phi_{eq} \tag{3.4.11}$$

Here $N_{eff,0}$ represents the initial doping concentration, generally, equal to the boron concentration in p-doped silicon. N_{c0} is the maximum amount of acceptor removal, where complete removal implies $N_{c0} = N_{eff,0}$, c is the acceptor removal factor and g_c is the acceptor-like defect generation rate.

Additionally, carbon interstitials, C_i are known to suppress the acceptor removal effect [62]. C_i are created either through an I pushing a C_s out, or by being knocked out of its lattice position, and can, similarly to B_i, react with the defect O_i to form C_iO_i. This process is in direct competition with the B_iO_i process and if the initial Carbon concentration is large, it can reduce the effect of acceptor removal. Figure 3.4.1 shows the reactions through which these defects are formed. It should be noted that the C_iO_i, while reducing the acceptor removal rate, also has donor-like properties and contributes to changing $\mathrm{N_{eff}}$.

Thermal Donor dependant doping concentration

As explained above, most silicon-based detectors utilise FZ silicon to achieve suitable characteristics for use in particle detection. However, more recently detector-grade silicon has been produced by a refined Cz technique [18], called Magnetic Czochralski. Additionally, with the introduction of active CMOS circuitry directly in the sensing silicon, conventional Cz silicon also becomes an option in the production of detectors. While the oxygen and carbon impurity concentrations in FZ silicon are sufficiently low to allow the thermal donor process to be ignored during manufacturing and post-processing steps, detectors using MCz or Cz silicon can be directly affected by the thermal donor generation process due to their high O concentration. High resistivity p-type MCz silicon based detectors have been shown to undergo SCSI after high-temperature annealing of less than two hours, implying the significant effect thermal donors can have on Cz or MCz silicon based detectors. This was done in both $p^+/p^-/n^+$ and $n^+/p^-/p^+$ detectors annealed at 430 °C [101, 41, 16]. Here, p-type bulk silicon detectors with initial doping concentrations in the order of $7 \times 10^{12} cm^{-3}$ and oxygen concentrations around $7 \times 10^{17} cm^{-3}$ showed to be effectively n-type after approximately 1 hour of annealing. Continuous annealing following this increases the N_{eff} again, making the detector more p-type-like. Analogously to this, and following the introduction rates stated in section 3.2, HV-CMOS sensors using Cz silicon are expected to be affected by the introduction of TDs. However, this appears to not be so clear as will be seen in chapter 7.

3.5 Annealing

Defects introduced by the irradiation can, as described above, move around in the lattice and combine with other defects to create new defect complexes. The probability of these processes are largely governed by the temperature, and change in detector parameters due to the formation of new defects post-irradiation can be seen as a function of time at elevated temperatures, so-called annealing. The effects of annealing after irradiation differ depending on what detector parameters one is looking at.

Leakage current

Annealing of the silicon detector following irradiation with hadrons decreases the elevated leakage currents, regardless of the space charge state of the detector. This change of leakage current after annealing can be captured by extending α, introduced in eq. 3.4.2, to also account for annealing temperature, T_A and time of annealing, t. Early studies done at room temperature reported an initial decrease of α followed by saturation, and parametrised α as a sum of exponentials multiplied with a saturation constant. However, prolonged annealing, $t >$ a year at room temperature, has shown a continuous decrease. This is also seen in longer annealing times at elevated temperatures, and instead of a saturation constant the decrease in leakage current taking place at these long time intervals has been found to follow a logarithmic function in time, however, there is no clear physical explanation for it [80]. α can then be parametrised as

$$\alpha\left(T_A,t\right)=\alpha_I\exp(-t/\tau_I)+\alpha_0-\beta\ln(t/t_0) \tag{3.5.1}$$

Where α_I is $1.23\cdot10^{-17}$ A/cm and β is $3.07\cdot10^{-18}A/cm$. Both τ_I and α_0 are annealing temperature dependent parameters and was found in to follow

$$\tau_I=exp\left(\frac{12.9\cdot10^3}{T_a}-34.1\right)min \tag{3.5.2}$$

and

$$\alpha_0=-8.9\cdot10^{-17}A/cm+4.6\cdot10^{-14}AK/cm\cdot\frac{1}{T_a} \tag{3.5.3}$$

τ_I is derived from an Arrhenius equation with an activation energy of 1.11 eV. It should be noted that this parametrisation of α only holds for the temperature range 21 - 106 ◦C and times above 1 minute [80].

Effective doping concentration

In contrast to the leakage current, the evolution of the effective doping concentration over longer periods of time do not show a decrease or increase in one direction. N-doped silicon, similar to what is used in ATLAS and CMS, show an initial decrease of space charge, to then subsequently start to increase again after reaching a minimum, as can be seen in figure 3.5.1 below. At room temperature the initial decrease until the minimum takes a few days, while the subsequent increase plateaus after approximately a year [59]. While studied to a lesser extent, similar characteristics have also been seen for p-doped silicon [28, 60]. Following this evolution, the change of N_{eff} with annealing can be described by the so called *Hamburg model* which divides it into three components:

- Defects whose influence on the space charge region disappear on a short time scale. This component is referred to as the *short-term annealing* or *beneficial annealing* part. The term *beneficial annealing* comes from the fact that N_{eff} decreases after a short annealing period in n-doped silicon that has undergone SCSI.

- A component that represents stable damage, unaffected by any annealing of the detector.

- A component that introduces more defects of the opposite doping type compared to the initial value, after long term annealing. This component is commonly called the *reverse annealing.*

The change in N_{eff} can then be expressed as:

$$\Delta N_{eff} = N_{eff,0} - N_{eff} = N_c\left(\Phi_{eq}\right) + N_a\left(\Phi_{eq}, t(T_a)\right) + N_Y\left(\Phi_{eq}, t(T_a)\right) \tag{3.5.4}$$

The stable damage, N_c, can be assumed to be similar to the acceptor removal and introduction expressed in eq. 3.4.11.

$$N_c = N_{c0}\left(1 - \exp\left(-c\Phi_{eq}\right)\right) + g_c\Phi_{eq} \tag{3.5.5}$$

Whilst the beneficial annealing and reverse annealing parts can be expressed as:

$$N_a = g_a\Phi_{eq}\exp(-\frac{t}{\tau_a})\,, \quad N_Y = g_Y\Phi_{eq}\left(1 - \exp\left(-\frac{t}{\tau_{ra}}\right)\right) \tag{3.5.6}$$

g_a and g_Y represent the introduction rate of the corresponding defects accompanying beneficial and reverse annealing, respectively, and τ_a and τ_{ra} represents the time scale for the introduction of these defects. The evolution of ΔN_{eff} for an n-doped standard silicon sample that has undergone SCSI and how it is related to the parameters of the Hamburg model is highlighted in figure 3.5.1.

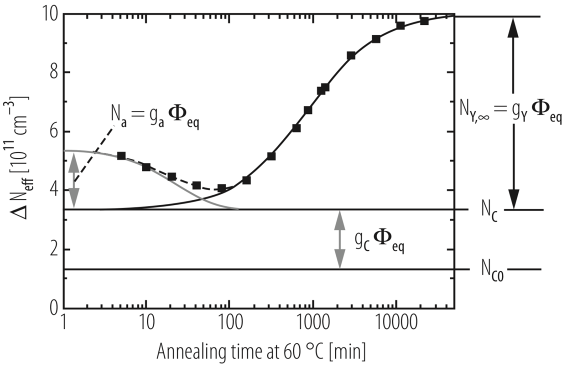

Figure 3.5.1: Evolution of ΔN_{eff} over time at 60 °C. From [59].

Trapping probability

While the trapping probability of electrons and holes is relatively similar right after irradiation, the time evolution affects these values differently. The trapping probability of electrons decreases with time after irradiation. On the contrary, the probability of holes being trapped increases with time after irradiation. Within normal operation temperatures, −20°C and 20°, the trapping probability varies by up to 20% [61].

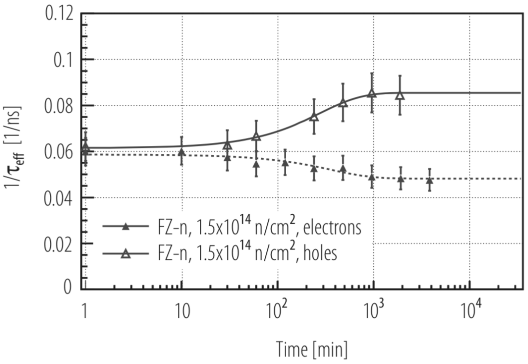

Figure 3.5.2: Time evolution of effective trapping time for electrons and holes in neutron irradiated silicon after annealing at 60 °C. From [59].

Chapter 4

HV-CMOS prototypes

Numerous prototypes have been developed in different frameworks in the pursuit of developing a monolithic pixel chip for future high energy physics experiments. One of the frameworks was commissioned by the ATLAS collaboration in 2011 to develop a radiation hard CMOS technology based pixel chip to be used in the new pixel detector for the HL-LHC. Under this framework 6 different chips were produced at AMS[1] using their 180 nm High Voltage CMOS process, (a)H18. Two iterations of these chips are investigated in this study. While ATLAS ultimately decided to not use monolithic pixel chips in the upcoming pixel detector due to time constraints, the technology is still highly desirable for future trackers due to the potential for better granularity, lower production costs and thinner detectors compared to the conventional hybrid pixel detector. The Mu3e experiment at PSI[2] will be using HV-CMOS sensors, and other experiments, such as LHCb and CLIC are considering using HV-CMOS as well. With future HEP experiments in thought, the RD50 collaboration has initiated a framework for developing radiation tolerant HV-CMOS sensors. The RD50 sensors are exploring the 150 nm CMOS technology, LF150, offered by LFoundry[3]. Two prototype chips have been developed so far, and a third is in the design stage at the time of writing. These two prototypes were investigated in this study.

---

[1] Austria Micro Systems, `https://ams.com/ams-start`

[2] Paul Scherrer Institute, `https://www.psi.ch/en`

[3] `http://www.lfoundry.com/`

4.1 Capacitively Coupled Pixel Detector Prototypes

In the pursuit of a radiation tolerant CMOS based chip for the future ATLAS upgrade, a CMOS collaboration framework was initiated in 2011 to explore suitable technologies for such a chip. While developing a MAPS was one of the main goals, the prototypes were also made to be able to connect capacitively to readout chips. Following the introduction of a new front end chip, the FE-I4 [37], that had been developed for the IBL upgrade of the current ATLAS detector, the CMOS prototypes were designed to match the readout pixels of the FE-I4 for particle beam testing. All of these prototypes, denoted either CCPD[4] or HV2FEI4[5], were manufactured at AMS using the their aH18 CMOS process with their standard 20 Ωcm Cz silicon wafer. The aH18 process guarantees operations up to 60V [99]. The thickness of both CCPD chips below is 250 μm. There is no backside processing, and bias voltage is supplied from p-implants on the top surrounding the deep n-wells.

4.1.1 CCPDv3

The third iteration of the CCPD chip, the CCPDv3, was developed in collaboration with the CLIC[6] community. The chip features a 64 × 64 active pixel matrix, with monolithic readout in addition to the capacitively coupled alternative [99]. The pixel size is $25 \times 25\ \mu\text{m}^2$, containing a deep n-well housing active CMOS circuitry. The small pixel pitch was chosen to address the CLIC requirement of high granularity. Designed with the CLICpix[7] in mind, the majority of pixels contain two amplifications stages, but lack any discriminator [51]. The chip also contains a $100 \times 100\ \mu\text{m}^2$ passive pixel diode, only consisting of the deep n-well implant without any active circuitry, near the edge of the detector. The placement is highlighted on the right in figure 4.1.1. This passive pixel is used in this study to investigate the irradiated samples through the eTCT technique explained in section 5.4.

The diode structure has two dedicated wire bonding pads, denoted DioNW and DioSub on the right in figure 4.1.1. However, earlier measurements on this chip used the Sub pad, which is the pad for supplying high bias to the pixel matrix, for biasing the diode. The same connection scheme is replicated in this study. DioNW is used for signal readout,

---

[4] Capacitively Coupled Pixel Detector, this denotation will be used onwards

[5] High Voltage To FEI4

[6] Compact Linear Collider

[7] A readout demonstrator developed for CLIC.

high bias is supplied to Sub, and the three red pads which are used to ground the active pixel matrix are connected to shared ground on the PCB.

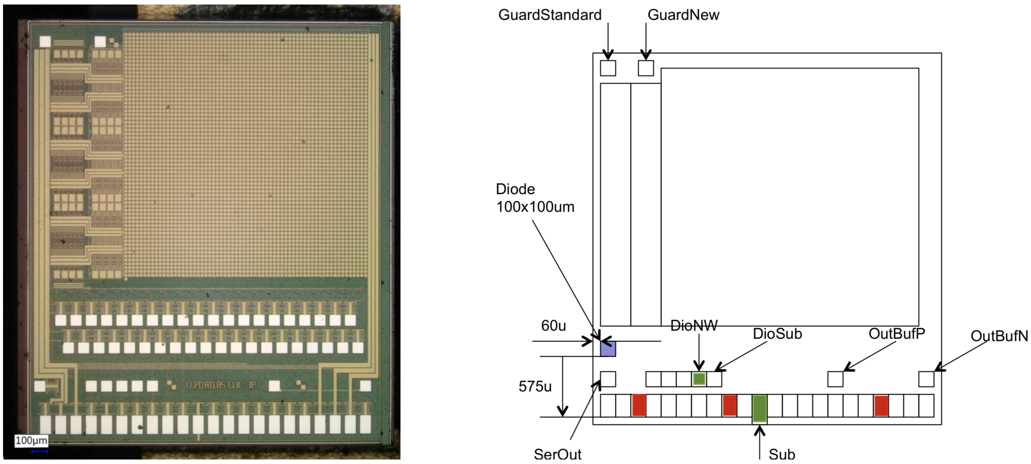

Figure 4.1.1: Top view of the CCPDv3 layout. Left image taken with a Keyence VHX-5000 microscope. The passive test structure is found on lower left side, named diode in the drawing, and is not visible in the picture.

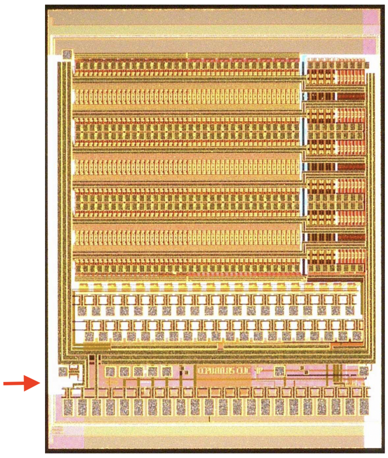

Figure 4.1.2: Top view of the CCPDv4 layout. Red arrow highlights the position of the passive test structure.

4.1.2 CCPDv4

The CCPDv4 was done without collaboration with the CLIC community and thus has slightly different pixel features. This chip features 125 × 33 μm^2 pixel pitches, and was designed to connect capacitively to the FE-I4. The majority of pixels in the CCPDv4 implements a two-stage amplification, but in contrast to its predecessor it also includes a discriminator with tunable output amplitude [13]. Similar to its predecessor, a passive pixel diode is also provided on the CCPDv4 for eTCT measurements. The placement of this diode is similar to the CCPDv3, and is highlighted in image 4.1.2. This chip has the same wire bonding pad layout as the CCPDv3, and for consistency, the same wire bonding scheme was followed for reading out the passive structure as described in the previous section.

4.2 RD50 prototypes

After the ATLAS collaboration decided to not implement CMOS technology in the ITk upgrade, the RD50 collaboration initiated a small working group to research HV-CMOS chips for future tracking detectors. As mentioned above, two prototype chips have been developed so far, using the 150 nm HV process offered by LFoundry. Both chips were manufactured during MPW[8] runs, meaning that no backside processing was possible. This implies that only top biasing is possible, and all readout has to be done from pads on the top. Both chips are developed to be full MAPS, and are not intended for connection to readout chips in contrast to the CCPDv3 and CCPDv4 above.

4.2.1 RD50-MPW1

The first prototype submitted by the RD50 collaboration features a 5.21×5.17 mm^2 large die with two flavours of pixel matrices, see figure 4.2.1. One of the pixel matrices is dedicated to photon counting applications, and the other pixel matrix is aimed at particle physics experiments. The pixel matrix aimed at particle physics experiments have the possibility of both analog and digital readout, and features 3120 50×50 μm^2 pixels. The analog readout electronics contains a CSA[9], a source follower, high-pass filter and comparator featuring a 4-bit DAC for offset compensation. The digital readout includes an edge detector, processing logic, a ROM storing the pixel address, and a DRAM that stores signal information. More details on the pixel design can be found in [104].

The RD50-MPW1 also features two passive test structures included for TCT and eTCT measurements. One 3×3 matrix with 50 μm pixel pitch and one 2×3 matrix with 75 μm pixel pitch. However, only the 50 μm pixel structure was used in this study. The test structures are completely separated from the active pixel matrices apart from sharing the same bulk and have dedicated connection pads. The passive test structure contains the same p- and n-implants used in active matrix where the NMOS and PMOS are placed. A simplified cross-section of the implant structure can be seen in figure 4.2.2.

---

[8] Multi Project Wafer

[9] Charge Sensitive Amplifier

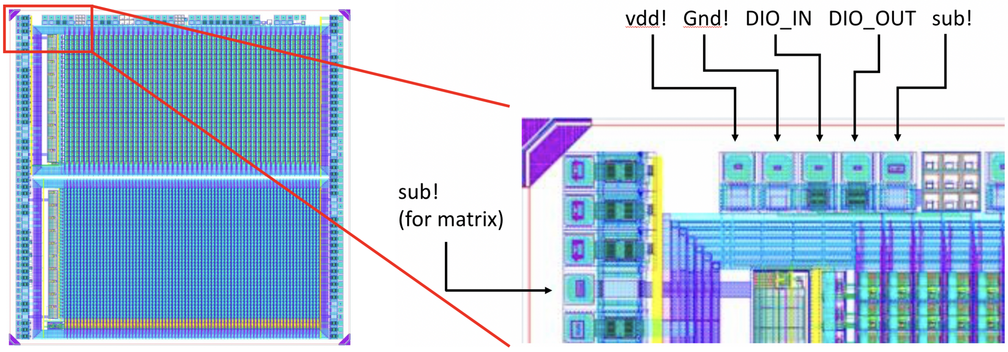

Figure 4.2.1: Top view of the RD50-MPW1 layout. On the left the two different pixel flavour matrices can be seen divided into upper and lower regions. The 3 by 3 passive pixel test structure is visible on the right, with its dedicated wire bonding pads.

The dedicated pads for the test structure are highlighted on the right in figure 4.2.1, and the 3 × 3 pixel test structure is visible on the far right as 9 white squares. *vdd!* and *gnd!* can be used for different leakage current measurements but are left floating during eTCT measurements done in this study. *DIO_IN* connects to the signal readout of the central pixel of the test structure. The remaining 8 pixels surrounding the central pixel are shorted together and the signal readout is connected to *DIO_OUT*. *sub!* in figure 4.2.1 corresponds to HV in figure 4.2.2 and is where the bias voltage was initially meant to go. Due to an unknown fault the *sub!* pad for the test structure does not work. A workaround is to leave this pad floating, and connect the bias pad intended for the active pixel matrix. Sharing the same bulk, this should not affect the operation during reverse biasing of the sensor.

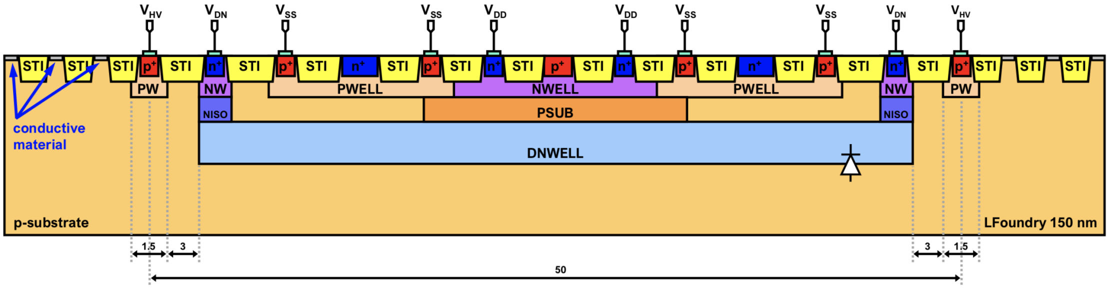

Figure 4.2.2: Simplified structure of the implants used in the 50 μm pixel. Figure taken from [34].

During the first submission of the RD50-MPW1, dies were only produced on 500 Ωcm and 1900 Ωcm substrates. A second submission was made for this study, and the chips used here have a bulk resistivity of 10 Ωcm, which is the standard LF15 substrate resistivity.

4.2.2 RD50-MPW2

Initial measurements of the RD50-MPW1 revealed unexpectedly large leakage current during reverse bias, which prompted development of a second HV-MAPS prototype. The second prototype, called RD50-MPW2, follows a similar design to the first prototype with regards to active matrix design, but the chip itself was designed to be of a smaller scale. The digital readout option was removed, and only analogue readout through a multiplexer is available. It was produced on four different resistivities; 10 Ωcm, 200 Ωcm, 1.9 kΩcm, and 3 kΩcm. With focus on low resistivity CMOS, only the 10 Ωcm samples were investigated in this study. The die is 2.1 × 3.2 mm^2 in size, and contains a 8 × 8 active pixel matrix. Similar to RD50-MPW1, the active pixels contain a CSA, a source follower, a high-pass filter and a 4-bit tunable comparator. The chip also includes SEU[10] tolerant memory for testing. Please refer to [110] for more details on the active circuitry and electronics of the chip.

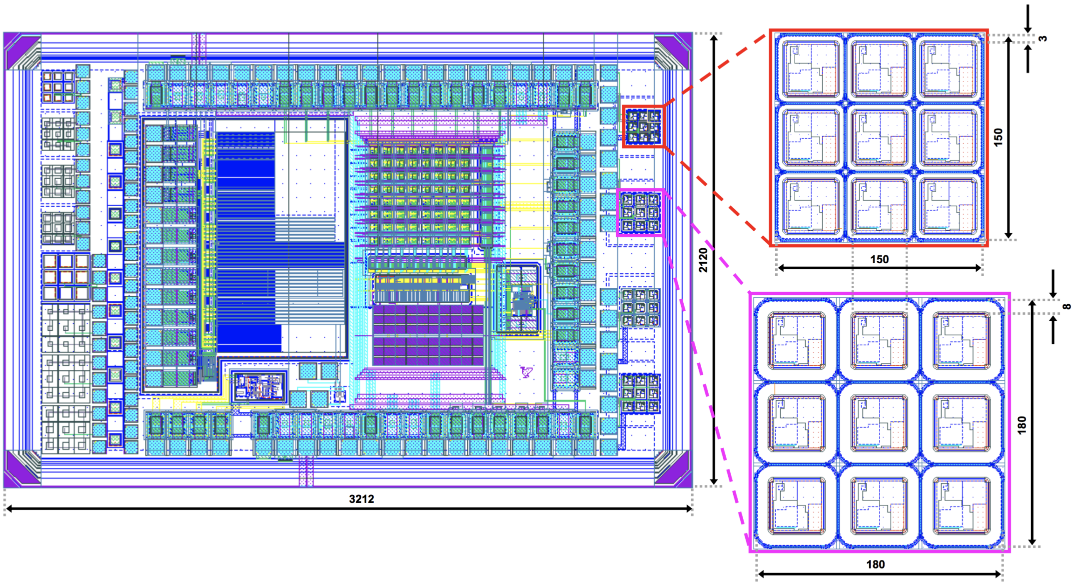

Figure 4.2.3: Overview of the RD50-MPW2 chip. Two passive 3 by 3 test structures highlighted. Both feature rounded corners, and have electrode spacing 3 μm and 8 μm respectively. All lengths are given in μm. Figure from [34].

Three design changes were made to tackle the high leakage current of the previous chip. Firstly, LFoundry adds surface structure to optimise the production which includes conductive material, believed to be partly at fault for the high leakage current. These conductive parts were placed in a p-well in the RD50-MPW2, which simulations show effectively reduces the leakage current [34]. Secondly, guard rings in form of repeating p-

---

[10] Single Event Upset

wells were added surrounding the whole chip to prevent edge effects caused by the dicing. Lastly, the electrode spacing in the pixel was increased from 3 μm to 8 μm, together with rounding of electrode corners. In figure 4.2.3, two of the four test structures are highlighted, where the upper one have 3 μm space, similar to the RD50-MPW1, while the lower one, with 8 μm spacing, have the same layout as the active pixels on this chip. These two spacings were included to compare leakage current between RD50-MPW1 and RD50-MPW2 leakage currents. However, the it has to be noted that the upper test structure, while having the same spacing, have rounded corners in contrast to RD50-MPW1s square corners. The two remaining test structures both have 8 μm spacing, but instead of rounded corners one have square corners and one have sharp 45 ° tilted corners. These two test structures were not investigated here.

Like its predecessor, RD50-MPW2 also have dedicated wire bonding pads for each test structure. A pad for *vdd!* was removed for the test structures, but the remaining four pads connect in a similar fashion to the test structure as the previous chip. Also here are the 8 pixels surrounding the central pixel shorted to each other. Please refer to figure 4.2.4 for each wire bonding pad. The *gnd!* pad was left floating during all measurements.

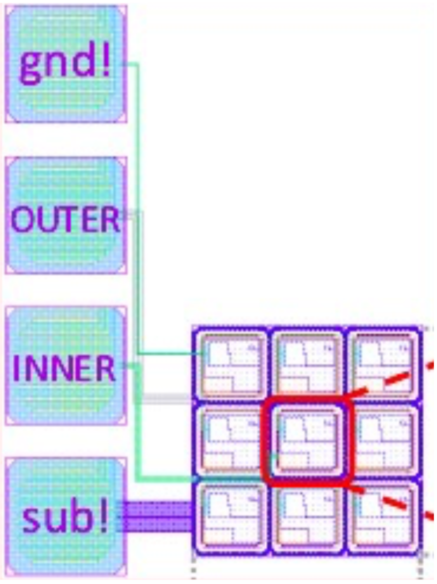

Figure 4.2.4: Pad connections for the test structures on RD50-MPW2.

Chapter 5

Experimental techniques

Characterisation of the samples was carried out using three different methods. Edge-TCT was predominantly employed for characterisation, with IV, and SIMS used in addition to provide complementary information useful to understanding the behaviour of the samples. The preparation of the samples for the TD study was done at Lancaster University using a ceramics oven, while accelerator facilities providing irradiation was used for the pre-irradiation study. These will be described in detail below, starting with the sample preparation, followed by the different characterisation techniques.

5.1 Annealing

Two different kinds of annealing treatments are done within this study. Firstly the CCPDv3 sample set underwent an isothermal annealing study after irradiation. This kind of annealing was done with a Memmert Oven 100-800, a low-temperature high precision oven. The second kind of annealing is high temperature treatment to introduce thermal donors. To achieve maximum introduction rate, the sensors have to be annealed at 450 °C. In order to reach this temperature, an LMF[1] furnace from Carbolite was acquired.

5.1.1 Post-irradiation annealing

In order to study the time evolution of defects generated by irradiation, an annealing treatment study was carried out on the irradiated CCPDv3 sample set after initial

---

[1] Ladel Metallurgy Furnace

measurements. The first annealing step was done at RT to bring all samples to an equivalent time at RT. Subsequent annealing steps were done isothermally at 60 °C, in a high precision oven. All samples were annealed together until 80 accumulated minutes at 60 °C. Two samples were then annealed and studied individually beyond this temperature. The temperature was logged using a Pt-1000 sensor connected to a Keithley 2000 multimeter once a second, and showed stable temperature control as can be seen in figure 5.1.1 below. The samples were inserted after 60 °C was reached. Temperature fluctuations were less than ±1°C, for all annealing steps.

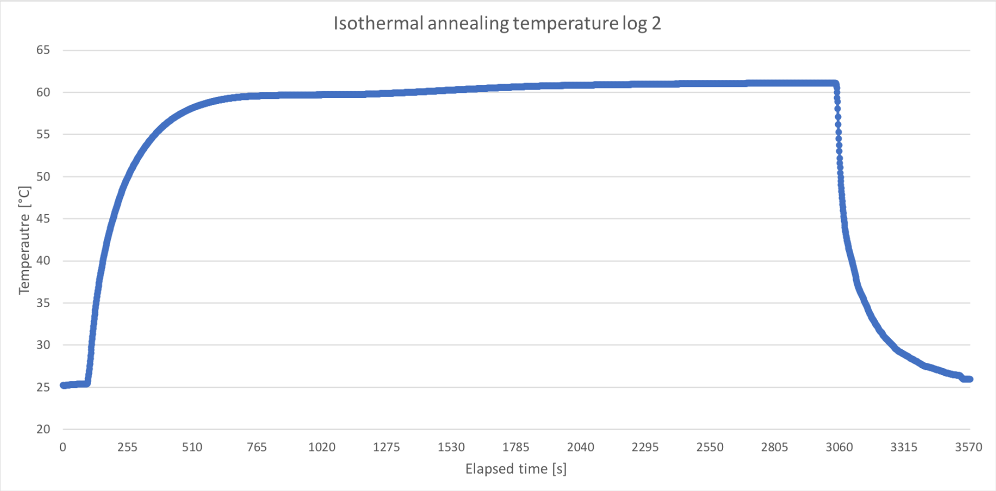

Figure 5.1.1: Temperature log during second annealing step of the whole CCPDv3 sample set in a high precision oven.

5.1.2 Furnace for TD introduction

To accommodate for the high temperatures needed for TD introduction a discontinued LMF Furnace produced by Carbolite was acquired. The furnace is capable of reaching 1200 °C using a resistance wire element wound onto a refractory muffle, and uses insulating brick and lightweight slabs for insulation. The furnace does not support infrastructure for environment control, such as nitrogen flushing. No active temperature monitoring was available, and the temperature was set using one manual knob, with markings of 50 °C increments. To ensure that 450 °C was reached, and that the furnace could hold relatively good stability, a simple temperature monitoring system was set up. A Pt-1000 sensor was crimped to a glassfiber-clad cable connected to a Keithley 2000 multimeter. The Keithley 2000 was connected to a computer via GPIB, and a simple LabVIEW script for logging temperature was written. After setting the furnace to 450 °C the temperature was monitored for over 20 hours. As can be seen in figure 5.1.2

the temperature fluctuates between 442 °C and 455 °C, with an average temperature of 445.6 °C. While stable within ±10 of 450 °C, a slight decrease of TD introduction compared to peak introduction rate has to be assumed. Similar results was achieved during the annealing steps of the samples. No clear reason was found for the sudden temperature fluctuations when investigated, and they are assumed to be due to the age of the furnace.

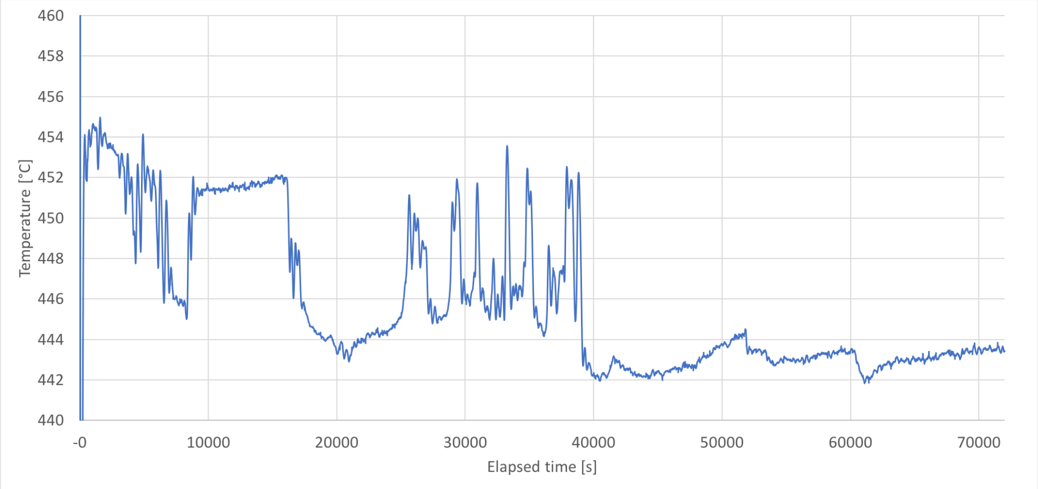

Figure 5.1.2: Temperature fluctuation in the ceramic furnace used for TD introduction. Data taken from temperature log the CCPDv3_TD5 sample.

The samples were placed in a silica crucible and covered with a smaller crucible during the annealing after preheating the oven to 450 °C. The temperature was measured with the Pt-1000 attached to the silica crucible, and reaching 450 °C takes approximately three minutes. Therefore three minutes should be added when the TD annealing is done. Each annealing was carried out individually prior to being wire bonded to test PCBs[2].

5.2 Irradiation facilities

To study the effects of radiation, naturally, the detectors have to be irradiated. While possible to do with a radioactive source, any source that is reasonably safe to handle would require a substantial amount of time to reach a fluence comparable to the background radiation in the LHC detector. Therefore, the detectors used in this study were irradiated at three different designated irradiation facilities. Two accelerator facilities were used to carry out the proton irradiation and the neutron irradiation was done

---

[2] Printed Circuit Board

with reactor neutrons. The initial proton irradiation was performed at the LANSCE[3], with 800 MeV protons. The second proton irradiation was carried out by the Bern Cyclotron Proton Irradiation facility, which provides 18 MeV protons. The reactor neutron irradiation was done with the TRIGA Mark II reactor at IJS[4] in Ljubljana.

5.2.1 Proton Accelerator at LANSCE

LANSCE is located at the Los Alamos National Laboratory, USA, and hosts a LINAC[5] capable of accelerating protons up to 800 MeV. The main use of these protons is for neutron beam production, but LANSCE also offers direct proton irradiation, with capabilities of delivering a proton beam with particle energy between 200 MeV and 800 MeV. 800 MeV protons were used in this study. The proton beam is Gaussian-like, slightly oval and has a FWHM of 1.5 and 1.2 cm along the two axes[76], however, the beam current appears homogeneous within 1cm diameter of the beam center. Irradiations are performed at room temperature, and consequently annealing effects have to be taken into account. There are currently no direct measurements of the hardness factor at this facility, although such measurements have been proposed [5], the hardness factor for 800 MeV protons is approximately 0.75 [49].

5.2.2 Bern Cyclotron Proton Irradiation Facility

The cyclotron laboratory in Bern is a multidisciplinary research facility hosting a cyclotron, produced by IBA[6], that accelerates H^- ions to 18 ± 0.36 MeV. One of the main purposes is radioisotope production for medical use, but it also has a dedicated beam transport line to a separate bunker allowing for research in parallel to the radioisotope production [9]. The facility provides a variable beam spot up to 2×2 cm^2, and has flat distribution within this area [30]. Similarly to LANSCE, the irradiations are done at room temperature. The hardness factor, κ, is 3.4885 [30].

5.2.3 TRIGA Mark II reactor at IJS

IJS in Ljubljana offers neutron irradiation with a TRIGA Mark II nuclear reactor. This facility provides neutrons up to approximately 10 MeV, and the irradiation is done by

---

[3] Los Alamost Neutron Science Center

[4] Jožef Stefan Institute

[5] Linear Accelerator

[6] `https://www.iba-radiopharmasolutions.com`

placing the samples in tubes that are inserted into the reactor core, taking the place of a fuel rod position. Two different tube size are available, with possible sample widths up to 6 cm. The neutron flux is dependent on the operating power, with $8.8 \times 10^{9} n/kW cm^{2} s$ in the small tube and $10.8 \times 10^{9} n/kW cm^{2} s$ in the large tube, with the operating power spanning a few W up to 250 kW. In the small tube, which was used in this study, the hardness factor is 0.9 [23].

5.3 IV

IV measurements were performed to determine the increase in leakage current for irradiated samples, and confirm relative fluences received by samples in the same set. The IV results presented in this study are taken during the eTCT measurements. Both TCT setups detailed below record the current automatically during measurements. The setup at Lancaster University records the current when a new bias voltage is set, and the TCT+ setup at CERN records the current for each measurement done giving more data and a more accurate value can be extracted. The DC circuit consists of a DC filter, the DUT and a resistor/inductor, detailed in figure 5.3.1.

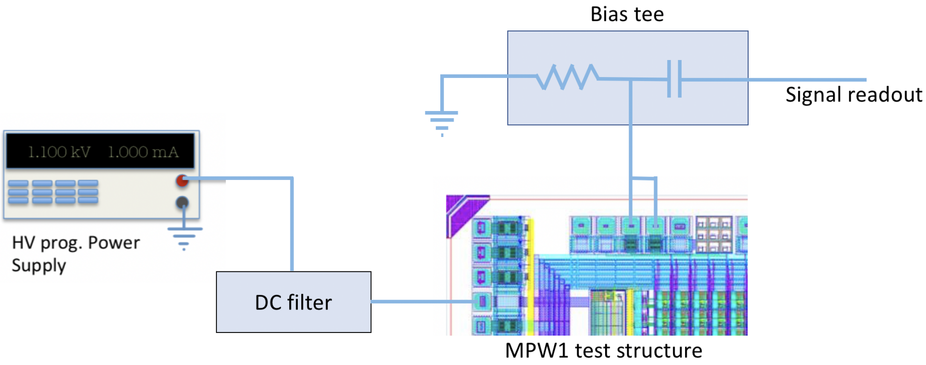

Figure 5.3.1: Example of dc circuit in the TCT setups.

5.4 eTCT

The Transient Current Technique, TCT for short, is a technique used to capture the transient current generated inside the detector due to the movement of charge carriers. The charge carriers are induced by a short laser pulse, normally on the order of picoseconds, repeated at fixed intervals. If these charge carriers are generated inside the depletion region, they start to drift and consequently induce a signal in the readout electrode, as explained in section 2.3.1. As explained in section 2.2.2, the absorption length of light depends on the wavelength. Using red light[7] charge carriers can be generated within the first couple of μm of the silicon. This is commonly used when having top or bottom illumination of a simple pad diode to visualise the internal electric field of the diode. Consider a fully depleted, simple diode with p-type bulk. If red light is injected close to the PN junction, the generated electrons will be collected almost instantly, while the holes will start drifting towards the backside electrode. The generated signal is completely generated by the drifting holes. Similarly, if the red light is injected close to the electrode opposite of the PN junction, the holes will be collected approximately immediately and the signal will be exclusively generated by the drifting electrons. However, in case of a sensor that is not fully depleted, illumination from the back side produces very limited signals as most of the generated e^-/h^+ pairs will recombine without the presence of an electric field. This is useful for studying the shape of the electric field inside the bulk and, due to the signal only having one type of charge carrier, also the electron and hole mobility can be studied.

Instead of red laser, IR laser can be used to simulate the the passing of a MIP. Due to the indirect band-gap of silicon the absorption length has a gradual decrease with longer wavelength instead of an abrupt cut off. This causes IR laser to be absorbed in the silicon over a few mm instead of μm like the red laser, generating e^-/h^+ pairs along the absorbed path. However, it should be noted that, the charge deposited by an IR laser do not fluctuate with a Landau distribution as charged deposited by a MIP do. Unlike the red laser, the signal in this case will be a superposition of the hole and electron signals generated at positions along the whole bulk.

While most HV-CMOS prototypes developed for future HEP experiments feature a passive test structure, unlike a simple test diode, the top side normally contains metallization making illumination from the top impossible. In addition the bottom is commonly unprocessed, making it necessary to avoid fully depleting the sensor, as this might cause an increase in leakage current. As such, red illumination from the back becomes virtually unusable. An alternative to top and bottom illumination is to illuminate the detector from the side. This alternative technique is called edge-TCT, or eTCT for short, and is the predominant measuring method in this work. As chips are designed to have the active region never reaching the side of a die, this illumination option is exclusive to IR lasers.

---

[7] wavelengths around 660 nm

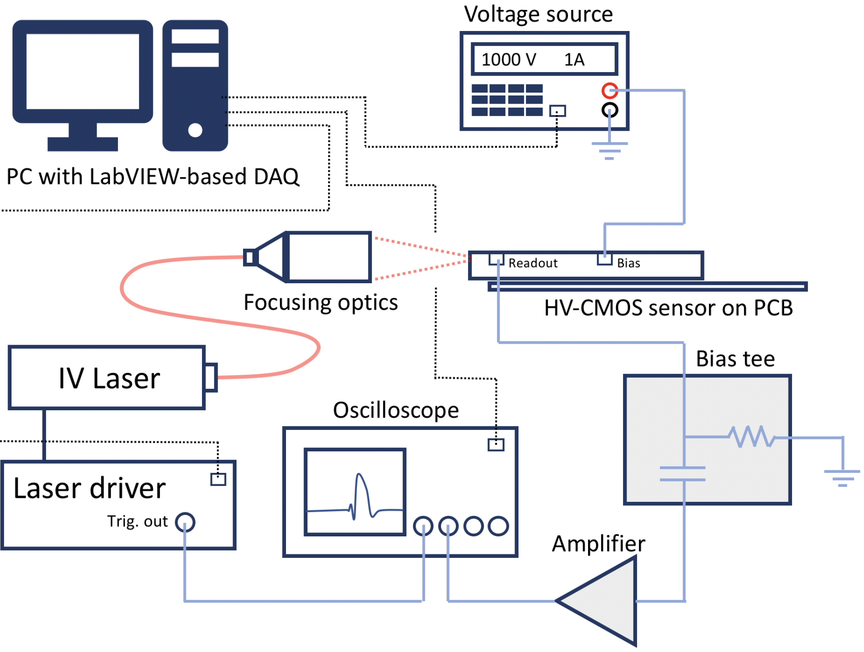

Figure 5.4.1: General layout of an eTCT setup.

Two different eTCT setups were used in this study and will be described in detail below. The main idea is the same, but there are some discrepancies in execution. However, the same PCB and sample preparation was used in both cases and will be described first.

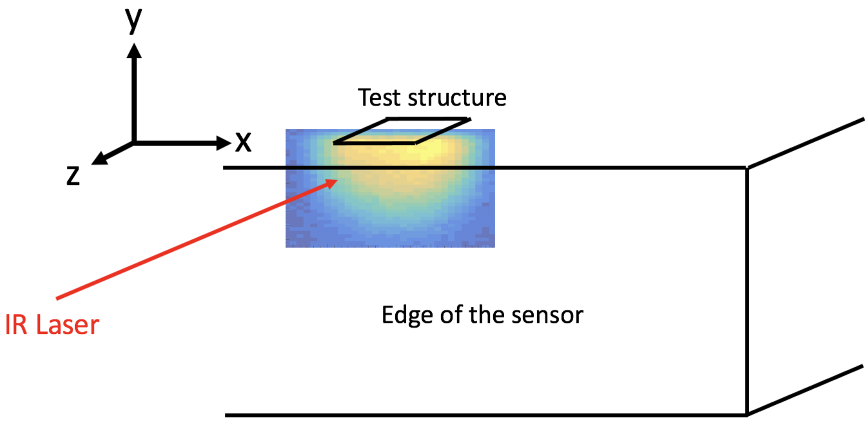

Figure 5.4.2: Visualisation of a eTCT scan over the surface of the detector. Not to scale.

5.4.1 Sample preparation

To be able to measure chips with using eTCT, they have to be mounted on a custom PCB. The PCB features 8 spots for SMA connectors, with shared ground on a fully metallised back plane. One connection spot is for the large central metal plane, which is where the samples were placed in this study, as can be seen in figure 5.4.3 below. 6 connections are used for the readout, and the last SMA connector spot, also featuring a spot for a surface mounted pin connection, is intended for readout of temperature sensors. Ground for this connector spot is isolated from the other grounds, as a previous iteration of the PCB design showed that the temperature measurements of Pt-1000 sensors became skewed when connected to common ground. The samples are connected to the PCBs using a silver based conductive adhesive[8]. All the connections between the PCB and the chip are done through wire bonding. The specific bond pads used for each chip is found in chapter 4. While a few samples were wire bonded by the CERN Wire Bonding Lab, the majority of samples were prepared at Lancaster University. Initial samples were bonded using a Kulicke & Soffa 4123 to perform aluminium wedge bonding. A TBT HB100 automatic wire bonder was acquired and used for all but the initial samples. While the CCPDv3 set were wire bonded using aluminium wedge bonding, the RD50-MPW1 and-MPW2 sets were wire bonded using gold ball bonding. This was only due to logistical circumstances, and is not expected to have any impact on the connectivity of the samples. Commonly gold bonding is done at elevated temperatures, around 120 °C, however, all bonds were done at room temperature in order to minimise the effects of annealing on the irradiated samples. The PCB are manufactured using Rogers RO4350B laminate ceramic material with good thermal conductivity in order to maximise effect of DUT cooling during measurements. The surface finish is ENEPIG[9]. All PCBs have a Pt-1000 attached with glue in order to monitor the temperature as close to the sample as possible. Later PCBs used a surface mounted pin connector to read out the Pt-1000, instead of the SMA connector as seen in figure 5.4.3, however, this should cause no difference in temperature measurements.

5.4.2 Particulars TCT at Lancaster University

The Physics Department at Lancaster University hosts a commercial TCT system produced by Particulars[10]. The setup contains the fundamental parts necessary for TCT measurements, and can be modified to allow for each of the illumination techniques described above. It comes with either a red or IR picosecond laser, which is achieved by a driving a laser diode with short high voltage pulses. Both the pulse length and pulse

---

[8] Early samples were connected using Letisilber 200. Later samples used Electrolube Conductive Adhesive from RS Components.

[9] Electroless Nickel Electroless Palladium Immersion Gold

[10] Company details at: `http://particulars.si`

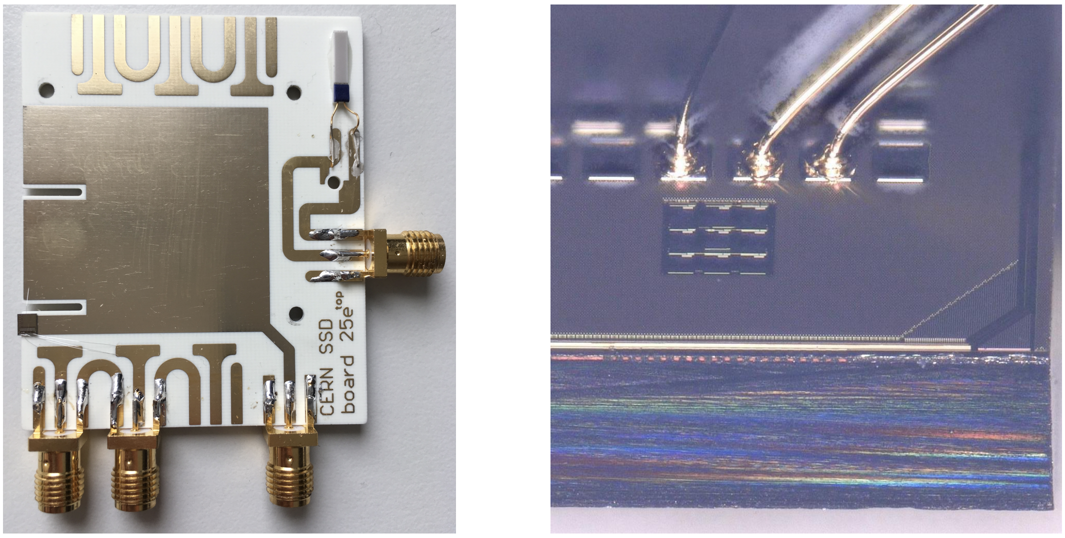

Figure 5.4.3: Left image shows the PCB used during eTCT measurements. In this image a CCPDv3 is glued and bonded to the PCB. The right image shows the bond scheme of the RD50-MPW2, 3 μm structure using gold ball bonds.

repetition rate can be set by the accompanying software, with pulse length ranging from below 350 ps to 4000 ps and repetition rate between 50 Hz - 500 kHz. The pulse length is set by setting a percentage in the software to a DAC in the laser driver. The scale is reversed, such that 100% in the software represents just above the threshold for lasing, i.e. the shortest possible pulse, and 0% is maximum. All measurements done with this setup was at 98%, which should equal a pulse in the 350 - 400 ps range, with a repetition rate of 100 Hz. The low repetition rate is to ensure that the DUT[11] returns to equilibrium between each laser pulse. The laser diode is coupled directly to a single mode optical fiber which is in turn coupled to the focusing optics achieving beam spots around 10 μm, further detailed below. As is common in most TCT setups, three motorised translation stages are used to allow for scan measurements in 3D. The translation stages in Particulars' TCT setup are provided by STANDA and have a resolution of 1 μm[12]. The focusing optics is mounted on one of these translation stages, and the sample holder is mounted on the remaining two stages. The three stages are orthogonally oriented to each other to achieve 3D movement. See figure 5.4.5 for the exact positioning of the stages. It should be noted that the STANDA stages delivered with this iteration of the setup experienced a slight wiggle back and forth during movement, with more details on this below. According to STANDA this has been fixed [87].

The setup also contains a bias tee and an amplifier. The bias tee is a three port com-

---

[11] Device Under Test

[12] A full step of the stage is 1 μm, but 1/8 steps, 0.156μm, is achievable with specialised controllers. The setup used in this study is limited to full steps.

Figure 5.4.4: The TCT setup at Lancaster University. Right to left: Metal case housing the DUT (seen below in figure 5.4.5), bias source Keithley 2410, Tektronix TDS 7254 DPO oscilloscope, and the computer used for the data acquisition.

ponent used to separate the DC voltage bias and the fast signal that is delivered to the sample, and is rated up to 1000V. The amplifier, built by Particulars, has a gain of 55 dB with a bandwidth of 0 - 2GHz. High amplification is important so that the laser signal can be kept at a low energy. Injecting a large number of e^-/h^+ pairs locally can cause plasma effects and alter the local electric field, distorting the signal [108]. A DC filter is connected on the DC port of the bias tee. As visible in in figure 5.4.5 the DUT is encapsulated within a metal box, while not a perfect Faraday cage, it helps to block light and some RF noise and also acts as the rigid body the translation stages are attached to.

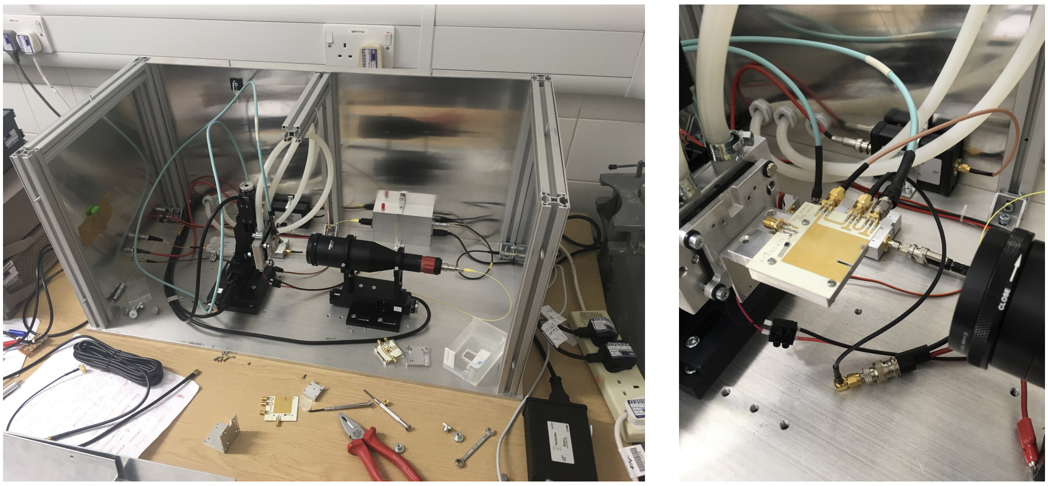

Figure 5.4.5: View of layout inside the metal box. Focusing optics mounted on a translation stage, and DUT mounted on two orthogonally positioned stages. On the right, the heat sink with two connected tubes for coolant circling and Peltier element is visible behind the DUT.

The above-mentioned PCB used in all the measurements was originally designed for the sample holder on the EP-DT-DD:SSD group's TCT setup at CERN. A custom made L-piece and additional metal block was made to fit this PCB to Particulars original sample holder plate, which is a bare metal plate with M2 and M2.5 screw holes in a square pattern. This metal plate is mounted on two translational stages.

Between the translation stages and the sample holder plate, a heat sink and a Peltier element is sandwiched. The heat sink is a metal block with a channel with two hose connectors that can be flushed with water or coolant. A Grant LTD6 chiller, capable of going down to -20 °C filled with a mixture of 40% ethylene glycol and water was used to cool the heat sink. The Peltier was connected to a current source capable of going up to 10A. A Keitley 2000 multimeter was used to read out the temperature from the Pt-1000. Cooling was done down to around 0 °C, and to avoid condensation or frost, the box was constantly flushed with dry air. The laboratory is equipped with compressed air line, and a series of SMC[13] particle and membrane filters was used to filter and dry the air prior to flushing the box.

A Keithley 2410 was used for biasing the detector. The signal capture for the initial measurements was done on a Tektronix TDS 7254 Digital Phosphorous Oscilloscope. The scope features a bandwidth of 2.5 GHz and 20 GSa/s sampling rate. The large bandwidth and high sampling rate is important when the waveforms are to be analysed due to the fast signals, normally below 5 ns in length. The oscilloscope is triggered using a reference signal fed from the laser driver. During the measurements of the last two sample sets the Tektronix oscilloscope broke down. No oscilloscope of similar performance was available and it was replaced with a DRS4 Evaluation Board. The DRS4 is a switched capacitor array ASIC capable of digitising up to eight channels with a 700 MHz bandwidth, and a 5 GS/s sampling rate at 1024 sampling points[14]. The reduction in performance is visible in a slight smoothing of the waveforms, however, when evaluating the relative amount of collected charge the impact should be limited. It will be noted which instrument is used when presenting the corresponding result.

Particulars provide a LabVIEW-based readout software for automatising and storing the measurements done with this TCT setup. The software contains drivers for many common types of oscilloscopes and voltage sources. Measured signals are recorded in a

---

[13] Modular filters used in this setup can be found at: `http://www.smcworld.com/products/en/s.do?ca_id=499`

[14] Details on the DRS4 can be found at: `https://www.psi.ch/en/drs/documentation`

binary format, and an analysis software built around the ROOT libraries are used to read the data files. While this software also contains some analysis features, a different software was used and extended in this work, and will be explained below.

Beam spot

Measuring with a minimal beam spot is important to get a good estimation of the depletion depth, when the depletion depth is on the same order as the size beam spot, which is the case for the non-irradiated low resistivity samples used in this study. The laser beam waist can be measured using the knife edge technique. Originally this is done by first measuring the intensity of the laser and then the subsequent intensity after introducing a knife edge into the beam line at different positions. Instead of using a knife's edge, a sensor with depletion region width, $\omega \gg \omega_{beam}$, is used where the laser is scanned from outside the sensor, over the edge into the depletion region. Assuming a Gaussian beam, the total power can be expressed as:

$$P_{tot}(x,y) = I_0 \int \int_{-\infty}^{\infty} \exp\left(-2\left(\frac{x^2}{\omega_x^2} + \frac{y^2}{\omega_y^2}\right)\right) dxdy = \frac{\pi}{2} I_0 \omega_x \omega_y \tag{5.4.1}$$

Considering the laser beam moving along the x-axis partially outside of the sensor the partial absorbed laser power can be expressed like:

$$P_{edge} = \frac{P_{tot}}{2} - \sqrt{\frac{\pi}{2}} I_0 \omega_y \int_{-\infty}^{x_{edge}} \exp\left(-\frac{2x^2}{\omega_x^2}\right) dx \tag{5.4.2}$$

Here x_{edge} is the position of the edge. Further simplifying this, and by substituting with the Error Function the power function finally is finally expressed as:

$$P_{edge} = \frac{P_{tot}}{2}\left[1 - \text{erf}\left(\frac{\sqrt{2}(x_{edge} - x)}{\omega_x}\right)\right] \tag{5.4.3}$$

Here ω_x is the $1/e^2$ width. Each measurement is fitted with equation 5.4.3, using P_{tot}, x, and ω_x as fitting parameters. The beam width used in the analysis in this study is the FWHM[15], and in the case of a Gaussian distribution the FWHM is related to the $1/e^2$ width such that:

$$2\omega_x = \frac{\sqrt{2}\text{FWHM}}{\sqrt{\ln 2}} \approx 1.699 \times \text{FWHM} \tag{5.4.4}$$

---

[15] Full Width Half Maximum

Using a fully depleted simple diode, with 300 μm thickness, multiple edge scans are done at different z values as seen in figure 5.4.7 between the sensor and the focusing optics to determine the minimum beam width. In a Gaussian beam following focusing optics the FWHM at any given point along the beam axis can be expressed as following.

$$\text{FWHM}(z) = \text{FWHM}_0 \sqrt{1 + \left(\frac{z - z_0}{z_R}\right)^2} \tag{5.4.5}$$

Where FWHM_0 is the FWHM value at the beam waist, z_0 the z-coordinate of the beam waist, and z_R is the Rayleigh length. The Rayleigh length denotes the length from the beam waist to the position at where the cross sectional area of the beam has doubled. Equation 5.4.5 is fitted to the extracted FWHM values to estimate the beam waist. As is revealed in figure 5.4.6 the FWHM of the laser beam waist in this TCT setup is approximately 12.5 μm, and has a Rayleigh length of 325 μm.

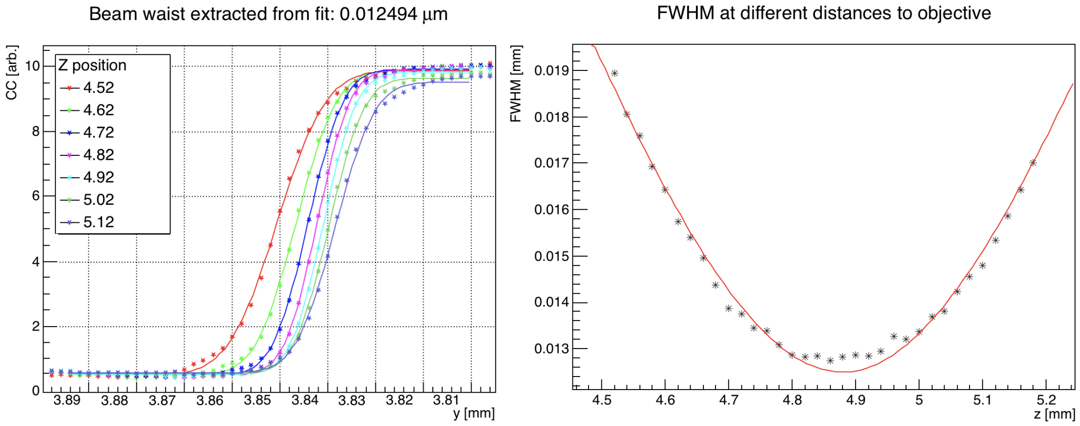

Figure 5.4.6: Left graph visualises every fifth measurement done along the z axis. Signal is inverted to have positive values. Beam waist is extracted from fitting equation 5.4.5 to the measured FWHMs, as can be seen in the graph on the right.

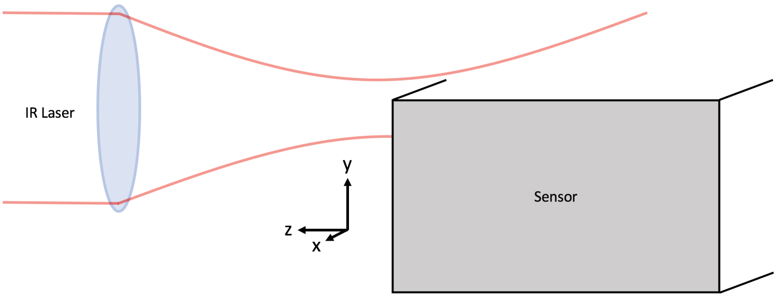

Figure 5.4.7: Visual of knife scan done with a sensor. z is the direction along the beam axis, and measurements are done starting outside the sensor, moving in negative y axis down into the the sensor creating the pattern seen on the left in figure 5.4.6.

5.4.3 TCT+ at SSD lab in CERN

The EP-DT-DD SSD group at CERN has a custom built TCT setup, nicknamed TCT+. Similarly to the Particulars TCT it features automatic 3D scanning during measurements. However, instead of having to change the sample holder depending on whether top, bottom, or eTCT is desired, the TCT+ setup has a constant sample holder and instead features 5 different optics to where the sample can be moved. As can be seen in figure 5.4.8 two focusing lenses above, and two below the sample holder are coupled to a red and IR laser source, respectively, for top and bottom illumination, and a fifth lens is stationed to the side coupled to an IR laser source for edge illumination. The movement in the horizontal plane is achieved with a Newport UTS 100CC orthogonally positioned atop a Newport UTS 150CC stage. The 100CC and 150CC stages has a travel range of 10 cm and 15 cm respectively. While the minimum incremental movement is 0.3 μm for, the the bi-directional repeatability is guaranteed at 1.75 μm so the movement is limited to 2 μm increments in with the TCT+ software. The z-movement is accomplished using a Newport LTA-HS stage, having a travel range of 5 cm and moves with 2 μm increments. All stages are controlled using a Newport ESP301-3N stage controller. In contrast to the Particulars setup, all lenses are fixed and the sample holder, made out of copper, is attached to the three stages in this setup. The DUT, stages and lenses are housed inside a ETS-Lindgren 5230ES Faraday cage, designed to block external RF signals in the 1 MHz - 5 GHz range.

The laser system uses two laser heads, one with red laser light, 660 nm, and one for IR laser light, 1064 nm. The laser heads are driven with using a PicoQuant PDL 828 "Sepia II" laser driver with two separate channels used for the laser heads. The timing of the pulses is controlled using an Agilent 8110A pulse generator connected to the laser driver. Both lasers emit 200 ps pulses at a 200 Hz pulse rate. Using fused fiber optic splitters, the laser light is split such that 10% goes to a reference diode monitoring the laser intensity, and the remaining 90% is split between the lenses. In case of the red laser the laser is split equally between the two lenses, however, the IR laser light is split such that the eTCT lens get 45% of total emitted light and the top and bottom lens get 22.5% each.

Similarly to the Particulars setup, the TCT+ also features a Peltier element attached to the sample holder with a heat sink attached to the opposite side on the Peltier element. The heat sink is cooled with a Huber CC-505 chiller using a glycol ethylene and water mixture. Whereas the cooling setup in Lancaster is manually operated, the TCT+ setup uses a LairdTech PR-59 PID controller in conjuncture with the TCT+ software for automatic temperature control. The Faraday cage is flushed with dry air.

Bias voltage is applied using a Keithly 2410. The TCT+ uses a cividec C2-HV, which is integrates both a fast amplifier and bias tee into on component. It has a bandwidth of 1 MHz - 2 GHz and an amplification gain of 40 dB. The signal is captured with an Agilent DSO9254A oscilloscope, which has a bandwidth of 2.5 GHz and a maximum sample rate of 20 GSa/s.

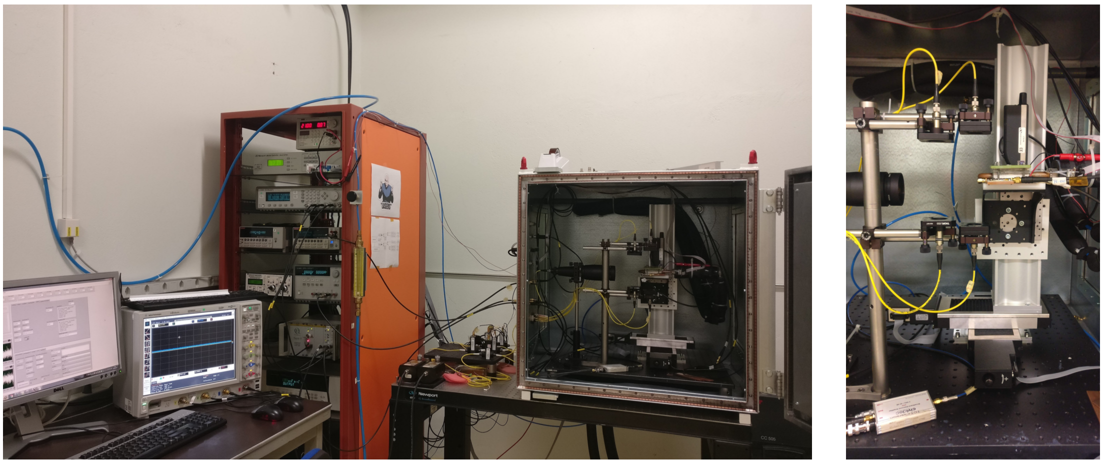

Figure 5.4.8: The EP-DT-DD SSD group's TCT+ setup at CERN. Detailed view of stages and optics setup to the right. Pictures adapted from [82].

Beam spot

Following the same procedure as described in the beam spot part under section 5.4.2 above, knife edges scans were done using a 300 μm thick fully depleted simple diode sensor. The measurement was done in conjuncture with calibrating the iris of the eTCT focusing optics, and the measurement presented in figure 5.4.9 is the final measurement during this calibration. The beam waist has a FWHM of 10.9 μm, with a Rayleigh length of 221 μm. The TCT+ setup has a slightly superior beam waist compared to the setup at Lancaster University. This could be due to better coupling in the optical setup.

5.5 Measurements and analysis

The collected data is processed using a C++ analysis library, called TRICS, developed by Marcos Fernandez Garcia for the data collected with the TCT+ setup. The software

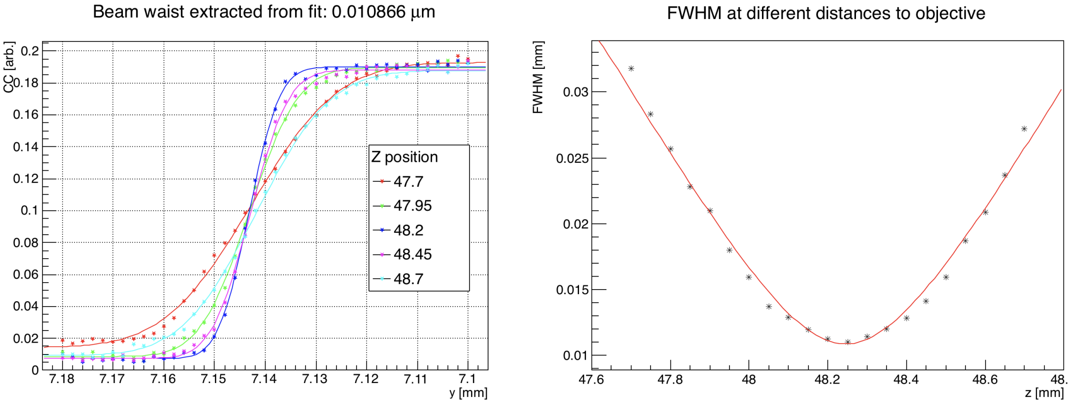

Figure 5.4.9: Knife edge scan results during calibration of the TCT+ eTCT focusing optics. Beam waist is extracted from fitting equation 5.4.5 of the extracted FWHMs, as can be seen in the graph on the right.

takes data in ascii format and converts it into a ROOT file, containing a TTree with the waveform data, and all setup parameters for that measurement. In order to use the eTCT data collected with the Lancaster University setup, a conversion script was written. While the Particulars setup comes with its own suite of analysis software, analysis scripts had already been written with the other library. Using the Particulars TCTAnalyse library, the data was extracted from the binary files produced by the Particulars setup and converted into the text format required by the TCT+ analysis software.

5.5.1 Charge collection

Following eq. 2.3.2, by integrating the measured signal the collected charge can be calculated. However, as no calibration is done with the laser signal, the exact amount of injected charge is unknown. This is of no concern as the relative change in charge collection with irradiation is what is sought. The collected charge is calculated by integrating the induced current signal:

$$CC = \int_{t_{left}}^{t_{right}} i(t)dt \tag{5.5.1}$$

t_{left} is a value calculated individually for each waveform, determined when the values reaches above half of the signal maximum, after taking the baseline into account. The average t_{left} of all waveforms in one file is taken as the final value, as some t_{left} are wrongly calculated due to the signal being on the same magnitude as the baseline. t_{right} is fixed to $t_{left} + 8$ ns, unless the integration time is specifically stated in the plot. As we are interested in the charge generated inside the active region, 8 ns was determined to be a appropriate value, with drift signals being collected within 5 ns and most of the diffusion generated signal taking a few tens of ns. In addition, signal reflections due to impedance mismatch in the bias-T arrive 20 ns from the first pulse and thus will also be excluded in the calculations. Before the integration of the signal is done, the current baseline is subtracted from the signal. The baseline is calculated by averaging data points in the time region before the signal. In addition, CC in the samples measured with the TCT+ system is divided by the measured laser power, to remove any fluctuations due to the laser. This was however not possible with the Lancaster system lacking a reference diode, but the fluctuations are small under normal working conditions. dt is the time resolution during measurement.

5.5.2 1D and 2D scans

The majority of eTCT measurements performed are either 2D or 1D charge collection scans. The 2D scans serve two purposes. Firstly, it used to verify relative uniformity of field and to give a qualitative overview of the depletion region in over the edge surface. Secondly, to ensure the 1D scans are consistently done over the center of the diode. A visualisation of the 1D scan compared to the 2D surface scan is seen below in figure 5.5.1.

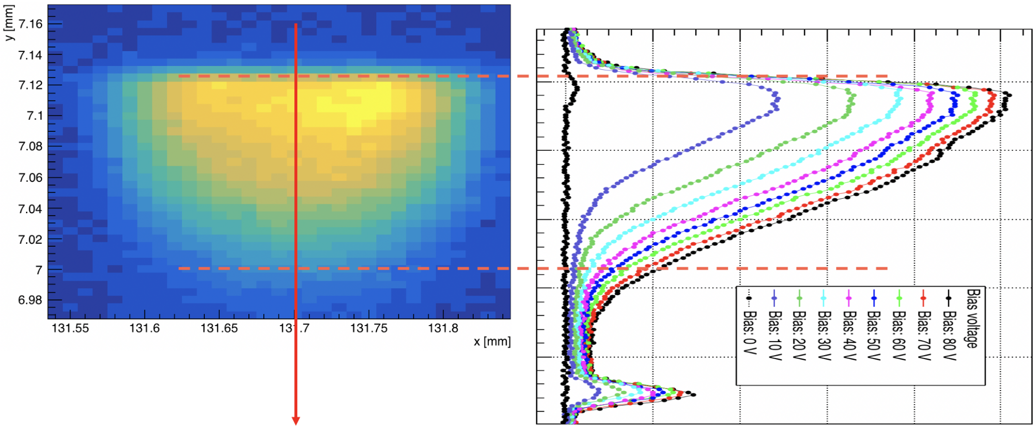

Figure 5.5.1: Visualisation of how a 1D charge collection scan is performed. The measurements here are from the CCPDv3_LA6 sample and can be found in section 6.4.2 and 6.4.3

Ultimately, the charge collection is calculated from the signal and section 6.3 presents the raw waveforms at different locations inside the detector. With first waveform always taken at maximum charge collection, and then at increasing depths into the detector from this position, as can be seen as an example in figure 5.5.2.

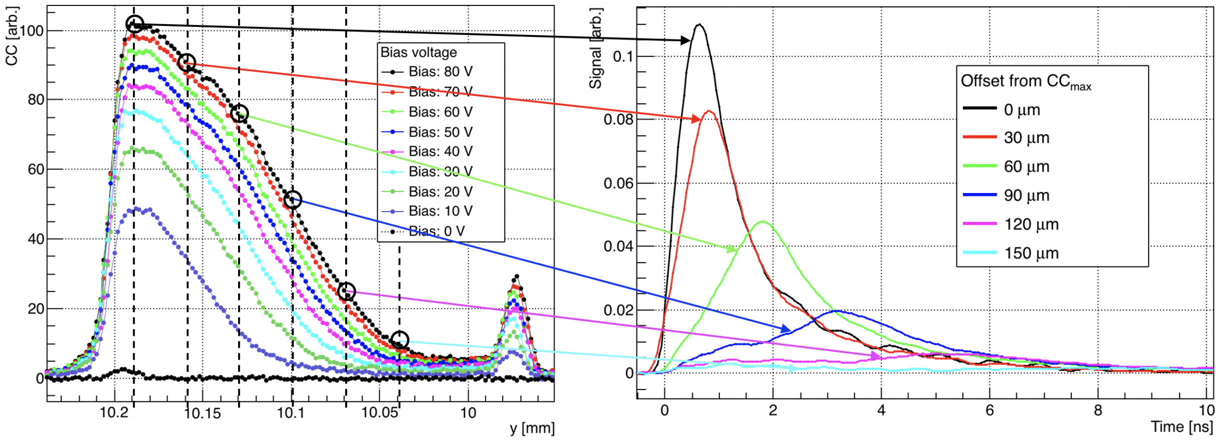

Figure 5.5.2: Waveforms measured at different positions inside the detector. Example measurements using the CCPDv3_LA6 sample.

1D scans are used extensively to estimate change in integrated charge collection, depletion width and effective doping concentration. All 1D scans are done starting outside the detector, then either scanning through the hole bulk or stopping when no signal can be measured any more. All scans are recorded using 256 averages on the oscilloscope. Prior to each 1D scan, in addition to the surface scan to locate the center, a focus scan is done to find the optimum for the beam spot. This is especially important for samples with small depletion regions as can be seen in the next section.

5.5.3 Deconvolution of depletion depth

Using the 1D charge collection plot described above, the width is extracted by calculating the FWHM. The FWHM is calculated by taking the positional values of the half maximum point on the two lines crossing the two measurement points that are directly above and below the half maximum on each side of the maximum. This is illustrated in figure 5.5.3 below. Initially a Gaussian distribution was fitted to the data in order to extract the FWHM, however, the irregular shape of some of the irradiated sensors prevented this method to be used, and instead the current method was selected for highest consistency.

From the FWHM, the N_{eff} can be calculated in a couple of ways. Firstly, it is possible to calculate the N_{eff} straight from the inverse eq. 3.4.10, however, this method relies only on one data point and also gives skewed values for non-irradiated sensors which have a comparatively large FWHM at 0 bias, due to the deep n-well implant. A superior method, more commonly used, is through fitting eq. 3.4.10 to the FWHM as a function

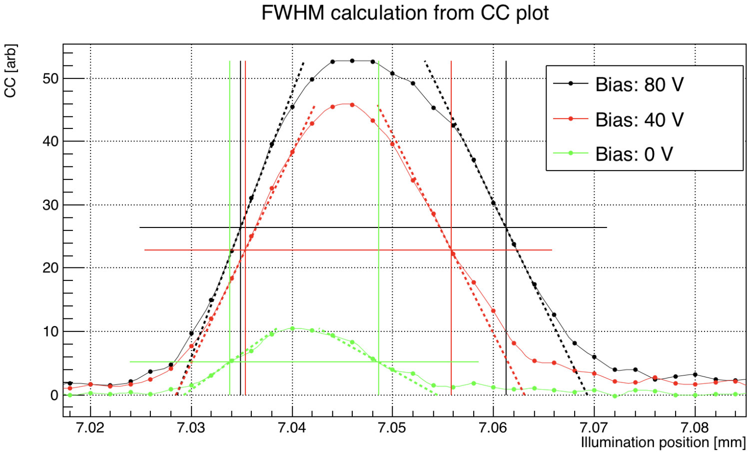

Figure 5.5.3: Example of FWHM calculated from CC profile in an non-irradiated CCPDv3. Horizontal lines represent half maximum value, and the width is the distance between the two vertical lines.

of bias voltage. This is done after scanning the depletion depth at different voltages, extracting the FWHM at each voltage and fitting the following equation, based on eq. 3.4.10:

$$\text{FWHM}(x) = [\boldsymbol{p_1}] + \sqrt{\frac{2\epsilon_{Si}\epsilon_0}{q[\boldsymbol{p_2}]}x} \tag{5.5.2}$$

$[\boldsymbol{p_1}]$ and $[\boldsymbol{p_1}]$ are fitting parameters, where $[\boldsymbol{p_1}]$ is including FWHM contribution from V_{bi} and the deep n-well implant. $[\boldsymbol{p_2}]$ is the fitting parameter corresponding to the $\mathrm{N_{eff}}$. This method has been shown to yield $\mathrm{N_{eff}}$ values close to the specified value in non-irradiated high resistivity HV-CMOS sensors [74]. An important difference between those samples, and the sensors used in this study is the magnitude of the FWHM. The high-resistivity sensor have a FWHM noticeably larger than the laser beam waist, giving good agreement between FWHM and real depletion width. In the case of standard-resistivity sensors, i.e. 10 - 20 Ωcm, the depletion depth below 100V bias is limited to the 10 - 20 μm range, which is relatively close to the beam width used to measure it. With the measured FWHM being a convolution of the actual depletion volume and the laser beam profile, the magnitude of the depletion depth will get overestimated if approximated to the FWHM when the depletion depth is close to, or smaller than the laser beam width. This is illustrated in the plot below, which shows the convolution of the ideal depletion region, a box function, and the laser beam, a Gaussian function.

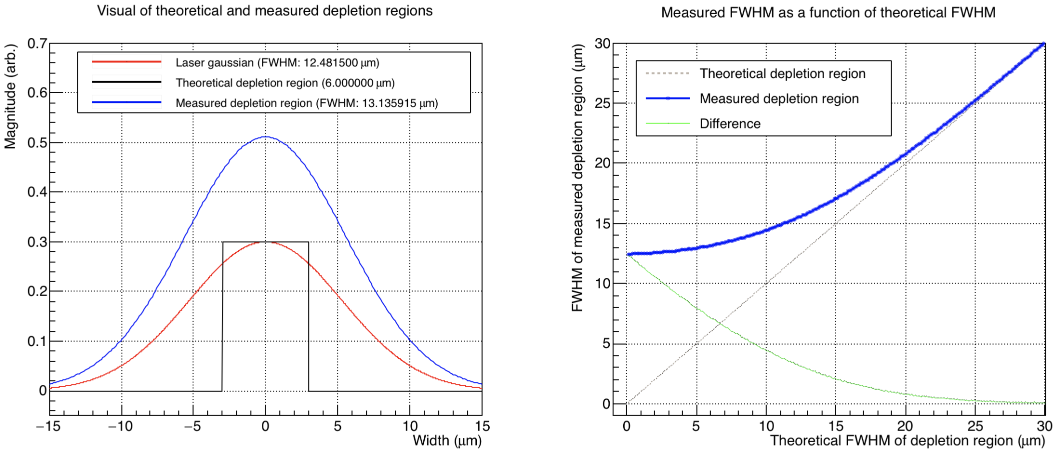

Figure 5.5.4: Left: Convolution of TCT laser beam width and ideal 2D depletion region. Right: Difference between ideal 2D depletion region FWHM and measured FWHm for FWHMs up to 20 μm. Laser width corresponds to the Lancaster University TCT setup.

Figure 5.5.4 clearly shows how measured FWHMs below 30 μm get overestimated, with an increasing overestimation as the FWHM approaches 0 μm. In order to possibly achieve a more accurate value of the actual FWHM, the measured FWHM has to be subtracted with the a simulated difference for the corresponding beam width. This method was first presented in [31], which compared the N_{eff} fitting method of unaltered FWHMs to calculating the N_{eff} from one data point that had been compensated with the convolution difference. It was shown that the calculation method with the convolution compensation gave a better approximation for the non-irradiated sample when comparing to nominal resistivity given by the foundry, and overall gave a lower N_{eff} than the fit method.

To use the good approximation for small FWHM while still using a as much data as possible, an analysis method combining these two methods will be explored in this study. The calculated FWHM will be compensated with the convolution difference at each voltage and subsequently eq. 5.5.2 will be fit to this corrected data.

Further, the fit used is limited to FWHM cases that are lower than 70% of the width of the test structure. When the test structure is lacking a guard ring and the depletion depth approaches the test structure width the depletion region will partly start to grow sideways and the growth perpendicular to the junction will deviate from eq. 3.4.10.

5.6 SIMS

When studying the acceptor removal effect and the thermal donor introduction rate knowing the initial doping concentration, as well as the contraction of oxygen and carbon defects is advisable. Secondary-ion mass spectrometry, SIMS for short, is an effective technique that analysis the composition of a solid material. The surface of the sample solid is sputtered with ions, and the mass/charge rate of ions knocked out from the solid are analysed to determine the element. The SIMS measurement was requested and done at ITE, using their CAMECA IMS 6F SIMS device. The instrument uses a primary ion beam, and continuous sputtering SIMS was used to achieve a depth profile for B, C and O.

Chapter 6

Characterisation of irradiated low resistivity HV-CMOS prototypes

This section is dedicated to presenting and discussing the measurements done on irradiated HV-CMOS prototypes, whether or not it could be a potential post-processing method for improving the operations of low resistivity HV-CMOS, but also the general effects of hadron irradiation on such sensors. In total, three sets of different low resistivity HV-CMOS prototypes were sent to three different irradiation centers for hadron irradiation. These sensors were characterised mainly through eTCT area scans and one dimensional scans to probe the depletion region and electric field of the devices. From this, charge collection efficiency and total charge collection is estimated to evaluate performance after irradiation.

The first set of samples studied is a batch of 20 Ωcm CCPDv3 chips, developed in collaboration with the CLIC community. Details on the chip can be found in section 4.1.1. 2 sets of 9 samples each were sent to Los Alamos National Laboratory for irradiation at LANSCE. The samples were irradiated with 800 MeV protons up to $1.28 \times 10^{16} n_{eq}/cm^2$ fluence[1]. The irradiations were done at room temperature, but stored at approximately -20 °C post-irradiation. Shipment from the irradiation facility to Lancaster University was done using a cold box. The two samples for the two highest fluence requests, $3.5 \times 10^{15} n_{eq}/cm^2$ and $6 \times 10^{15} n_{eq}/cm^2$, turned out to have received an insufficient dose

---

[1] LANSCE proton beam have a hardness factor of approximately 0.75

during the initial run. These two samples were kept for a second irradiation, and accidentally received a significantly larger dose than requested. Additionally, these two samples were kept overnight at room temperature in the irradiation facility prior to collection, which has to be taken into account for annealing effects. Fluences and initial annealing states are listed below. After reception of the samples at Lancaster University all samples were exposed to approximately 12.5 h at RT. Part of the time was during sample preparation, but the majority of the 12.5 hours are due to shipment between Lancaster University and CERN. This additional time is included in the time listed in table 6.0.1.

Sample	Fluence ±11% [n_{eq}/cm^2]	Initial time at RT [min]
CCPDv3_LA1	2.08×10^{13}	805
CCPDv3_LA2	6.83×10^{13}	850
CCPDv3_LA3	1.27×10^{14}	915
CCPDv3_LA4	3.22×10^{14}	1057
CCPDv3_LA5	7.96×10^{14}	1285
CCPDv3_LA6	1.22×10^{15}	1525
CCPDv3_LA7	2.09×10^{15}	1880
CCPDv3_LA8	$(2.04 \times 10^{15} + 3.7 \times 10^{15})$ 5.74×10^{15}	6235
CCPDv3_LA9	$(1.81 \times 10^{15} + 1.1 \times 10^{16})$ 1.28×10^{16}	6205

Table 6.0.1: List of CCPDv3 samples irradiated with 800 MeV protons at LANSCE. The fluence uncertainty is 11%.

The second set of samples acquired were a 10 Ωcm bulk resistivity version of the RD50-MPW1 chip produced by LFoundry. Details on the chip can be found in section 4.2.1. These chips were sent to the Bern Cyclotron Proton Irradiation Facility for irradiation with 18 MeV protons. While fluence up to $2 \times 10^{15} n_{eq}/cm^2$ was initially requested[2], the 2020 Covid-19 pandemic interrupted operations and ultimately the two highest fluences were left out of the study. With the irradiation facility in Bern having a flat beam within 2 × 2 cm^2, the RD50-MPW1 samples, being approximately 5 × 5 mm^2 are expected to have been irradiated homogeneously. The irradiation was carried out at room temperature, however, the time to reach the highest fluence is less than an 30 minutes of irradiation meaning the largest contribution of RT exposure can be attributed to sample preparation. With the low total time at room temperature, the annealing state of all the samples can be assumed to be similar.

---

[2] The hardness factor at this facility is 3.49 [30].

Sample	Fluence ±10% $[n_{eq}/cm^2]$	Initial time at RT [min]
MPW1_Bern1	1.02×10^{13} $(1MRad)$	41
MPW1_Bern2	2.04×10^{13} $(2MRad)$	35
MPW1_Bern3	5.1×10^{13} $(5MRad)$	132
MPW1_Bern4	1.02×10^{14} $(10MRad)$	156
MPW1_Bern5	2.04×10^{14} $(20MRad)$	58
MPW1_Bern6	5.1×10^{14} $(50MRad)$	120

Table 6.0.2: List of RD50-MPW1 samples irradiated with 18 MeV protons at Bern Proton Irradiation Facility. The fluence was calculated from the dosage, in parenthesis, which was given by the operators.

The third and last set of samples were 10 Ωcm RD50-MPW2. The low resistivity RD50-MPW2 were produced on two different wafers, and the measurements in this study are done on chips from wafer 24. The samples were irradiated in the TRIGA Mk II reactor, within the RD50 framework. Time frame of irradiations is similar to the Bern proton irradiation facility, with the highest fluence being on the hour time scale. The initial time at RT values in list 6.0.3 also include time to glue and wire bond the samples. While the different test structures on the chip have separate readout pads, technical difficulties with the wire bonder forced different chips to be used for reading out the different test structures. As such, all samples presented in table 6.0.3 are different chips, even though both the 3 μm and 8 μm structure exists on each chip. The only exception to this are the MPW2_W24_3um4 and the MPW2_W24_8um4, where the 3 μm structure was first measured, to then have new wire bonds made to the 8 μm structure and measured again. Only the 8 μm structure with rounded corners was measured in this study.

Sample	Fluence ±10% $[n_{eq}/cm^2]$	Initial time at RT [min]
MPW2_W24_3um1	1×10^{13}	167
MPW2_W24_3um2	3×10^{13}	112
MPW2_W24_3um3	1×10^{14}	106
MPW2_W24_3um4	2×10^{14}	121
MPW2_W24_3um5	5×10^{14}	129
MPW2_W24_3um6	1×10^{15}	120
MPW2_W24_3um7	2×10^{15}	146
MPW2_W24_8um2	3×10^{13}	783
MPW2_W24_8um4	2×10^{14}	167
MPW2_W24_8um7	2×10^{15}	147

Table 6.0.3: List of RD50-MPW2 samples irradiated at the TRIGA II reactor at JSI. Uncertainty in fluence is 10%.

Annealed CCPDv3 sample set

After initial measurements, an isothermal annealing study was carried out on the CCPDv3 sample set. While planned annealing studies were planned for the MPW1 and MPW2 sets, logistics and time constraint prohibited this to be carried out, but is recommended for a future study. Due to the large initial difference of exposure to room temperature, all samples apart from the CCPDv3_LA8 and CCPDv3_LA9 were brought to similar annealing states using a climate chamber. The chamber was set to 22 °C and each sample was removed individually once it had reached 6230 minutes at this temperature. In moderately irradiated pad detectors, the end of beneficial annealing was reached around 80 minutes at 60 $\circ$C, and thus 60 $\circ$C is commonly a used when annealing irradiated detectors[44]. In order to approximate the equivalent of 6230 minutes at room temperature to the numbers of minutes at 60 $\circ$C annealing, eq. 3.5.1 is used. 6230 minutes at 22 $\circ$C yields approximately the same α value as 28 minutes at 60 $\circ$C. However, it should be pointed out that as there are different mechanisms to how defects contribute to leakage current and the effective doping concentration, equivalent time in terms of beneficial annealing is slightly different. At 60 $\circ$C the beneficial annealing process happens approximately 130 faster compared to 22 $\circ$C, and roughly equates 48 minutes. On the other, reverse annealing have shown much larger acceleration in process at elevated, and the 28 minutes calculated using eq. 3.5.1 is seen as a good middle ground. In reality one should keep in mind the actual annealing history of the samples are 6230 minutes at room temperature in with the additional time at 60 $\circ$C. Once the samples had reached 6230 minutes at 22 $\circ$C, all samples were annealed at 60 degrees for 52 minutes to bring the total annealing at 60 °C to 80 minutes. After this, individual isothermal annealing was carried out on the two samples CCPDv3_LA6 and CCPDv3_LA9. They were exposed to 60 °C at exponentially increasing time intervals. Please refer to the table 6.0.4 for exact times at this temperature. eTCT measurements were done between each annealing step.

CCPDv3_LA6	CCPDv3_LA9
177 min	178 min
376 min	376 min
691 min	756 min
1378 min	1163 min
3343 min	2187 min
7145 min	3714 min
16989 min	
28948 min	
69214 min	

Table 6.0.4: Isothermal annealing steps for the CCPDv3_LA6 and CCPDv3_LA9. Annealing was done at 60 °C.

6.1 Leakage current measurements

Presented here is the current of the irradiated sensors measured during the eTCT scans. While not giving accurate values of the actual leakage current, it gives a qualitative view of the relative behaviour of the leakage current. The measurements for the CCPDv3 samples were done at -15±0.5 °C, while both the RD50-MPW1 and RD50-MPW2 samples sets were measured at 2±1.5 °C.The discrepancy in measurement temperature is due to the limited cooling power of the Lancaster University setup. The uncertainty in I_{leak} purely from a temperature fluctuations during measurement is expected to be around $\pm 0.05 I_{leak}$ for the CCPDv3 samples, and $\pm 0.14 I_{leak}$ for the RD50-MPW1 and RD50-MPW2 sets, assuming only bulk generation. The CCPDv3 samples were biased through the Sub pad, with GND connections connected to ground. No guard ring surrounds the passive structure. The measured leakage current at voltages below breakdown voltage is as expected low in the non-irradiated CCPDv3, saturating around 1.2 nA as can be seen in figure 6.1.1. The initial increase between the measurement points of the non-irradiated CCPDv3 is due to measurement resolution of the Keithley 2410 when applying a voltage higher than 21V. While not affecting the irradiated samples, due to their higher leakage current, the actual leakage current of the non-irradiated sample is smaller than the measured value. While not included in figure 6.1.1, the breakdown voltage of the CCPDv3 chip was found to be at 93V, slightly higher than simulations during chip design [17].

Similarly, the non-irradiated RD50-MPW2 samples have a leakage current lower than the resolution of the measuring instrument. However, an important point to consider is that the RD50-MPW2 has all 9 passive diodes shorted together and thus has a larger depleted volume and junction area, 150 × 150 μm^2 and 180× 180 μm^2 for the 3 μm and 8 μm structure respectively. Both structures showed a leakage current lower than 1 nA. The breakdown voltage for the RD50-MPW2 was found to be 56 V for the 3 μm structure and 121 V for the 8 μm structure with rounded corners, consistent with measurements done by other groups [25].

Regarding the irradiated samples, a gradual increase of the leakage current following increasing fluence is seen in both the CCPDv3 and RD50-MPW2 samples as is expected due to increased generation of minority carriers by the defects introduced by irradiation. The leakage current in the CCPDv3 set appears to stop increasing beyond $2 \cdot 10^{15} n_{eq}/cm^2$. However, this can be attributed to the fact that the leakage current in irradiated sensors increases due to carrier generation in the depleted region. Beyond $2 \cdot 10^{15} n_{eq}/cm^2$ there is a decrease in active region as is seen in the eTCT measurements below. So a combination of increased generation with a decreasing active volume gives the appearance of a none-increasing leakage current. Figure 6.1.2 shows the normalised leakage current to an approximate depleted volume as a function of fluence. While the increase follows the same general trend as literature, the discrepancy is explained in the low fluence samples due to an overestimation of the depleted volume, and vice verse a underestimation in the high fluence sample, in addition to the uncertainty of leakage current measurements. The RD50-MPW1 and RD50-MPW2 are not included in the figure due to the unconventional leakage current and the large fluctuations in measure leakage current, respectively. The RD50-MPW2 samples on the other hand show an increase leakage current for each increasing fluence level. The overall lower increase in leakage current for the RD50-MPW2 compared to the CCPDv3 samples is also attributed to the fact that the depletion volume is significantly larger in the case of the CCPDv3.

On the other hand, the RD50-MPW1 samples show significantly different behaviour compared to the other two chips. However, the exponential increase in leakage current is consistent with previous results of higher resistivity non-irradiated RD50-MPW1 chips [104, 73]. This exponential increase is attributed partly to a filling layer the foundry added during production and partly to the lack of guard rings between implants and chip edge, and is described in more detail in section 4.2.2. While breakdown voltage of the chip is approximately 56V, this is never reached during measurements of the non-irradiated samples as all measurements were done with a compliance setting of 25 μA. However, it was found that the leakage current decreased with each increasing fluence

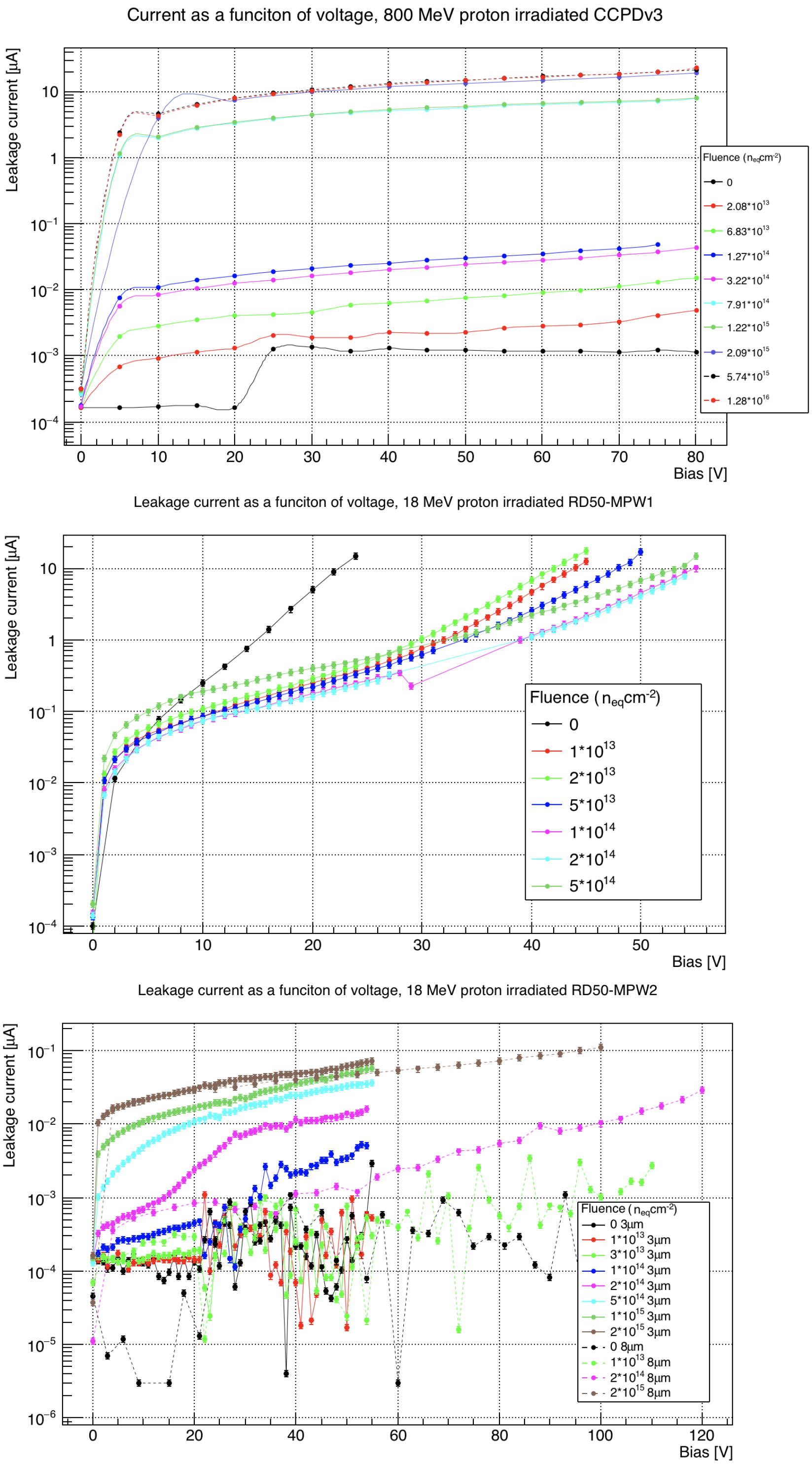

Figure 6.1.1: Leakage current as a function of reverse bias voltage for the three sets of irradiated low resistivity HV-CMOS samples in this study. Top: 800 MeV proton irradiated CCPDv3 chips. Measurements were done at -15±0.5 °C. Middle: 18 MeV proton irradiated RD50-MPW1 chips. Measurements done at 2±1 °C. The high and non-saturating leakage current is attributed to a partly conductive filling layer added by the foundry during production. More details in section 4.2.1. Bottom: Neutron irradiated RD50-MPW2 chips, including both the 3 μm and 8 μm structure. 8 μm measurements used the rounded corner structure. Measurements done at 2±1 °C.

step, and only the last fluence step shows an increase in leakage current. While normally energy levels introduced near the surface can increase surface currents, here it hints at having the opposite effects. As can be seen in the implant layout in figure 4.2.2, there are STI[3]s situated between the conductive filling materials in the chip. The STIs are simply small groves for the oxide to extend into the bulk of the sensor. As explained briefly in 3.3, after irradiation hole charges accumulate in the Si-SiO_2 interface, attracting electrons. Additional energy levels are also introduced. Normally these two effects would lead to increased leakage current in the surface. However, an explanation for the reduced leakage current with irradiation can be that these surface defects act as recombination centres between the conductive fillings, ultimately reducing surface leakage current with increasing fluence. The increase in leakage current in the last sample is simply attributed to the bulk generation, which is strictly increasing with increasing fluence, eventually becoming larger than the surface current.

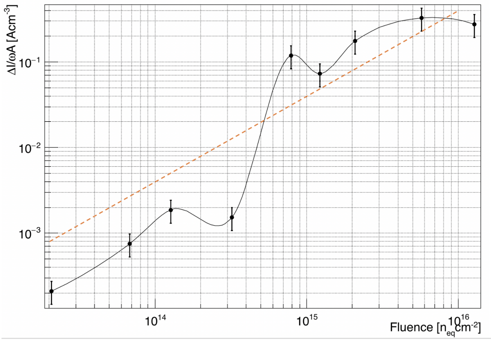

Figure 6.1.2: Fluence dependence of leakage current normalised to depletion volume. The red line are are measurements from [80]. The discrepancy is explained by overestimation of depletion volume for the low fleunce samples and an underestimation, due to lateral growth, in high fluence samples.

In order to be able to improve the results above and derive the *current related damage rate* it is suggested to perform current measurements in a dedicated IV setup, using a pico ammeter and a climate control chamber to accurately measure the current at different temperatures. This would be particularly interesting for the RD50-MPW1 samples, to measure activation energy and the discrepancy with expected values for silicon.

---

[3] Shallow Trench Isolation

6.2 edge-TCT measurements

This section introduces the main results in the investigation of the irradiated low resistivity HV-CMOS samples. Starting with a short discussion on the waveforms, to then focus on the charge collection. Due to using IR light and doing eTCT, the waveforms themselves are more limited in information compared to top and bottom TCT. From the charge collection, different studies can be done. Charge collection over time reveals a loss of diffusion contribution to the signal over irradiation. Furthermore, a new method, building on previous work from Marcos Fernandez in [32], is explored to more accurately extract the N_{eff} in cases where the depletion width is on the same order of magnitude as the laser beam width used to measure it. The acceptor removal coefficient is estimated and compared to published results. Lastly, the Hamburg model is fitted to the N_{eff} data from the annealing study and compared to results of well studied detectors.

Prior to any measurement, area scans are done to locate the passive diode and determine its centre. The focus is calibrated for each sample measurement using the knife edge scan technique. This is especially important when measuring samples were the depletion width is small. These calibration scans were done with 64 averages, while high resolution scans along the sensor depth were done with 128 averages.

The CCPDv3 sample set were measured with the TCT+ setup in the EP-ED-SSD lab at CERN. These measurements, unless otherwise stated, were done at -15 ±0.6°C. The RD50-MPW1 and RD50-MPW2 sample sets were measured with the Particulars TCT setup at Lancaster University. These measurements were done at 1 ±0.6°C, due to limited cooling power. Biasing was done to slightly below breakdown voltage for all samples, except in the case of lowly irradiated RD50-MPW1, which were limited by the high leakage current, where 25 μA was used as compliance level. The RD50-MPW2 sensors were produced on two different wafers, dubbed W5 and W24. All eTCT measurements presented below were done on W24 chips.

6.3 Transient signal

Figures 6.3.1 to 6.3.3 show typical transient signals recorded on the oscilloscope and the DRS4, at different depths into the sensor bulk. Left hand side plots depict the signal in non-irradiated samples and the right hand side show the irradiated sensor which had the biggest increase in depletion region. Due to the nature of eTCT, the signals in all cases are superpositions of the electron and hole signals, albeit the collection time of the two signals will vary depending on the injection position in the bulk. With the bulk being p-doped and readout electrode being n-doped, the electrons drift towards the readout electrode, and the holes in the opposite direction. A visualisation of where the waveforms are compared to a charge collection vs depth scan can be found in section 5.5.2.

The CCPDv3 signals, seen in figure 6.3.1, are recorded with an Agilent DSO9254A oscilloscope, using 2000 data points and 128 averages over 100 ns. The oscilloscope is triggered using the *trigger out* from the pulse generator used to control the pulsed laser. The RD50-MPW1 and RD50-MPW2 signals, seen in figure 6.3.2 and 6.3.3 respectively, are captured using the PSI DRS4, using 1024 data points and 128 averages, capturing 200 ns. The DRS4 is triggered on the trigger out from the laser driver.

The non-irradiated CCPDv3 reveals a collection time below 2 ns for the majority of the carriers, while the non-irradiated RD50-MPW1 and RD50-MPW2 show a collection time just below 4 ns. Due to the inferior time resolution of the DRS4, used to measure the RD50-MPW1 and RD50-MPW2 samples, the transient signals are unfortunately smoothed out in the majority of the measurements. It should be noted though, that the longer collection time is not a result of the DRS4, as approximately similar times were seen with the Tektronix oscilloscope prior to the use of the DRS4. The oscillating pattern in figure 6.3.2 and 6.3.3 is noise induced by the laser driver. While it normally would make the waveform harder to analyse, due to its stable nature the impact on the charge collection results should be limited.

The non-irradiated samples show a fast drop in signal when moving into the bulk. The majority of signal produced by drift is gone in the CCPDv3 sample after moving 20 μm into the bulk from peak charge collection position, and in the RD50-MPW1 and RD50-MPW2 this happens already after only 10 μm. This makes sense with the CCPDv3 having twice the resistivity of the other two sample sets and also a higher bias voltage. Additionally, a tail after the initially collection of the majority of the carriers is visible in the case of all non-irradiated samples. This is most likely due to charge carriers generated close to the edge of the depletion region diffusing into the depletion region and starting to drift.

Both the irradiated CCPDv3 and RD50-MPW1 seen below show slight increase in signal height, but a significant increase in depletion depth, with signal height dropping to half at approximately 60 μm into the bulk in the CCPDv3 sample and 90 μm in the RD50-MPW1. The depletion width is studied in more detail below. The decrease in signal follows the same pattern in both of these detectors. It's noticeable that the RD50-MPW1 appears to have larger depletion region than the CCPDv3, at less fluence and bias voltage, even though the initial resistivity is lower. A possible reason to this is the lower energy proton having a higher acceptor removal factor, increasing the resistivity faster in the RD50-MPW1 compared to the CCPDv3. This is further investigated in section 6.5.2.

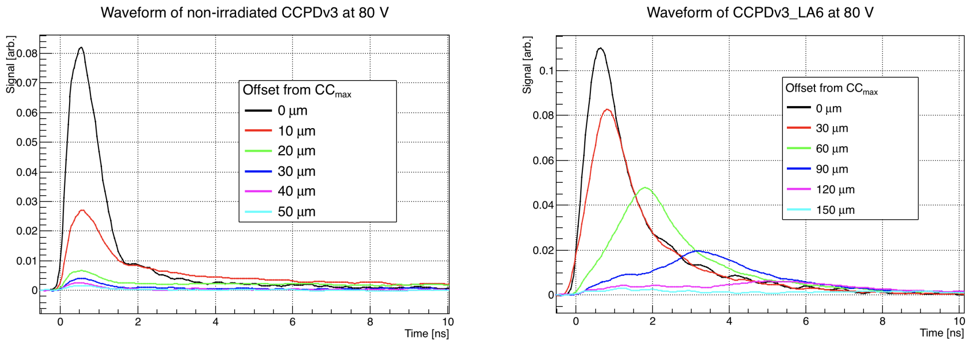

Figure 6.3.1: Transient current signal in CCPDv3 sensors at different distances into the bulk from peak charge collection. Left shows a non-irradiated sensor. Right shows a sensor irradiated with 800 MeV protons to $1.22 \cdot 10^{15} n_{eq}/cm^2$ fluence.

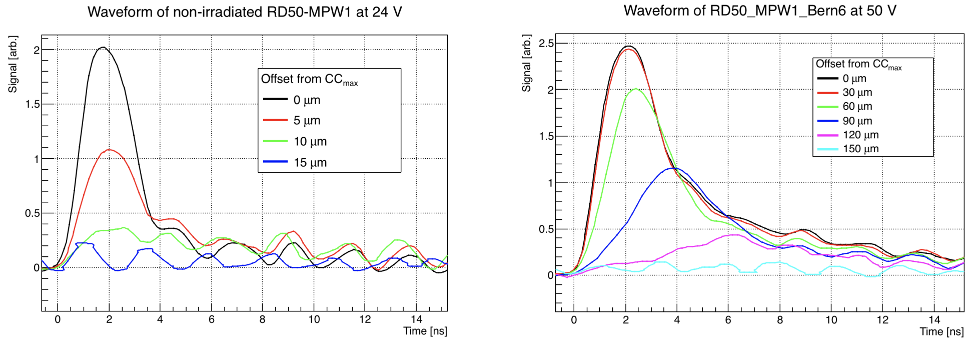

Figure 6.3.2: Transient current signal in RD50-MPW1 sensors at different distances into the bulk from peak charge collection. Left shows a non-irradiated sensor. Right shows a sensor irradiated with 18 MeV protons to $5 \cdot 10^{14} n_{eq}/cm^2$ fluence.

It is notable though that the majority of charge is collected within 4 ns at measured fluences in the CCPDv3 and RD50-MPW2. The RD50-MPW1 show slightly longer collection times, with the majority being collected within 6 ns when generated inside the depletion region. These fast collection speeds, even at fluences matching what is expected in the HL-LHC is promising.

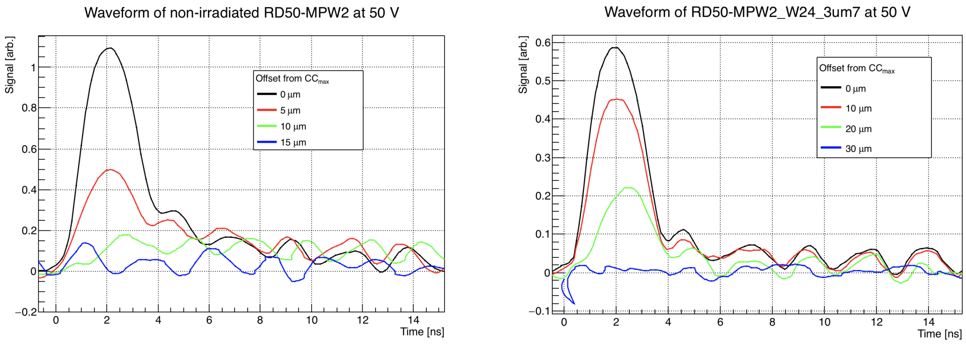

Figure 6.3.3: Transient current signal in the 3 μm test structure on the RD50-MPW2 sensor at different distances into the bulk from peak charge collection. Left shows a non-irradiated sensor. Right shows a sensor irradiated with reactor neutrons to $2 \cdot 10^{15} n_{eq}/cm^2$ fluence.

6.4 Charge collection

Ramo's theorem, and especially equation 2.3.2, it is known that by integrating the current signal the collected charge can be calculated. However, without having a calibrated fixed laser intensity, or even better, actively measuring the laser intensity during illumination, the exact amount of collected charge will be unknown. The Particulars setup at Lancaster University at the moment of measurements did not have any laser monitoring system. The TCT+ setup does actively monitor the laser intensity, however it is not calibrated to a certain amount of electron hole pairs per injection. This is, however, not of importance in this study, as it is the comparison in collected charge between non-irradiated samples and irradiated samples that is of interest.

If nothing else is stated, all charge collection calculations are done with an 8 ns integration window. As partly seen in the previous section and also the next section, virtually all samples collect the majority of the signal within 5 ns. Thus 8 ns integration should include all collected drifting charge carriers, apart from trapped charges, while still excluding the majority of diffusion. The timestamp for the start of signal is calculated individually for each waveform, and it is the first time where the signal reaches half of its maximum. The final timestamp used for the integration is then derived by deducting 1 ns from the mean of all the individual timestamps. Using the mean is to avoid wrongly calculated timestamps for a few waveforms, which can happen when the signal maximum is on the same order as the noise.

6.4.1 Charge at different collection times

In order to get an idea of the diffusion contribution to the charge collection, the accumulated charge as a function of integration time is evaluated in figures 6.4.1 to 6.4.3. These measurements are done at the position in the bulk where charge collection is at maximum for each sample. This maximum can be seen in figures in section 6.4.3. The small dips in charge seen at 30 ns in figure 6.4.1 and at 20 ns in figures 6.4.2 and 6.4.3 are due to signal reflection in the bias tee as a result of impedance mismatch.

All samples, non-irradiated and irradiated, show a quick rise in charge within the first 4 ns, as is expected with the laser injection taking place close inside the depleted region causing the charge carriers to drift. In the non-irradiated CCPDv3 sample, there is a clear continuous increase in charge with increasing integration times. This increase in charge is attributed to charges created outside the depletion region, in front and behind, eventually entering the depletion region after some diffusion to then start drifting and being collected. Ignoring the large dip at 30 ns, this slow increase in charge can also be seen in the non-irradiated RD50-MPW1 and non-irradiated RD50-MPW2 samples.

On the other hand, the irradiated samples show a different picture. In the CCPDv3 sample set, already for the lowest fluence point the curve stays flat after the initial rise, and stays flat for all irradiated samples. This clearly shows that the introduced defects act as trapping or recombination centres, suppressing the diffusion contribution in the signal. Similar effects can be seen in RD50-MPW1 and RD50-MPW2, however, the lowest fluence point in both sets appears to slightly retain some contribution from diffusing charges, while higher fluence points do not. Another discrepancy between the CCPDv3 set and the other two, is that the highest fluence points in both RD50-MPW1 and RD50-MPW2 show increasing accumulated charge with increasing collection time, similar to the non-irradiated case. However, it is highly unlikely to be a contribution from diffusing charge carriers in this case. Rather, the increase could be explained as a result of significant trapping of drifting charges that slowly gets de-trapped over time. An explanation to why this seems to be less prominent in the CCPDv3 sample set is the lower temperature during measurement, suppressing de-trapping and having more recombination compared to the other two sample sets. This pattern is consistent in all samples, except the $5 \cdot 10^{14} n_{eq}/cm^2$ RD50-MPW2 sample, which is deviating in that it has a slower initial charge collection than all the other samples, and the curve flattens out only after around 25 ns. The reason for deviating behaviour is not certain, and while unlikely might be due to bad wire bond connections, or possibly other manufacturing faults.

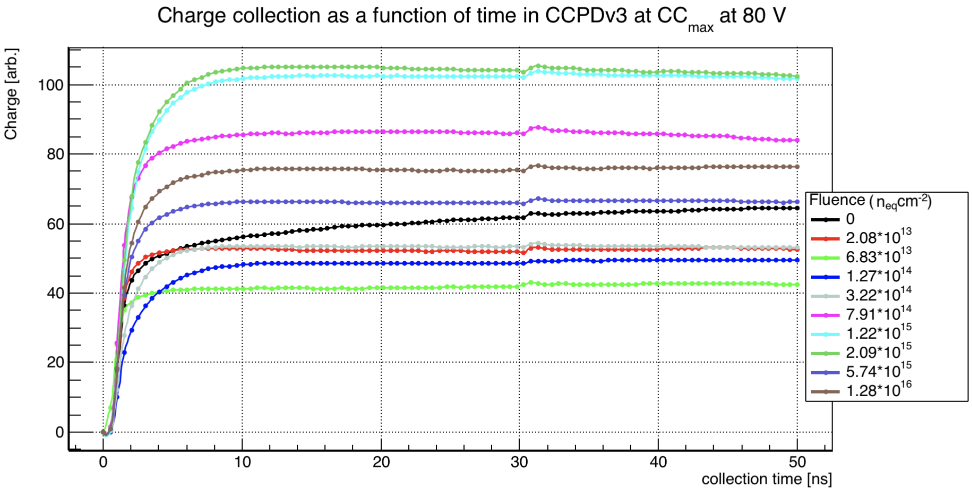

Figure 6.4.1: Accumulated charge as a function of integration time in the CCPDv3 sample set. The position of CC$_{\text{max}}$ for each sample can be found in figure 6.4.14. The fast initial rise is due to the drifting charge carriers, and the slow rise seen for the non-irradiated sample is due to diffusing charges. The bump at t = 30 ns is due to pulse reflection in the system.

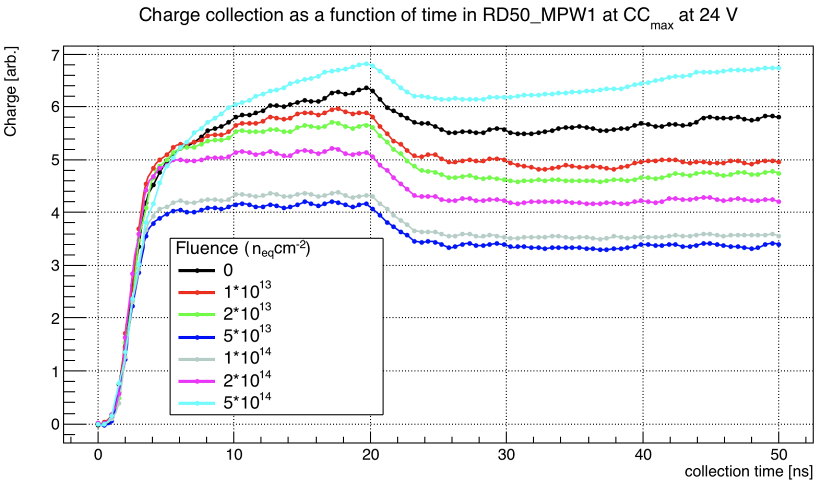

Figure 6.4.2: Accumulated charge as a function of integration time in the RD50-MPW1 sample set.The position of CC$_{\text{max}}$ for each sample can be found in figure 6.4.16. Fast rise is due to contribution from drifting charge, while the slow rise seen in the non-irradiated sample is due to diffusing charges. The slow rise seen for large t in the $5 \cdot 10^{14}$ sample is possibly due to some of the trapped charges getting de-trapped and contributing to the signal again [61]. The large dip after t = 20 ns is due to pulse reflection.

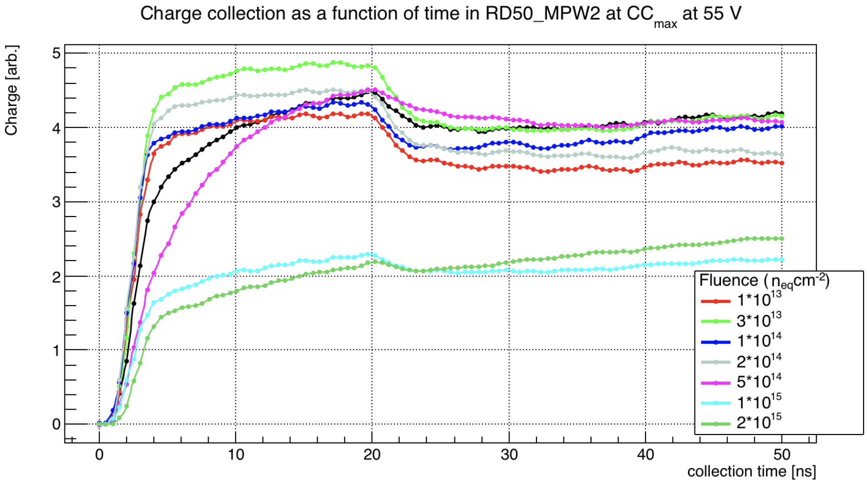

Figure 6.4.3: Accumulated charge as a function of integration time in the RD50-MPW2 sample set.The position of CC$_{\text{max}}$ for each sample can be found in figure 6.4.17

6.4.2 Charge collection surface scans

Charge collection scans over the surface of edge of the sensors were done for two reasons. Firstly, they were done to pin point the center of the test structure before charge collection scan over the depth of the sensor was performed. These kinds of surface scans were done with low resolution and 64 averages on the oscilloscope to quickly get a rough visualisation. Apart from these rough scans, high resolution surface scans were done to investigate local behaviour of the depletion region in the RD50_MPW2 samples. The high resolution scans were done after optimal focus of the laser had been found. The surface scans are done by moving the x and y stages at fixed increments and taking a measurement at each step, using 256 averages on the oscilloscope to have minimal noise.

No sample edges were polished prior to the eTCT scans, which is sometimes done to ensure minimal light scattering at the air-silicon interface. Normally the dicing at the foundry is of high quality and the edges are sufficiently clean for eTCT measurements without prior edge treatment. Almost all samples show a homogeneous and/or symmetrical charge collection over the depletion region similar to what is seen in figure 6.4.4, confirming a suitable edge for eTCT. However, two samples show some edge defects, both from the RD50_MPW1 set, in the form of non-homogeneity in the charge collection.

Firstly, the non-irradiated RD50_MPW1 sample showed a local reduction in charge collection. This could be attributed to a small damaged spot on the surface as seen in figure

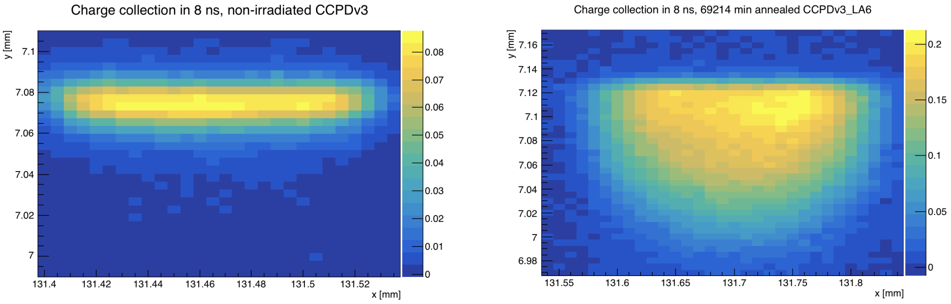

Figure 6.4.4: Examples of charge collection scans, indicating a good edge for eTCT. *Left*: Non-irradiated CCPDv3. The structure width, 100 μm, is clear in the scan. *Right*: CCPDv3_LA6. Clear lateral increase in depletion region.

6.4.5 below. The remaining part of the passive test structure appears homogeneous and deemed sufficiently good to use to measure the depletion depth. The unevenness in the scan is due to a wiggle in the translation stages in the Lancaster University TCT setup. Secondly, the MPW1_Bern4 sample showed reduced charge collection on the left hand side as shown in figure 6.4.6 below. However, no matching defect was seen on the surface of the chip, and the cause of the reduction is unknown. The sample is still used as a data point for its fluence, with an increased error estimation compared to the rest of the samples, and the scan along depletion depth was done off-centre along the red arrow seen in the figure.

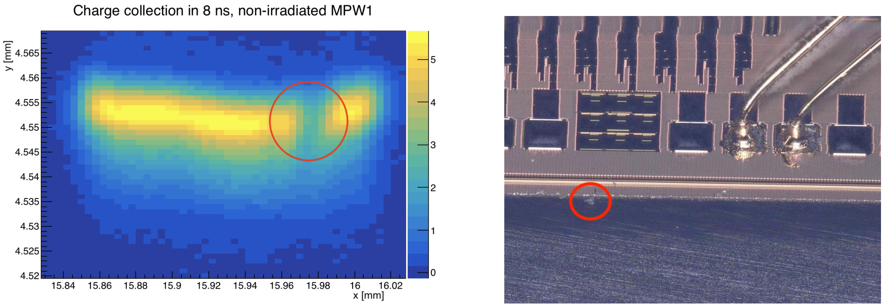

Figure 6.4.5: Damage on detector surface, seen on the right, scattering the incoming laser light reducing the charge collection on that spot seen on the left.

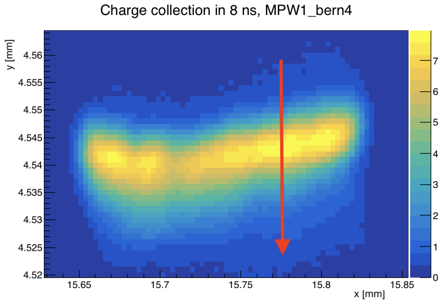

Figure 6.4.6: Reduced charge collection in the RD50-MPW1_Bern4 sample. Depletion depth scan done along the red arrow position instead of centre of diode, as is the case for all other samples.

Local distortion in charge collection in RD50-MPW2 samples

While the remaining of the RD50-MPW1 and CCPDv3 samples show homogeneous and symmetrical charge collection 2D scans, the 8 μm structure on the RD50-MPW2 exhibits a deviating behaviour when approaching voltages close to breakdown. As can be seen in figure 6.4.7 through 6.4.10, when bias voltage goes above approximately 70V the charge collection close to the electrodes start increasing faster than in the depleted region, with significant differences close to breakdown voltage.

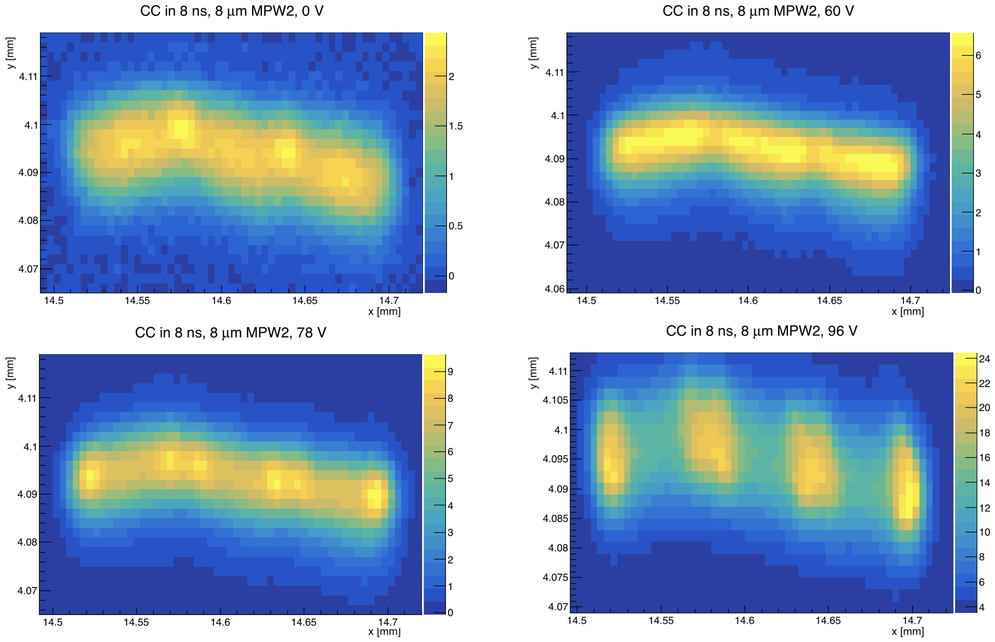

Figure 6.4.7: Charge collection area scans of non-irradiated RD50-MPW2, 8 μm structure. Large charge collection is observed close to the bias electrodes above 78V bias.

An explanation to this could be the high electric field close to the surface between the electrode and deep-n well which might cause a small avalanche effect when a large amount of charge carriers are injected close to this region. While the electric field

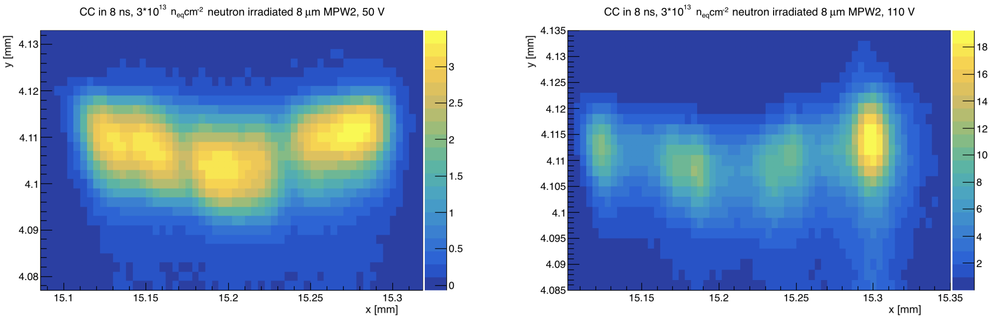

Figure 6.4.8: Charge collection area scans of $3 \cdot 10^{13} n_{eq}/cm^2$ neutron irradiated RD50-MPW2, 8 μm structure. Very large charge collection in one bias electrode at maximum bias voltage. At lower voltages the depletion region appears to not cover the gap between the pixels.

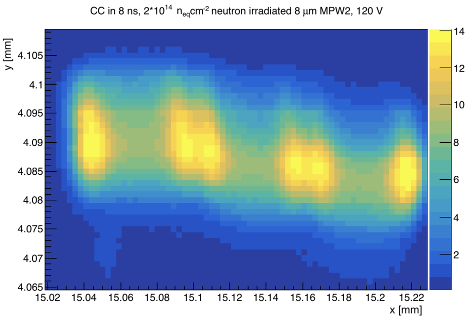

Figure 6.4.9: Charge collection area scans of $2 \cdot 10^{14} n_{eq}/cm^2$ neutron irradiated RD50-MPW2, 8 μm structure. Still showing high charge collection at the HV electrodes, but slightly less so than the non-irradiated sample.

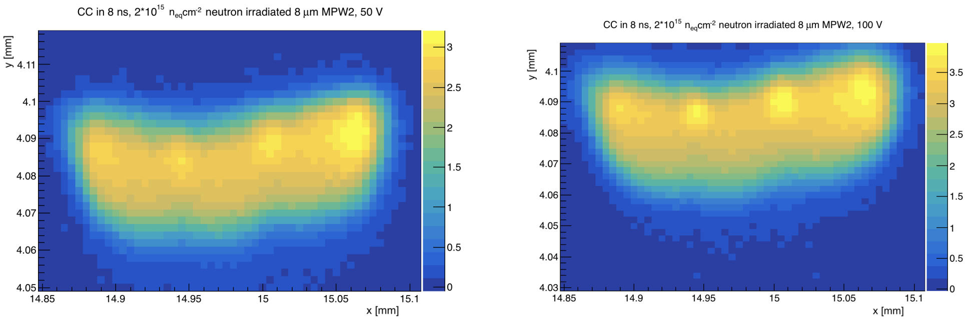

Figure 6.4.10: Charge collection area scans of $2 \cdot 10^{15} n_{eq}/cm^2$ neutron irradiated RD50-MPW2, 8 μm structure. Reduction of the effect of high charge collection at the HV electrodes compared to lower fluences.

between the bias electrode and the deep n-well is non trivial to calculate, a TCAD simulation during design was produced, revealing small regions of high electric fields close to the biasing electrode, as can be seen in 6.4.11. Positionally this agrees well with what is observed in the figures above, however, the absolute value of the electric field was not available at the time of writing. While it is clear that the electric field is not high enough to cause a avalanche breakdown, considering that the generation rate through impact ionisation scales linearly to the concentration of drifting charge carriers

[40], it is reasonable to imagine that there is signal gain through impact ionisation after significantly large injection of charge carrier in these regions. However, to verify this it would be of interest to do more simulations to get the value of the electrical field at different biases, and also to use a calibrated eTCT experiment where the amount of injected charge carriers per unit distance is known. Additionally, with the recent development of the so-called TPA-TCT[4], more detailed mapping of the regions could be achieved. The TPA-TCT utilizes a pulsed femtosecond laser, at wavelength energies below the band gap energy, and excites electron into the conduction band through the Two Photon Absorption process. This method can achieve one order of magnitude smaller beam spot compared to a conventional laser, thus allowing for high resolution TCT scans [107]. Additionally, the TPA process only occur at the focus of the beam, where the photon denisty is highest, making it possible to do point-wise injection of charge. This technique would be interesting to utilise here to study the structure with target charge collection injections.

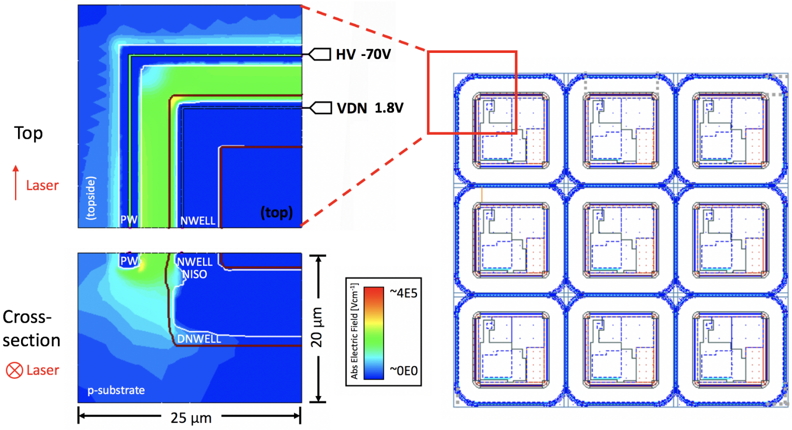

Figure 6.4.11: Top, and cross-sectional view of TCAD simulation of electric field in the RD50-MPW2 8 μm structure at -70V bias. Notably, there is a small region of large electric field close to the biasing electrode. From [33].

The MPW2_W24_8um2, figure 6.4.8, shows extremely high charge collection in the right-most bias electrodes. The cause for this is unknown, but highly likely a manufacturing anomaly. The effect persists, but decreases with increasing fluence, and is only slightly present at $2 \cdot 10^{15} n_{eq}/cm^2$ compared to lower fluences. Another discrepancy is the lack of depleted region between the pixels below approximately 70V in the low- and non-irradiated sensors. At high fluence, as can be seen in figure 6.4.10, due to increased bulk resistivity these gaps disappear. Both of theses effects, depletion region gaps and high fields around electrodes at high voltage were also observed by I. Mandic in the

---

[4] Two Photon Absorption TCT

low resistivity RD50-MPW2 produced on W5 [25]. This excludes wafer anomalies as potential cause. Sensors produced on higher resistivity substrates did not show these effects.

6.4.3 Charge collection along sensor depth

In order to assess the change in active sensing region, scans along the depletion depth were performed, from outside of the sensor into the bulk, along the centre of the passive diode. The centre is determined from area scans similar to the ones in figure 6.4.4. The charge collection scans are done in order to determine increase or decrease in charge collection following the irradiation. It has to be noted that due to the unpolished sensor edge, there might be slight variation in charge carrier generation by the laser light. However, if the area scan showed symmetrical and uniform charge collection, the effect due to the unpolished edge is deemed to be limited, and this was the case in the majority of the samples. Additionally, while a slight decrease in charge generation might give skewed results on the amount of collected charge, the estimation of depletion width is expected to still be largely unaffected. All scans are performed going from outside the top of the detector into the bulk, along decreasing y-coordinates as explained in section 5.4. The sensor edges are located on the left side in all CC vs y (mm) scans below.

800 MeV proton irradiated CCPDv3

The non-irradiated CCPDv3 chip shows as expected little increase in collected charge with increased bias voltage. Notably, even without bias, the maximum charge collection is still over half of the value with high bias. This is most likely attributed to the geometrical structure of the deep n-well, where there is collection of diffusing charges even in absence of a significant depletion region. Increasing fluence initially shows a slight decrease in charge collection until $1.27 \cdot 10^{14} n_{eq}/cm^2$ is reached, after which a slight increase is first observed. Significant increase in depletion region size and charge collection magnitude is observed in all samples irradiated to more than $7.91 \cdot 10^{14} n_{eq}/cm^2$, peaking at approximately $1.22 \cdot 10^{15} n_{eq}/cm^2$. However, it should be noted that even after $1.28 \cdot 10^{16} n_{eq}/cm^2$ [5], charge collection levels are significantly higher than for the non-irradiated sensor. Charge collection at 0V bias gradually decreases with increasing fluence, and becomes negligible after $1.22 \cdot 10^{15} n_{eq}/cm^2$. This is attributed to the amount of increasing lattice defects acting as traps for the charge carriers, and is investigated

---

[5] fluence levels close to expected levels in the innermost pixel layer in the upcoming HL-LHC ATLAS upgrade

further below. Figures 6.4.13 and 6.4.14 show a small peak on the right hand side, around 250 μm from the sensor top, corresponding to the backside of the sensor. While it appears as though a local depletion region is forming in the irradiated samples, it is likely due to light scattering at the bottom corner of the sensor and partly going in to the depleted region in the bulk. To test this, a scan was done horizontally from the depleted region to the right corner of the sensor. As can be seen in figure 6.4.12 below, approximately 650 μm from the middle of the sensing region a small bump can be observed, corresponding to light scattering at the right edge of the detector. Following this, it is most likely that the second peak in the figures below are due to light scattering.

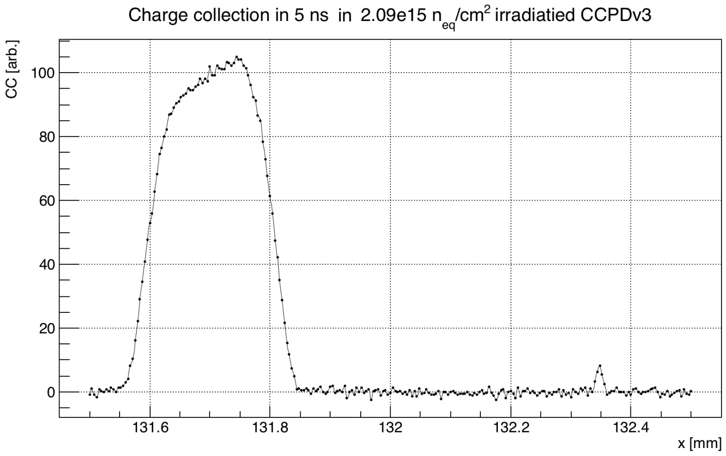

Figure 6.4.12: Lateral charge collection scan along the x axis. The small bump around x = 132.35 mm coincides well with the distance to the right edge of the detector and is thus presumed to be light scattering back into the depleted region.

18 MeV proton irradiated RD50-MPW1

The RD50-MPW1 sample set follows a similar behaviour as the CCPDv3 samples, where there seems to be an initial reduction in charge collection following irradiation, to then lead to a significant increase. The non-irradiated sensor was measured only to 24V bias due to the leakage current reaching compliance on the voltage source. It shows relatively large charge collection without any external voltage present, however, due to the low resistivity the depletion region is limited in growth after applying bias. The first two fluence points, $10^{13} n_{eq}/cm^2$ and $2 \cdot 10^{13} n_{eq}/cm^2$, show little difference in comparison to the non-irradiated sensor at equal bias, with the third and fourth fluence points, $5 \cdot 10^{13} n_{eq}/cm^2$ and $10^{14} n_{eq}/cm^2$, showing a reduction in charge collection. The $2 \cdot 10^{13} n_{eq}/cm^2$ sample show a slight increase in charge collection compared to the previous fluence point, however, the increase is small enough that surface roughness cannot be ruled out as the cause. The last fluence point $5 \cdot 10^{14} n_{eq}/cm^2$ reveals a significant increase in charge collection, in both magnitude and width. The profile shape is also similar to the $1.22 \cdot 10^{15} n_{eq}/cm^2$ CCPDv3 sample, where after reaching a maximum the charge collection first decreases slowly, then more rapidly as the laser is moved down the bulk. Finally, bottom right corner in figure 6.4.16, shows how the charge collection at no bias decreases with increasing fluence, similar to the CCPDv3 samples.

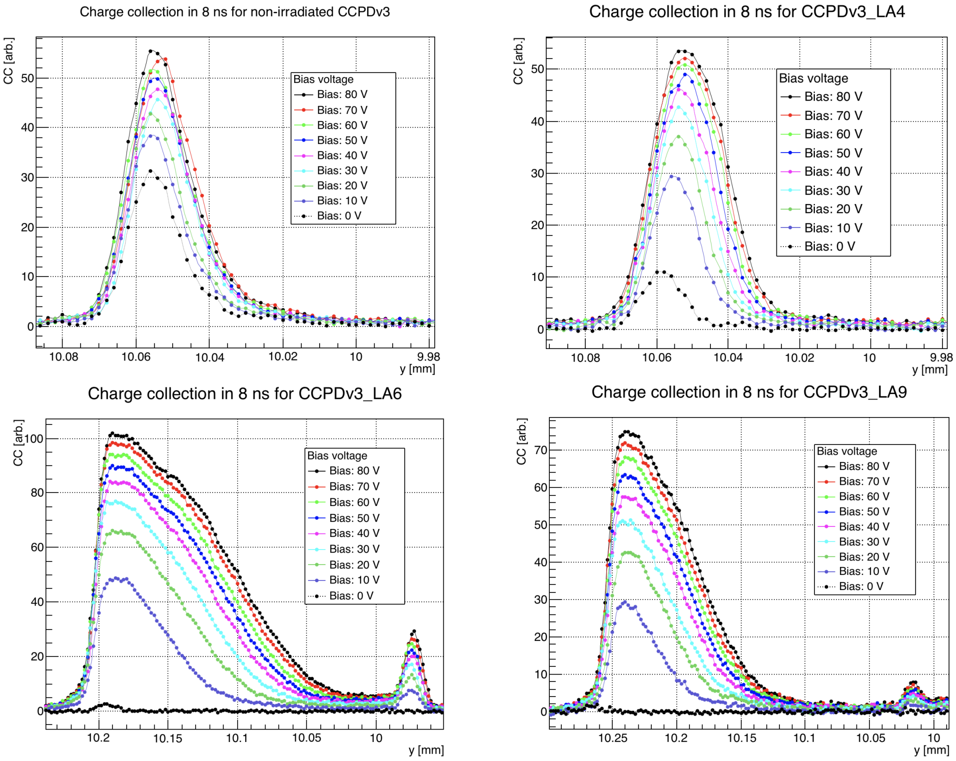

Figure 6.4.13: Charge collection as a function of y coordinate, measured at different biases. *Top left*: Non irradiated CCPDv3. *Top right*: $3.22 \times 10^{14} n_{eq}/cm^2$ 800 MeV proton irradiated CCPDv3. *Bottom left*: $1.22 \times 10^{15} n_{eq}/cm^2$ 800 MeV proton irradiated CCPDv3. *Bottom right*: $1.28 \times 10^{16} n_{eq}/cm^2$ 800 MeV proton irradiated CCPDv3.

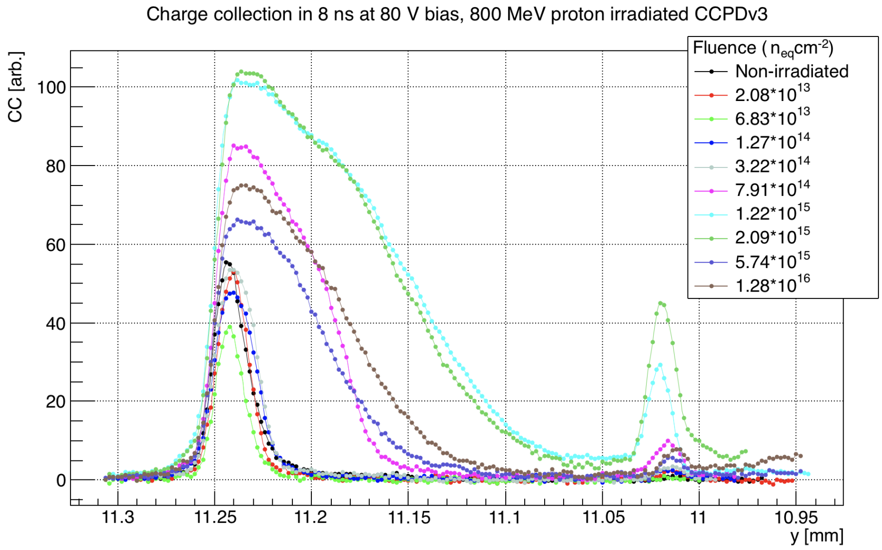

Figure 6.4.14: Charge collection as a function of y coordinate, scanned through the whole sensor for the whole CCPDv3 sample set.

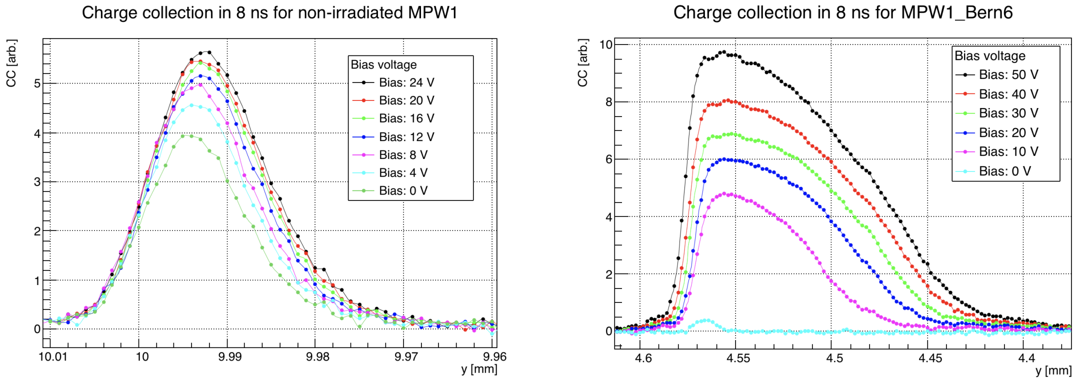

Figure 6.4.15: Charge collection along sensor depth. dy = 1 μm. *Left*: Non irradiated RD50-MPW1 chip. *Right*: $5 \times 10^{14} n_{eq}/cm^2$ proton irradiated RD50-MPW1. Different biases voltage is due to lower leakage current in the irradiated sample.

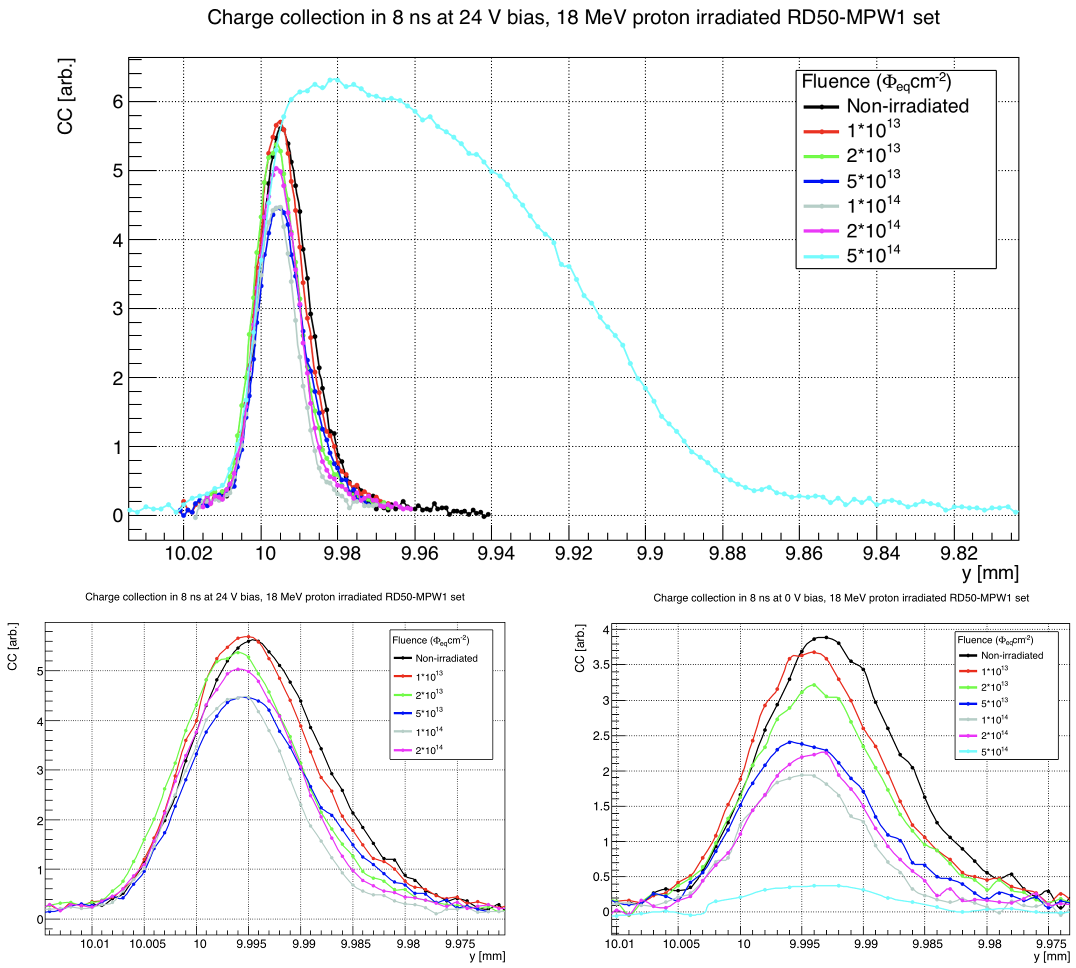

Figure 6.4.16: Charge collection as a function of y coordinate, along the depth of the sensor. *Top*: The whole RD50_MPW1 sample set with 24 V bias. *Bottom left*: Same as top but without the highest fluence sample. *Bottom right*: All samples at 0V bias, highlights reduction in charge collection at no bias.

Both the CCPDv3_LA6, seen on the bottom right of figure 6.4.13, and MPW1_Bern6, seen on the right in figure 6.4.15, both show an increase in CC amplitude with increasing voltage. In the lowly irradiated samples this is alos seen to some extent, but can be explained by growing depletion region being smaller than the laser beam spot, roughly 11 μm, and thus higher bias voltage would lead to larger depleted volume coinciding with the laser. This is not true for the formerly mentioned samples, as the depletion region is already larger than the beam spot for small bias voltages. The increase in charge collection amplitude here is attributed to the large lateral increase in depletion region in these sensors, as is clear in figure 6.4.4, where the lateral extent of the depletion region in non-irradiated sensor is close to the actual implant size of 100 μm, while the irradiated sensor is approximately twice this, around 200 μm. As the depletion region grows laterally with increased bias voltage, increased charge collection is expected with increased bias voltage at the same position.

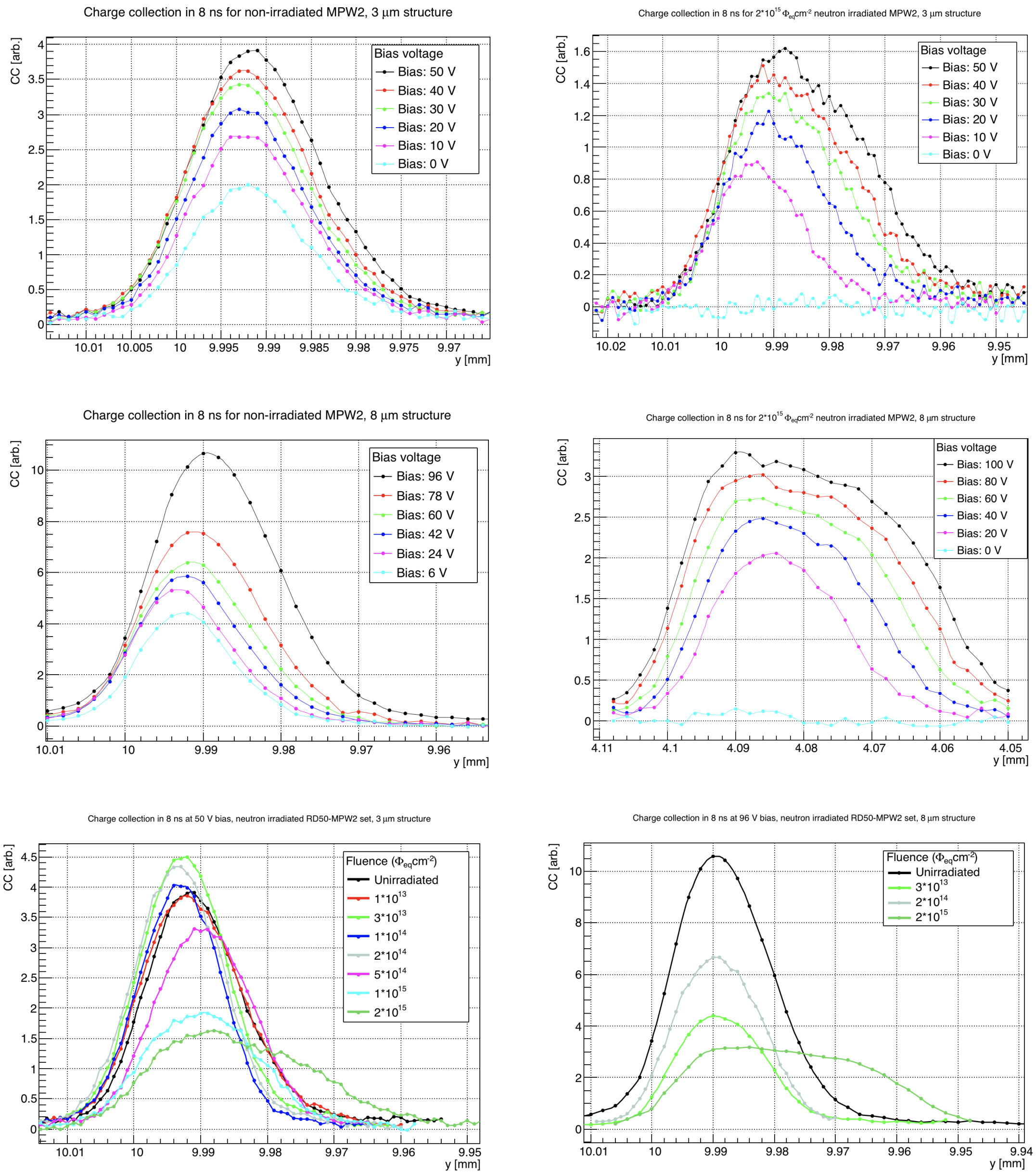

Charge collection in 8 ns for non-irradiated MPW2, 3 μm structure

Charge collection in 8 ns for 2*10^{15} Φ_{eq}cm^{-2} neutron irradiated MPW2, 3 μm structure

Charge collection in 8 ns for non-irradiated MPW2, 8 μm structure

Charge collection in 8 ns for 2*10^{15} Φ_{eq}cm^{-2} neutron irradiated MPW2, 8 μm structure

Charge collection in 8 ns at 50 V bias, neutron irradiated RD50-MPW2 set, 3 μm structure

Charge collection in 8 ns at 96 V bias, neutron irradiated RD50-MPW2 set, 8 μm structure

Figure 6.4.17: Charge collection as a function of y coordinate, along depth of the sensor. *Top left*: Non-irradiated RD50-MPW2, 3 μm structure. *Top right*: $2 \times 10^{15} n_{eq}/cm^2$ neutron irradiated RD50-MPW2, 3 μm structure. *Middle left*: Non-irradiated RD50-MPW2, 8 μm structure. *Middle right*: $2 \times 10^{15} n_{eq}/cm^2$ neutron irradiated RD50-MPW2, 8 μm structure. *Bottom left*: Full sample set at 55 V bias, 3 μ structure. *Bottom right*: Selected fluences at 96 V bias, 8 μm structure.

Reactor neutron irradiated RD50-MPW2

Figure 6.4.20 shows charge collection scans for both the 3 μm and 8 μm structure on the RD50-MPW2 chips. Different sensors were used for the two different structures due to wire bonding limitations. The 3 μm structure behaves similar to its predecessor, with limited depletion region and relatively high charge collection before bias.

However, as could be seen in the area scans, figures 6.4.7 to 6.4.10, the 8 μm structures experiences high charge collection at the bias electrodes compared to the rest of the depleted region at bias voltage close to breakdown. Although the charge collection is largest at the bias electrodes, as can be seen in middle left graph of figure 6.4.17, the charge collection over the middle of the pixel also appears to have an exponential increase.

Studying the charge collection vs fluence, little change is seen in the charge collection at high bias until a fluence of approximately $5 \cdot 10^{14} n_{eq}/cm^2$, above which the absolute charge collection declines. Initially, a bad edge was considered as cause for the decrease in charge collection, however, as both the 3 μm structures irradiated $1 \cdot 10^{15} n_{eq}/cm^2$ and $2 \cdot 10^{15} n_{eq}/cm^2$, undergo the reduction in collected charge, this is unlikely. Furthermore, both the 3 μm and 8 μm structures, tested on different chips, show similar charge collection profiles at the highest fluence, with similarly reduced magnitude. From this, the reduction in absolute charge collection can be attributed to the irradiation, despite the apparent increase in resistivity, which is seen in the increasing depletion region width.

6.4.4 Relative total charge collection over fluence

This section aims to compare the charge collection relative to the charge collection at maximum bias in the non-irradiated sample, for each of the three sample sets. Firstly, the total collected charge at each voltage is quantified by integrating the charge collection over the y-coordinate. In the case of the CCPDv3, the integration excludes the charge collection that can be seen at the bottom edge of the detector, as this is caused by scattering of the laser light. In all the RD50-MPW1 and RD50-MPW2 samples, the integrations were done over the whole measured distance, as most measurements were done only over the depleted region. The calculated total charge collection is then normalised to the charge collection at highest bias voltage in the non-irradiated sample for the respective sample set, to show the relative change in charge collection. This is shown in figures 6.4.18 to 6.4.20 as a function of bias voltage for all samples. As also observed above in the charge collection profile plots, but much clearer here, the charge collection at 0V bias voltage decreases with increasing fluence. This is expected due to the introduction of trapping centres after irradiation leading to increased recombination of charge carriers, and the depletion region at no bias being very limited in size, $\omega < 9.5 \mu m$. Additionally, one should keep in mind that the light absorption increases with fluence [90], leading to an increase in generated charger carriers. As such the increase in normalised collected charge is slightly overestimated.

The CCPDv3 set shows an increase in collected charge at 80 V bias in both the 1.22 and the $2.09{\cdot}10^{15}n_{eq}/cm^2$ 800 MeV proton irradiated samples greater than 8 times, compared to the non-irradiated CCPDv3. Beyond this fluence, the CC starts to decline again, but after $1.28{\cdot}10^{16}n_{eq}/cm^2$ the CC is still 4 times greater than the non-irradiated CCDPv3. While this large increase is promising, figure 6.4.18 also shows that for the two lowest fluence points, there is a decrease in CC, and after $6.83 \cdot 10^{13}n_{eq}/cm^2$ the CC is less than 0.6 times at 80 V bias compared to the non-irradiated sample. After this, the CC increases again to roughly the same level as the non-irradiated case before sharply increasing to the maximum level mentioned above.

The RD50-MPW1 sample set reveals a somewhat similar picture to the CCPDv3 sensors. It should be noted that when comparing the change in CC to the non-irradiated sample, one needs to keep in mind the limited maximum bias of the non-irradiated case. Only comparing maximum CC at maximum bias shows that all irradiated samples perform as good, or better, compared to the non-irradiated case. However, comparing the CC at 24 V, which was maximum bias applied to the non-irradiated sample, or simply extrapolating the CC for the non-irradiated case, figure 6.4.19 shows that CC decreases with fluence until reaching a minimum with the $10^{14}n_{eq}/cm^2$ irradiated sample. The next fluence step after this shows a slight increase in CC, but is still has lower CC than the non-irradiated sample.

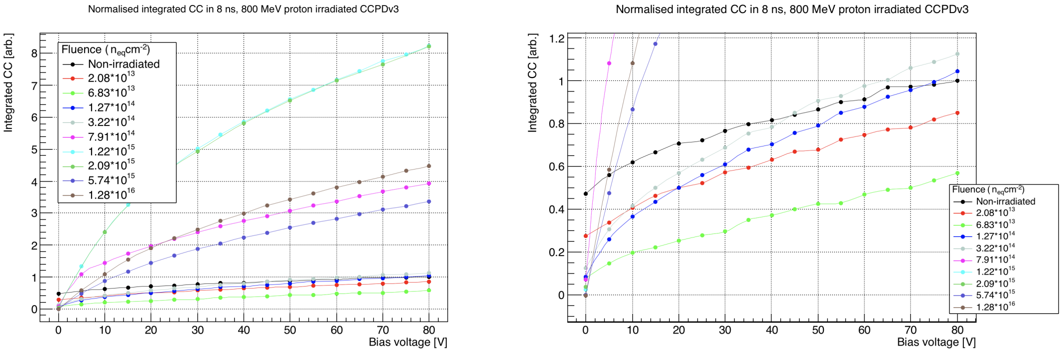

Figure 6.4.18: Accumulated charge integrated over the y coordinate as a function of bias voltage, in 800 MeV proton irradiated CCPDv3. Right plot is a zoom in on the low values.

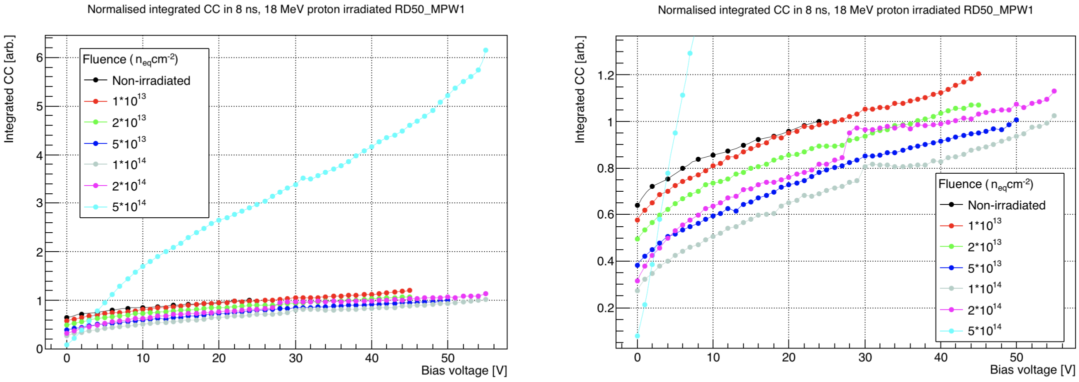

Figure 6.4.19: Accumulated charge integrated over the y coordinate as a function of bias voltage, in 18 MeV proton irradiated RD50-MPW1. Right plot is a zoom in on the low values.

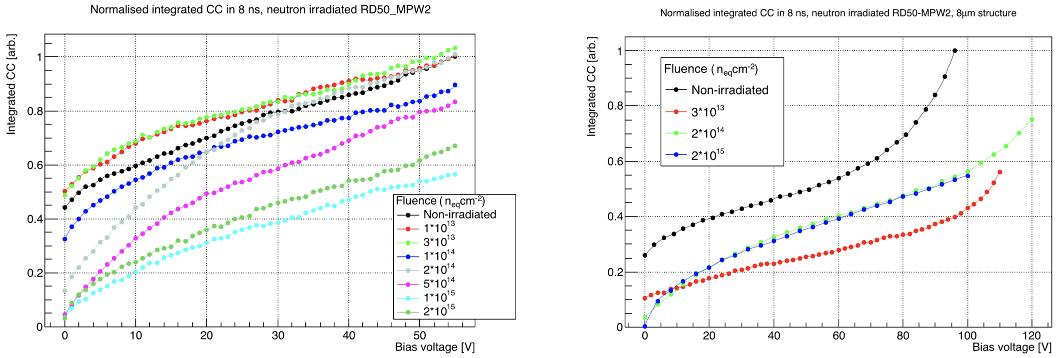

Figure 6.4.20: Accumulated charge integrated over the y coordinate as a function of bias voltage, in reactor neutron n irradiated RD50-MPW2. Left plot shows results using the 3 μm passive structure, and the right plot shows the 8 μm passive structure.

The last fluence point show a significant increase, with CC over 6 times greater than the non-irradiated sample at maximum bias. However, as mentioned above, this ratio is more likely somewhere around 5 times greater due to the limited maximum bias of the non-irradiated sample.

The RD50-MPW2, 3 μm set deviates in behaviour compared to the CCPDv3 and RD50-MPW1 samples. Initially, the CC seem to be stable/even slightly increase after neutron irradiation at 1- and $3{\cdot}10^{13} n_{eq}/cm^2$ fluence. However, it should be noted that the increase is low enough to be considered an effect of difference in light penetration. Further irradiation decreases the CC, without any increase until the highest fluence, $2 \cdot 10^{15} n_{eq}/cm^2$. Only the $2 \cdot 10^{14} n_{eq}/cm^2$ deviates from the continuous decline in CC and shows approximately equal CC at maximum bias as compared to the non-irradiated sample. The 8μm structure also show similar results, with all irradiated samples having lower accumulated charge over the whole bulk. However, here the $3 \cdot 10^{13} n_{eq}/cm^2$ sample shows the lowest charge collection, with the two higher fluences having a slightly higher total charge collection. Additionally, all the 8 μm samples, apart from the $2 \cdot 10^{15} n_{eq}/cm^2$ sample, show an exponential increase in leakage current when approaching maximum bias. These three samples showed even higher charge collection in the biasing electrode, as seen in section 6.4.2, suggesting this being caused by the same effect.

Two potential reasons for the low CC in the neutron irradiated samples could be the limited acceptor removal, resulting in a reduced increase in depletion region compared to the proton irradiated samples, as well as a greater number of trapping centres. As discussed above, neutron irradiation, compared to charged hadrons, introduces more cluster defects which causes less acceptor removal. This is also in line with results from comparing proton and neutron irradiated p-type MCz based sensors, which show a larger decrease in collected charge from neutron irradiation [55]. Neutron irradiated CCPDv3 also show less increase in collected charge compared to the proton-irradiated samples in this study, a 2 fold increase vs an 8 fold increase, respectively [32]. While the increase seen from proton irradiation is promising for operation after large fluences, the decrease from neutron irradiation naturally hinders performance. To investigate the suitability in a HL-LHC environment, a mixed irradiation study is recommended.

6.5 Change in effective doping concentration

Normally, with pad diodes the effective doping concentration can be calculated using the full depletion voltage measured with CV[6] scans. This is however not possible with the samples used here as they are not designed to fully deplete and the effective doping concentration needs to be estimated from the depletion width.

---

[6] Capacitance-Voltage

6.5.1 Depletion width calculations

From the charge collection profiles plotted in the section above, the depletion width can be calculated. This is of interest to understand how the depletion region, and ultimately N_{eff} changes with different irradiation in different sensors. The depletion width is extracted by first calculating the FWHM from the charge collection profile. Traditionally, this suffices to give a good approximation of the depletion width. However, due to the small size of the depletion widths in low resistivity CMOS sensors, the convolution between the laser and the depletion region will also need to be taken into account, aiming to achieve a more accurate value of the depletion width. This is done by extracting the difference of a simulated convolution and ideal depletion region from the measured value. All of these steps are explained in more detail in section 5.5.3. As this method has not been used before, a comparison to the conventional method when calculating N_{eff} can be found in appendix B.

The non-irradiated CCPDv3 sample is shown to have a depletion width of approximately 20 μm at 80V bias. This is slightly higher than expected, with the theoretical value for a 20 Ωcm abrupt junction being around 15 μm. The irradiated samples naturally follow a similar behaviour to the CC profile, with the width slightly decreasing for the two lowest fluence points, followed by a slight increase in the next two fluence points, and thereafter a significant increase is observed, reaching a maximum depletion width of approximately 102 μm around $1.22 \cdot 10^{15} n_{eq}/cm^2$ fluence, to then decrease with further increasing fluence. However, the depletion width after 1.28 $\cdot 10^{16} n_{eq}/cm^2$ is still above 70 μm, significantly larger than before irradiation.

The 10 Ωcm RD50-MPW1 and RD50-MPW2 also show a larger depletion width compared to theoretical values in the non-irradiated samples, with 13 μm and 16 μm measured, respectively, where the expected values would be 5 μm and 7 μm, respectively. It should be noted that an abrupt junction is highly idealised, and in reality there is a gradient in doping concentration over the junction, which can affect the measured depletion width, in particular in the low resistivity samples. Figure 6.5.3 shows how the depletion width decreases slightly with increasing fluence, especially at low biases. However, as is seen in the next section, the N_{eff} does not increase with fluence, therefore this decrease could be an artefact of signal loss due to trapping. As expected from the CC profile, the depletion width increases significantly for the $5 \cdot 10^{14} n_{eq}/cm^2$ sample, reaching over 100 μm at maximum bias.

The sudden, large increase in depletion width for the MPW1_Bern6 sample, as seen in 6.5.2, is not solely attributed acceptor removal, but also to the fact that the removed Boron combines with O_i forming the electrically active B_iO_i, increasing the bulk resistivity rapidly. Additionally, this effect is exaggerated in low MeV energy protons which create a larger amount of point defects compared to higher energies, driving the formation of B_iO_i.This is in agreement with a test beam study on the low resistivity CCPDv4 HV-CMOS prototype that was irradiated with 18 MeV protons, where a decrease in detector efficiency after a fluence of $1.3 \cdot 10^{14} n_{eq} cm^{-2}$ followed by an increase to 100% again after a fluence of $5 \cdot 10^{15} n_{eq} cm^{-2}$ was observed [14].

The irradiated RD50-MPW2 also show an initial decrease in depletion width until $2 \cdot 10^{14} n_{eq}/cm^2$, apart from the lowest irradiated sample, which shows a slight larger depletion width. After $2 \cdot 10^{14} n_{eq}/cm^2$ the depletion width increases with increasing fluence, however, significantly less so than the proton irradiated samples, reaching only 30 μm at maximum bias in the highest irradiated sample. The 8 μm structures of the RD50-MPW2 show the same result. It should be noted that the exponential increase in CC towards higher biases in the 8 μm structure do not seem to affect the calculated depletion width.

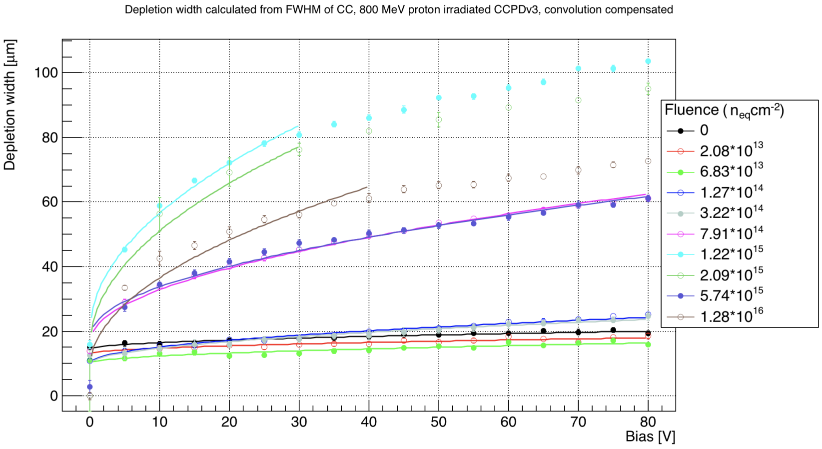

Figure 6.5.1: Depletion width as a function of bias voltage in 800 MeV proton irradiated CCPDv3. Laser beam and depletion region convolution taken into account.

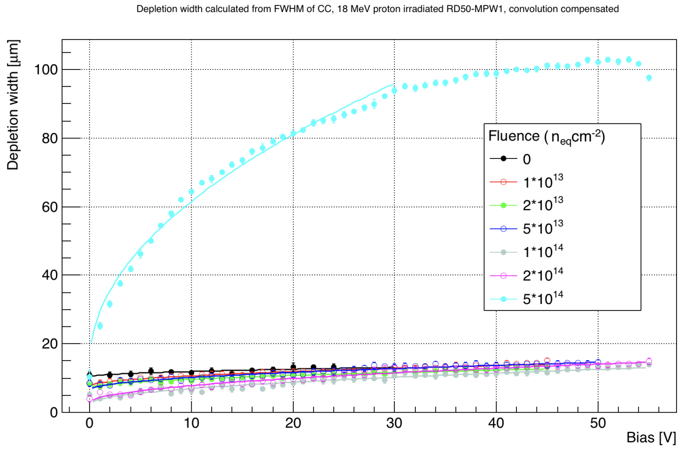

Figure 6.5.2: Depletion width as a function of bias voltage in 18 MeV proton irradiated RD50-MPW1. Laser beam and depletion region convolution taken into account.

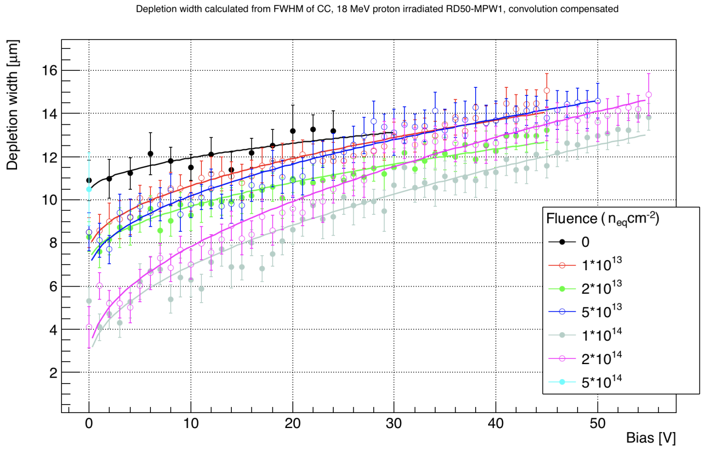

Figure 6.5.3: Expansion of figure 6.5.2 at small depletion widths.

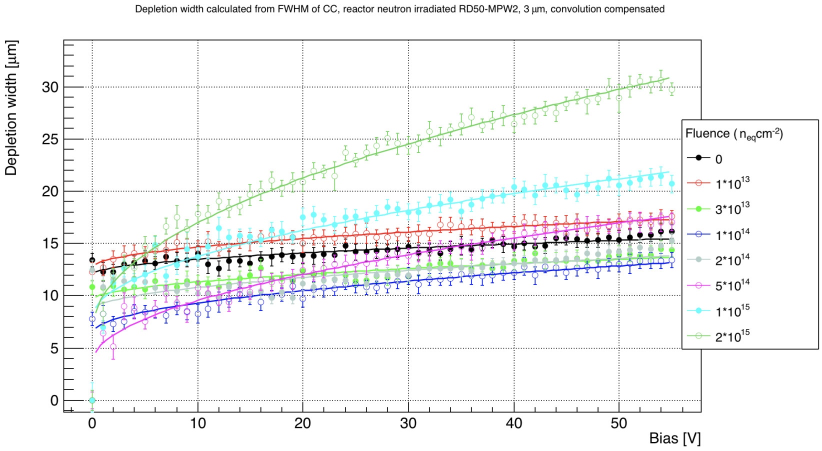

Figure 6.5.4: Depletion width as a function of bias voltage in reactor neutron irradiated RD50-MPW2, 3 μm passive structure. Laser beam and depletion region convolution taken into account.

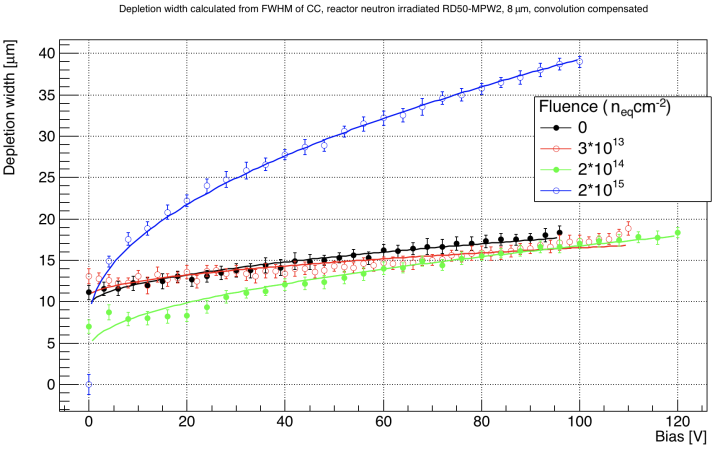

Figure 6.5.5: Depletion width as a function of bias voltage in reactor neutron irradiated RD50-MPW2 , 8 μm passive structure Laser beam and depletion region convolution taken into account.

6.5.2 Change in N_{eff} with fluence

From the depletion width, N_{eff} can be calculated by fitting eq. 5.5.2, where the second fit parameter represents N_{eff}. N_{eff} is calculated for the CCPDv3, RD50-MPW1 and RD50-MPW2 (3μm) and presented in figure 6.5.6 below. Although the values presented are calculated from the convolution-compensated depletion width, the N_{eff} of non-irradiated samples all seem to be overestimated compared to what is to be expected from the given resistivity. The expected values for CCPDv3 (20 Ωcm) are $6.73 \cdot 10^{14} cm^{-3}$, and $1.36 \cdot 10^{15} cm^{-3}$ for both RD50-MPW1 and RD50-MPW2 (10 Ωcm), respectively. With this in mind, the two RD50 sample sets are relatively close to the expected value, meanwhile the CCPDv3 measures approximately 4 times greater than this value. However, as can be seen in appendix A, the values are still closer to the expected value than the values calculated without considering the convolution of the laser beam and depletion region. The overestimation is possibly explained by the deep n-well inflating the charge collection region for the non-irradiated samples, decreasing the effect of compensating for the convolution.

Following the overestimation of the non-irradiated samples, it is reasonable to argue that the likelihood for the first two irradiated data points of all three sample sets being overestimated as well is high. This might be especially true for the CCPDv3 sample set, where a slight increase in N_{eff} can be seen prior to decrease. The increase could be attributed to a bad fit of the depletion width due to low charge collection as a result of trapping while no increase in depletion width has happened.

Irradiated samples with calculated N_{eff} below approximately $5 \cdot 10^{14} cm^{-3}$ are expected to reflect the real N_{eff} more accurately. At this N_{eff}, the charge collection region at low biases is less inflated by the deep n-well, which is not the case in the non-irradiated sample, and a low N_{eff} gives a more distinct increase in depletion width with increasing bias making the fit more accurate.

The CCPDv3 set show a minimum N_{eff} of $9.8 \cdot 10^{12} cm^{-3}$ after $1.22 \cdot 10^{15} n_{eq}/cm^2$ fluence, after which the N_{eff} increases again. Even at fluences above $10^{16} n_{eq}/cm^2$, the CCPDv3 show significantly lower N_{eff} than lowly- or non-irradiated samples. Compared to the CCPDv3, the RD50-MPW1 reaches a minimum N_{eff} of $6.37 \cdot 10^{12} cm^{-3}$ after $5 \cdot 10^{14} n_{eq}/cm^2$ fluence. Due to the lack of samples with higher fluence, it is not possible to say if the N_{eff} would decrease further or if this is the minimum. However, assuming a similar behaviour to most other p-type silicon sensors following proton irradiation, with

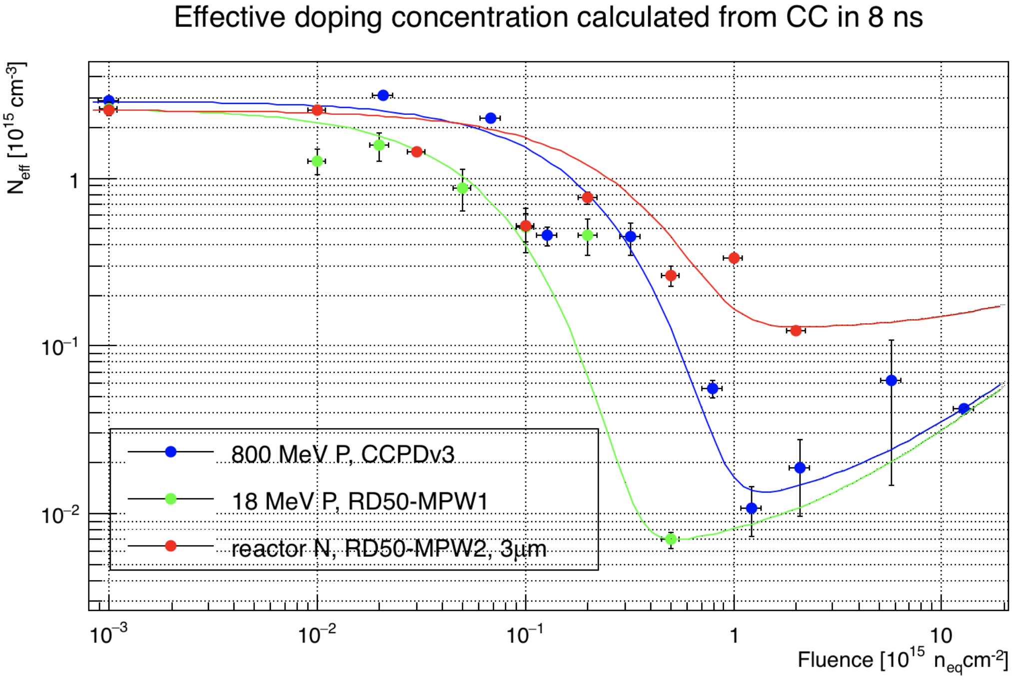

Figure 6.5.6: N_{eff} values calculated from fitting equation 5.5.2 to the calculated depletion width, which can be seen in figure 6.5.1 through 6.5.4.

acceptor removal and further acceptor-like stable damage introduction, the N_{eff} would be expected to start to increase not much after this fluence level. The RD50-MPW2 experiences less decrease in N_{eff} compared to the other two sample sets. This agrees with other results comparing neutron and proton irradiation [28], and can explained by neutron irradiation not causing complete doping removal as opposed to proton irradiation. Similarly to the the RD50-MPW1 set, it is unclear whether higher fluences would decrease the N_{eff} further, or if an increase would occur following stable, acceptor-like defects.

To assess the acceptor removal and dopant-like defect introduction, the data is fitted to eq. 3.4.11 in the form of:

$$N_{eff} = [0] - [1]\left(1 - \exp(-[2]\Phi_{eq})\right) + [3]\Phi_{eq} \tag{6.5.1}$$

Where [0], [1], [2], and [3] are used as fitting parameters. [0] represents the initial doping concentration, N_0, [1] the degree of doping removal, N_c, [2] is the acceptor removal constant, c , and [3] is the doping-like defect introduction rate, g_c. In all three fits in fig. 6.5.6 [0] was fixed to the N_{eff} of the non-irradiated samples for the respective set, [1] was limited between 0 and the [0] value, [2] was left free in all three cases, and [3] was free in the CCPDv3 set, but fixed in the RD50-MPW1 and RD50-MPW2 sets, due to the lack of data points at higher fluences. As can be seen in table 6.5.1, for the CCPDv3 set g_c was calculated to $2.7 \pm 0.05 \cdot 10^{-3} cm^{-1}$. This value is found to be slightly below of what was previously found in different studies, where g_c is stated to be between 0.43 —3.1 $10^{-2}cm^{-1}$ [79, 28, 73, 63, 26]. The reason for this lower g_c is either due to some mechanism suppressing the introduction of acceptor-like defects, or a competing mechanism of introduction of donor-like defects. Which of the two is however unknown. For simplicity, g_c was fixed to the value calculated in the CCPDv3 set, when fitting the equation to RD50-MPW1 and RD50-MPW2. Different values from literature were also investigated, however, the c parameter only changed marginally with different g_c thus the CCPDv3 value was chosen, due to similarity in resistivity and silicon material. The error in the c parameter in both RD50-MPW1, and RD50-MPW2 includes the uncertainty from different values of fixed g_c.

It is known that presence of oxygen in the silicon suppresses the generation rate of acceptor like defects in n-type Fz silicon [69, 68]. Further, MCz silicon diodes, with oxygen concentration levels of a few $10^{17}cm^{-3}$, were also found to have smaller generation rates, in both n- and p-type silicon, compared to standard FZ and EPI diodes [55]. The g_c of the p-type MCz after 24 GeV proton irradiation was found to be $7.42 \cdot 10^{-3}cm^{-1}$. Considering the oxygen concentration to be even higher in this Cz sensors, as is seen in appendix A, it is reasonable that the higher oxygen concentration suppresses g_c further. Additionally g_c was found be lower for lower energy charged hadrons [55]. Considering this, the lower proton energy here might also be a contributing factor to the lower g_c.

Sample set	N_0 [10^{15}cm^{-3}]	N_c [10^{15}cm^{-3}]	c [10^{-15}cm^2]	g_c [10^{-3}cm^{-1}]]
800 MeV p-irrad CCPDv3	2.87 ± 0.11	2.86 ± 0.039	6.43 ± 0.33	2.6 ± 0.05
18 MeV p-irrad RD50-MPW1	2.60 ± 0.22	2.59 ± 0.04	18.8 ± 4.2	2.6 (fixed)
n-irrad rd50-MPW2	2.53 ± 0.08	2.41 ± 0.12	4.05 ± 1.13	2.6 (fixed)

Table 6.5.1: Parameters achieved from fits in figure 6.5.6. Due to limited data points at high fluence g_c was fixed in the case of RD50-MPW1 and RD50-MPW2.

Further, both proton irradiated sets show $N_c \approx N_0$ meaning in both cases close to complete acceptor removal can be assumed. On the other hand, the neutron irradiated sample have $N_c/N_0 \approx 0.95$, which means that there is only partial acceptor removal. Both of these results agrees with previous results [28].

The acceptor removal constant, c, appears consistent with results from different p-type silicon detectors as can be seen in figure 6.5.7. The 20 Ωcm CCPDv3, shows approximately 2 - 4 times higher c as compared to neutron irradiated HV-CMOS, following the trend where proton irradiated silicon show larger c. The neutron irradiated RD50-MPW2, has $c = 4.05 \pm 1.13 \cdot 10^{-15} cm^{-1}$, which falls between neutron irradiated epitaxial, $c = 3.39 \cdot 10^{-15} cm^{-1}$ and neutron irradiated HV2FEI4, $c = 5.7 \cdot 10^{-15} cm^{-1}$. However, the RD50-MPW2 estimates a c twice as large as compared to previous proton irradiated epitaxial diode data. While, initial impurities are different, an explanation for the high c could be due to the the low energy of the proton irradiation, 18 MeV vs 24 GeV. It is suggested that the generation of B_iO_i defect after B_s is removed from the lattice is one of the main drivers for the acceptor removal effect [78]. Additionally, point defects drive the generation of B_iO_i[7]. With lower energy protons (∼MeV) inducing more point defect compared to higher energy protons (∼GeV) as seen in [50], it would be expected that the 18 MeV proton irradiation results in a higher c.

Complementary to this study, to better understand the effect of irradiation on low resistivity Cz in general, DLTS[8] and TSC[9] measurements could be carried out to quantify the introduction rate of specific defects. This was attempted in the current study, however, the test structure in the samples used in this study proved to have too small depleted volumes to yield any useful results. Therefore, to carry out such a study, it would be recommended to produce planar diodes with large pn-junctions together with detector prototypes.

6.5.3 N_{eff} after isothermal annealing in CCPDv3

After initial measurement were done on the CCPDv3 set, an annealing study was carried out, to investigate whether the sensors' annealing behaviour followed the Hamburg model described in section 3.5. Firstly, due to the discrepancy in initial annealing states all samples were brought to the same accumulated time at RT, 6235 minutes, which the two samples with highest fluence already had. This number was the approximated to the equivalent time, 27 minutes at 60 °C, using acceleration constants for short term annealing from [79], after which all samples were annealed for 53 minutes to reach 80 minutes of accumulated equivalent time at 60 °C. All isothermal annealing was done using a high precision oven with $< \pm 1°C$ deviation.

After this, two samples, CCPDv3_LA6 and CCPDv3_LA9, were isothermally annealed

---

[7] $I + B_S \rightarrow B_i, B_i + O_i \rightarrow B_iO_i$. See section 3.3.3

[8] Deep-Level Transient Spectroscopy

[9] Thermally Stimulated Current spectroscopy

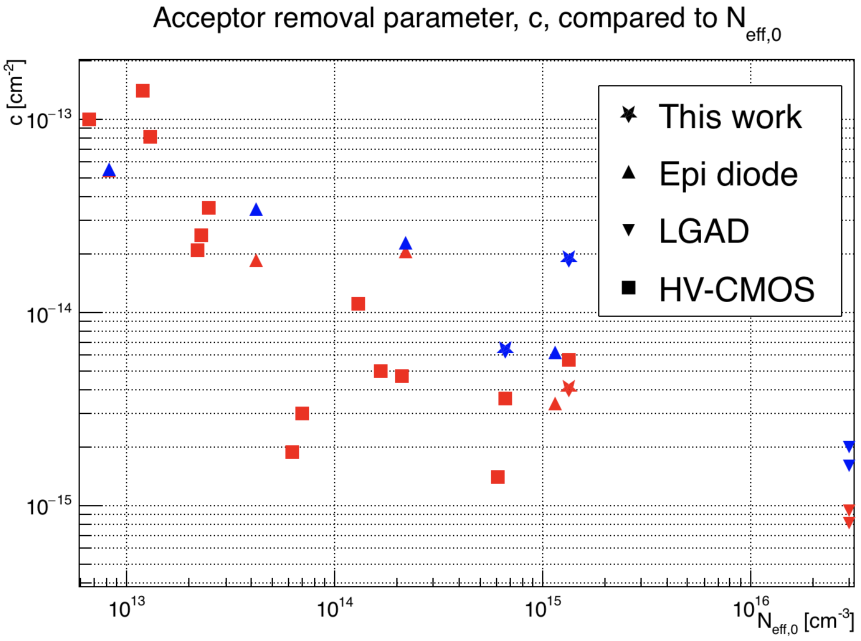

Figure 6.5.7: Comparison of calculated c, to results from different p-type silicon detectors. Red markers indicates neutron irradiation, and blue markers indicate charged hadrons. Epitaxial diode results taken from [28]. LGAD results taken from [62]. HV-CMOS results from [46, 45, 75, 73, 74, 3, 19]

at 60 °C at increasing time steps to investigate the long-term annealing effect, with time steps as listed in table 6.0.4. The Hamburg model is evaluated by fitting eq. 3.5.4, where eq. 3.5.5 and 3.5.6 are substituted in their respective places.

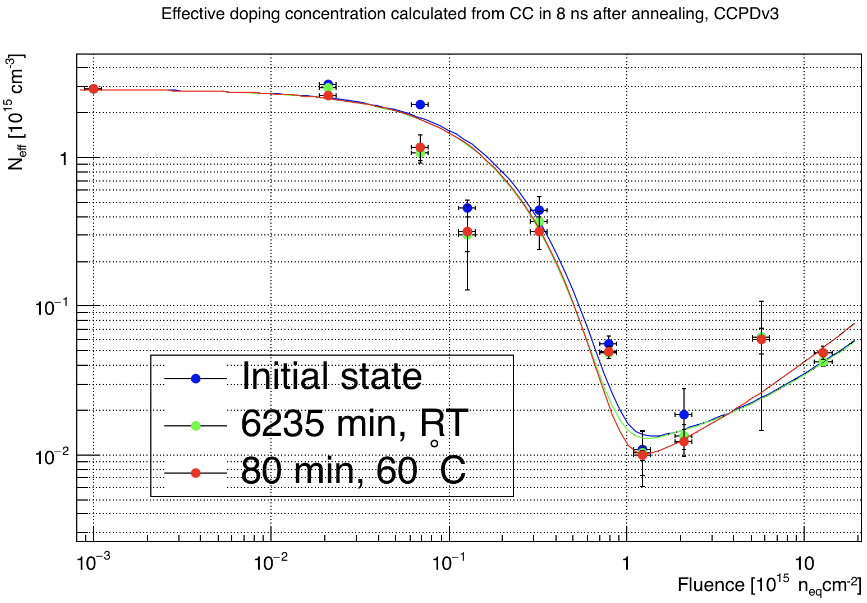

Figure 6.5.8: Effective doping concentration as a function of fluence for the CCPDv3 sample set at different annealing states.

As can be seen in figure 3.5.4, the calculated effective doping concentration only changes marginally after all samples were exposed to the equivalent time at RT. All changes are a decrease in the N_{eff} as compared to the initial state, in agreement with the Hamburg model, which states that short-term annealing increase the positive space charge, i.e. lowers the N_{eff} in our case of an initially p-doped sensor. This is usually attributed to the annealing of defects introducing negative space charge, i.e. acceptor-like defects. Between the first and second annealing step the N_{eff} appears to decline further, however, the change is even smaller and the error is on the same level of the change so an actual decline cannot be fully confirmed from just these results.

Figure 6.5.9 and 6.5.10 show the long-term annealing effects of the two samples that were irradiated to $1.22 \cdot 10^{15} n_{eq}/cm^2$ and $1.28 \cdot 10^{16} n_{eq}/cm^2$, respectively. The Hamburg model, in the form of eq. 3.5.4, used to described short and long term annealing effects in silicon sensors is fitted to the data. All parameters were left free, except N_0 which was fixed to the N_{eff} value calculated with the non-irradiated sensor.

CCPDv3_LA6 shows an initial further decrease in N_{eff} with additional annealing steps beyond 80 minutes, and then an increase again in N_{eff} with annealing beyond approximately 3000 minutes. The change in either direction is, however, limited and after the last annealing step, N_{eff} is measured to be approximately the same as prior to any annealing. Additionally, the error in a large number of the data points is on the same magnitude as the change in N_{eff} itself, giving more doubt to the actual change in N_{eff} with annealing. Despite this, the overall behaviour resembles what is found in literature, with short term annealing decreasing effective doing concentration and long term annealing increasing it again. Normally this is explained such that the short term annealing removes defects introducing negative space charge, and the long term annealing introducing such defects. However, there is also a possibility that donor-like defects are annealed away over long time, resulting in the same effect on N_{eff}. As there is limited data on this for low-resistivity Cz silicon, this cannot be said for certain to not be the case.

CCPDv3_LA9 shows a more unusual behaviour, where N_{eff} seemingly continues to decrease after approximately 4000 minutes. However, due to the lack of higher data points it cannot be ruled out that N_{eff} might increase beyond annealing times of 10000 minutes. Assuming low resistivity Cz silicon to follow the literature, i.e. having a positive g_Y, due ot the higher fluence it would be expected that N_{eff} increases more in CCPDv3_LA9 as compared to the CCPDv3_LA6 sample. As the opposite is observed here, two situations could be considered. Firstly, previously found parameters for the annealing behaviour do not apply to low resistivity Cz silicon. While it is true that not much data exists here, there seems to be relatively good consistency in literature where g_Y is in the range of $2.24 - 5.63 \cdot 10^{-2} cm^{-1}$ for both n-doped and p-doped FZ silicon and n-doped Cz silicon, undermining the validity of the results here. The second situation would simply be that the fitting method for calculating $\mathrm{N_{eff}}$ is too inaccurate. Even though it has shown to give rather good results when the depletion region is distinctively larger than the laser beam spot, due to the limited number of data points in the case of CCPDv3 sample set[10], the slope of the fit might get affected by a deviating data point. Still, if g_a and g_Y would be on the same order as previously found, despite slight $\mathrm{N_{eff}}$ variation due to fit, a larger change in $\mathrm{N_{eff}}$ than is observed in the plots below would be expected.

Sample	$\mathrm{N_{eff,0}}$ $[10^{15}\mathrm{cm}^{-3}]$	g_a $[10^{-3}\mathrm{cm}^{-1}]$	τ_a (60 °C) [min]	g_Y $[10^{-3}\mathrm{cm}^{-1}]$	τ_Y (60 °C) [min]
CCPDv3_LA6	2.87 (fixed)	1.82 ± 0.98	27.8 ± 17.1	3.24 ± 1.82	13300 ± 4700
CCPDv3_LA9	2.87 (fixed)	0.79 ± 0.11	30.3 ± 4.7	-0.24 ± 0.2	1040

Table 6.5.2: Parameters achieved from fits in figure 6.5.9 and 6.5.10. $\mathrm{N_{eff,0}}$ value calculated from non-irradiated sample. The CCPDv3_LA9 values are less reliable due to the limited data points at longer annealing times, and should not be taken as more than an indication of behaviour.

Table 6.5.2 show the fitting parameters corresponding to the short and long term annealing parameters of the fits in figures 6.5.9 and 6.5.10. Due to the nature of the large errors bars, and slight uncertainty of exact $\mathrm{N_{eff}}$ introduced with the limited number of data points in the fit, the values should be taken with a grain of salt. Still, both g_a and g_Y appears to be less than found in literature by one order of magnitude. However, as mentioned above, annealing studies on p-type Cz silicon are lacking, so these values cannot be ruled out. Additionally, recent results on high-resistivity[11] RD50-MPW2 samples annealed up to approximately 1300 minutes at 60 °C, also show little to no reverse annealing [74]. The short term annealing time parameter, τ_a, calculated here agrees well with literature.

To further investigate this, it would be suggested to include simple pad detectors on the production wafers of the HV-CMOS prototypes for cross checking validity of $\mathrm{N_{eff}}$ estimation in the low resistivity samples, as well as conducting separate annealing studies for reference. Additionally, by using the newly developed TPA-TCT technique, mentioned in more detail already in section 6.4.2, a much better measurement of the depletion

---

[10] 5V steps in the depletion depth scans.

[11] 0.5 to 2.2 kΩcm

width, and consequently the N_{eff} could be achieved for the non-irradiated prototypes. The TPA-TCT, achieving a beam spot around 1 μm [107], also makes the convolution technique redundant.

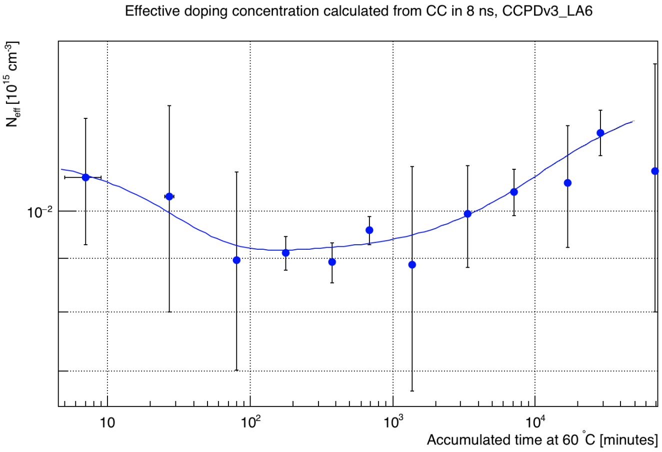

Figure 6.5.9: Effective doping concentration as a function of accumulated annealing time at 60 °C for the $1.22 \cdot 10^{15} n_{eq}/cm^2$ CCPDv3 sample.

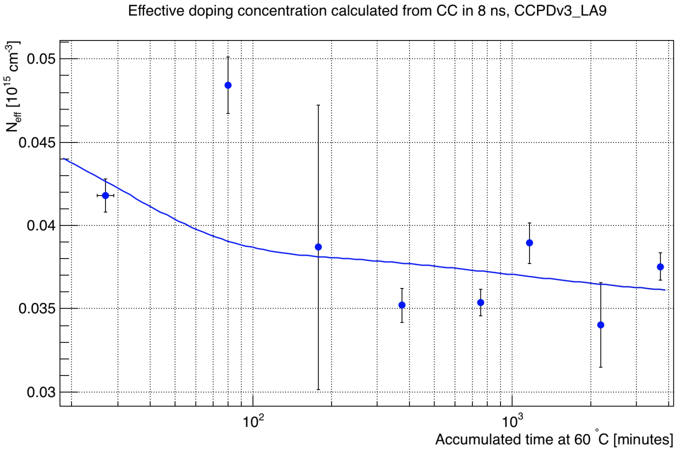

Figure 6.5.10: Effective doping concentration as a function of accumulated annealing time at 60 °C for the $1.28 \cdot 10^{16} n_{eq}/cm^2$ CCPDv3 sample.

Chapter 7

High temperature treatment

As introduced early in the thesis, due to the limited charge collection in low resistivity, high temperature annealing was theorised to be a possible method to increase the performance in the detector. By heating silicon to temperatures between 330 and 500 °C, electrically active oxygen agglomerates are formed. These introduce positive space charge, effectively acting like donors, and with high enough concentration, change the resistivity in silicon. Apart from a pure material standpoint, this effect has also been shown in MCz p-type silicon diodes, where prolonged annealing has shown space charge sign inversion [101, 41]

A first batch of four CCPDv3 samples were annealed in order to investigate this hypothesis. Early in the study, the oxygen concentration in the samples were unknown, but assumed to be $10^{18} cm^{-3}$ for calculation purposes. Normally, the oxygen concentration falls within the 5 - $10 \cdot 10^{17} cm^{-3}$ range in Cz silicon [65]. Using this value with eq. 3.2.1, appropriate annealing times were calculated. To these values, corresponding expected N_{eff} after TD introduction and change in depletion width is included. To account for the decrease in introduction rate over time, the average introduction rate over the chosen time period was calculated using $\frac{1}{b-a} \int_a^b f(t)dt$ of eq. 3.2.1. While the annealing times presented in table 7.0.1 were determined assuming an O_i of $10^{18} cm^{-3}$, the average introduction rate, as well as the expected N_{eff} and depletion widths are calculated using the measured $6.5 \cdot 10^{17} cm^{-3}$ O_i.

The new N_{eff} is simply calculated as $N_{\text{eff},0} - N_{\text{TD}}$, where the value of $N_{\text{eff},0}$ is taken from the SIMS result for the CCPDv3 and CCPDv4 samples, and from the given resistivity for the RD50-MPW1. The negative value of N_{eff} for CCPDv3_TD4 and CCPDv3_TD5

Sample name	Annealing time	Avg. introduction rate	Expected N_{eff}	Expected dw
CCPDv3_TD0	0 min	N/A	$5.59 \cdot 10^{14} cm^{-3}$	d_0
CCPDv3_TD1	25 min	$4.43 \cdot 10^{10} cm^{-3} s^{-1}$	$4.92 \cdot 10^{14} cm^{-3}$	$1.08 d_0$
CCPDv3_TD2	45 min	$4.40 \cdot 10^{10} cm^{-3} s^{-1}$	$4.40 \cdot 10^{14} cm^{-3}$	$1.13 d_0$
CCPDv3_TD3	90 min	$4.34 \cdot 10^{10} cm^{-3} s^{-1}$	$3.25 \cdot 10^{14} cm^{-3}$	$1.31 d_0$
CCPDv3_TD4	240 min	$4.13 \cdot 10^{10} cm^{-3} s^{-1}$	$-3.6 \cdot 10^{13} cm^{-3}$	$3.95 d_0$
CCPDv3_TD5	1200 min	$3.08 \cdot 10^{10} cm^{-3} s^{-1}$	$-1.66 \cdot 10^{15} cm^{-3}$	$0.58 d_0$

Table 7.0.1: Table containing annealing times and expected new effective doping concentration, calculated from $N_{\text{eff},0}$ - N_{TD}.

represents a space charge sign inversion of the bulk, i.e. it has effectively switched from a p-doped material to an n-doped material. The depletion width values were then derived using eq. 3.4.10 with the expected new N_{eff}, assuming an abrupt PN junction. As will be seen below, the results for the initial batch of four samples showed little to no change in depletion width, and a fifth sample, CCPDv3_TD5, was added, with a substantially increased annealing time.

Following the results of the first batch, where little difference was observed in the annealed samples compared to the non-annealed sample, two more batches of HV-CMOS was prepared for study. Three samples of the CCPDv4, the successor to the CCPDv3 prototype also produced by AMS on 20 Ωcm resistivity Cz silicon, and four samples of RD50-MPW1, produced by LFoundry on 10 Ωcm resistivity wafers, were annealed at 450 °C to different lengths of time. Prior to this, SIMS results on the oxygen concentration in CCPDv3 was achieved, revealing the oxygen concentration to be $6.5 \cdot 10^{17} cm^{-3}$. See Appendix A for details on the SIMS result. The CCPDv4 having the same manufacturer and resistivity is assumed here to have a similar oxygen concentration. For the RD50-MPW1 no SIMS results exist, thus the exact oxygen concentration is unknown. However, the wafer being Cz silicon, the same value as measured in the AMS sensors is used for calculating approximate TD introduction rates. Annealing times for these two new sets of samples are found in table 7.0.2.

Sample name	Annealing time	Avg. introduction rate	Expected N_{eff}	Expected dw
CCPDv4_TD1	352 min	$3.98 \cdot 10^{10} cm^{-3} s^{-1}$	$-2.82 \cdot 10^{14} cm^{-3}$	$1.41 d_0$
CCPDv4_TD2	730 min	$3.54 \cdot 10^{10} cm^{-3} s^{-1}$	$-9.91 \cdot 10^{14} cm^{-3}$	$0.75 d_0$
CCPDv4_TD3	2196 min	$2.35 \cdot 10^{10} cm^{-3} s^{-1}$	$-2.54 \cdot 10^{15} cm^{-3}$	$0.47 d_0$
RD50-MPW1_TD1	150 min	$4.25 \cdot 10^{10} cm^{-3} s^{-1}$	$9.68 \cdot 10^{14} cm^{-3}$	$1.17 d_0$
RD50-MPW1_TD2	368 min	$3.96 \cdot 10^{10} cm^{-3} s^{-1}$	$4.75 \cdot 10^{14} cm^{-3}$	$1.69 d_0$
RD50-MPW1_TD3	730 min	$3.54 \cdot 10^{10} cm^{-3} s^{-1}$	$-2.0 \cdot 10^{14} cm^{-3}$	$2.60 d_0$
RD50-MPW1_TD4	2196 min	$2.35 \cdot 10^{10} cm^{-3} s^{-1}$	$-1.75 \cdot 10^{15} cm^{-3}$	$0.88 d_0$

Table 7.0.2: Table containing annealing times and expected new effective doping concentration, for second round of thermal donor samples.

RD50-MPW1_TD1 was included to provide a short anneal time in case the oxygen concentration would be significantly higher than the value assumed when calculating.

All samples were annealed with the ceramic kiln at Lancaster University, described in section 5.1.2. As seen in that section, the temperature varies up to 10 °C from set temperature. This variation might lead a slight decrease in estimated increase in depletion width change, as the TD introduction rate decreases for temperatures higher and lower than 450 °C. The initial CCPDv3 samples were measured on the Particulars TCT setup in Lancaster University in early 2017. The CCPDv3_TD5 sample and all of the other samples were measured using the TCT+ setup in the EP-DT-DD:SSD lab.

After the wire bonding was done to connect the chips to the eTCT PCB, it was noticed that the RD50-MPW1 samples showed signs of damage to the metallisation on the detector after annealing, with the amount of damage increasing with annealing times. Prior to annealing, all samples were confirmed to visually be in good shape. Unfortunately, no microscopic pictures of this were taken after annealing was done. On the RD50-MPW1_TD4 the damage was severe enough to make any wire bonding impossible.

7.1 IV measurement

Similarly to the irradiated samples in section 6, the IV measurements here are taken during the eTCT measurements. Unfortunately, the current readings during the first measurement were corrupt, however, when monitored during the measurements the current never exceeded $10^{-2}\mu$A. As clearly seen in figure 7.1.1, the CCPDv4 samples show virtually no change in leakage current from the annealing treatment, which is expected as the TDs are shallow defects [16]. The sudden increase in current around 20V bias is attributed to the decreased resolution in the Keithley 2410 when exceeding this bias voltage, and the actual current is likely to be similar to the value before 20V. On the other hand, the RD50-MPW1 leakage current appears here to have an increase in leakage current after annealing. However, comparing this to the results achieved in section 6, leakage current of the annealed samples matches the non-irradiated sample closely and RD50-MPW1_TD0 appears to be the deviating sample. The reason for the comparatively low leakage current in this sample is unknown, but it is possibly a result of poor connectivity.

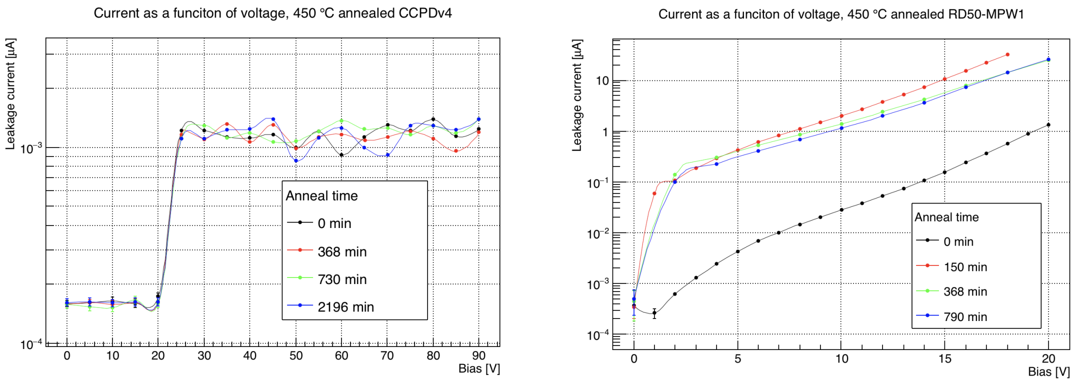

Figure 7.1.1: Leakage current as a function of bias voltage in 450 °C annealed CCPDv4 (Left) and RD50-MPW1 (Right). All measurements were done at 2±1°C.

7.2 Charge collection and estimated change in N_{eff}

The charge collection scans were performed the same way as described in chapter 6. However, the RD50-MPW1 samples slight deviate from this procedure. As described in section 4.2.1, the test structure has pads connecting to the centre pixel and outer 8 pixels. Due to limited experience with the chip at the time of measurements the depletion depth scans were done over the right side of the outer pixels as seen in figure 7.2.1 below, while also biasing through this connection instead of the bias pad. Previous measurements on the RD50-MPW1 with high resistivity[1] were done by having the outer 8 pixels in the passive test structure floating, and using the central pixel for both biasing and readout. Early measurements on the low resistivity samples showed insufficient signal to be useful for any analysis when using only the central pixel. Further, shorting the two pads and biasing from the top does not work due to difference in resistance. Thus only the outer pixels were used in the measurements below. The scan path is highlighted in figure 7.2.1.

As already mentioned little change is seen in charge collection in the CCPDv3. Figure 7.2.2 reveal a slight decrease in charge collection for the initial annealing step, and a slight increase for the subsequent steps. However, looking a the depletion width in figure 7.2.3, virtually no change in depletion width is observed, for all but the highest annealing step. Furthermore, it is probable that the measured increase in depletion width observed in

---

[1] 500 - 1900 Ωcm.

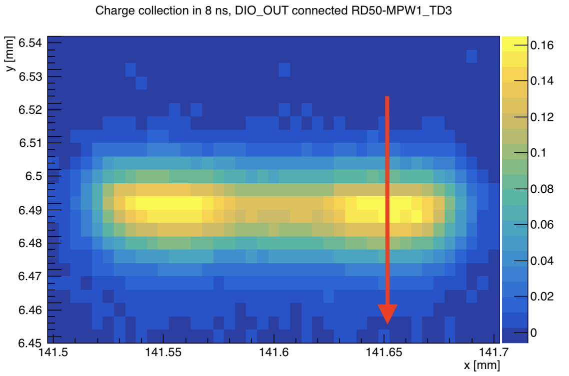

Figure 7.2.1: Charge collection area scan of RD50-MPW1, where only the outer 8 pixels of the test structure is connected. Red arrow indicates where path for charge collection scans seen in bottom plot of figure 7.2.2.

CCPDv3_TD5 is a result of bad focusing. As mentioned, this sample was measured on a different setup than the other five, and limited experience with the new setup might be the cause for this increase. Additionally, the fitted function calculates $N_{eff} \approx 4.3 \cdot 10^{15} cm^{-3}$, due to the large depletion width at low bias. This is also seen in figure 7.2.4. While this value is most likely too large, as the bad focus would inflate the depletion widths too greatly at low voltages, a type inversion cannot be ruled out. From the introduction rates seen in table 7.0.1, CCPDv3_TD5 is expected to have higher resistivity compared to the other CCPDv3 samples. On the other hand, CCPDv3_TD3 and in particular CCPDv3_TD4 would be expected to show an increase in depletion width, but as is seen no such increase is observed. It should be noted that the charge collection in the 1200 min sample has been multiplied by 65, to bring it to a similar level as the other samples. The initial low CC is due to different amplification and laser intensity between the two experimental setups. However, this multiplication was not done when calculating the depletion width and should also not affect this calculation.

Both the CCPDv4 and RD50-MPW1 measurements reveal a slight increase in charge collection after annealing. However, figure 7.2.3 shows that the calculated depletion width is slightly smaller in every annealed sample, for both of these sample sets. The change exhibited in the CCPDv4 sample set is small enough to be considered a result of variation in surface roughness. If the oxygen concentration is similar to the CCPDv3 samples, the depletion width in the 352 minute sample is expected to be approximately 40% larger than the non-annealed sample, but this is clearly not the case. It is possible to imagine a different introduction rate to the assumed one in the beginning of this chapter. The oxygen concentration in normal Cz silicon is known to vary depending on radial position, and is greatly affected by the rotation speed during production [111].

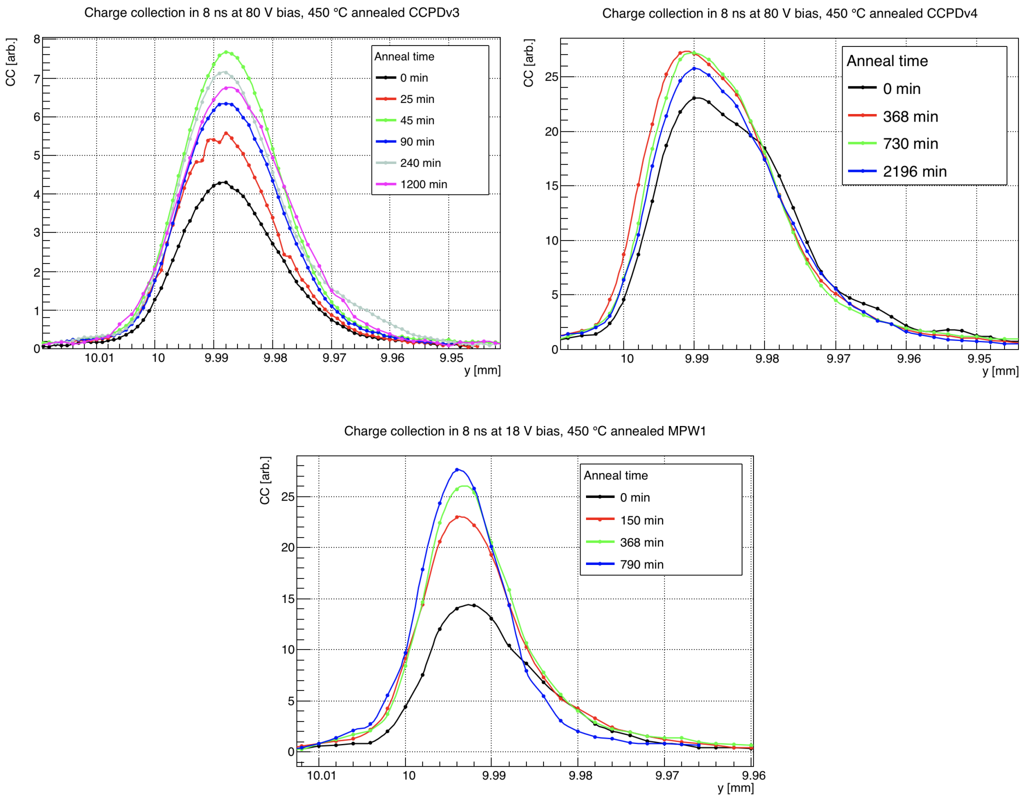

Figure 7.2.2: Charge collection along sensor depth in 450 °C annealed CCPDv3 (top left), CCPDv4 (top right), and RD50-MPW1 (bottom). Sensor surface at approximately y = 10, with decreasing y moving into the sensor bulk.

Some high oxygen concentration, industrial level Cz silicon ingots have a variation up to 15% from centre to the edges of the wafer [77], meanwhile growth methods applying a magnetic field can have variations as low as $1 - 2\%$ [101]. Unfortunately, foundries rarely reveal information on this part, and a higher oxygen concentration compared to the CCPDv3 is possible. Additionally, if the oxygen diffusivity is higher than used during the calculations, the introduction rate could be underestimated. As mentioned in section 3.2, an increased presence of oxygen dimers and trimers can cause higher oxygen diffusivity, which would lead to higher introduction rates [81]. However, the case of a higher introduction rate, and consequently a type inversion already after the first annealing step in the MPW1 samples, is ruled out as the depleted region clearly is growing in the interface between the deep n-well and the bulk.

However, while no type inversion has taken place, significant reduction in diffusing charge carriers can be seen in figure 7.2.7 between then non-annealed and the longest annealed sample, suggesting introduction of defects acting as recombination centres after the annealing. This decrease in diffusion contribution to CC is not seen in CCPDv3 (figure 7.2.5), and only slightly hinted at in the CCPDv4 (figure 7.2.6) samples, with the most

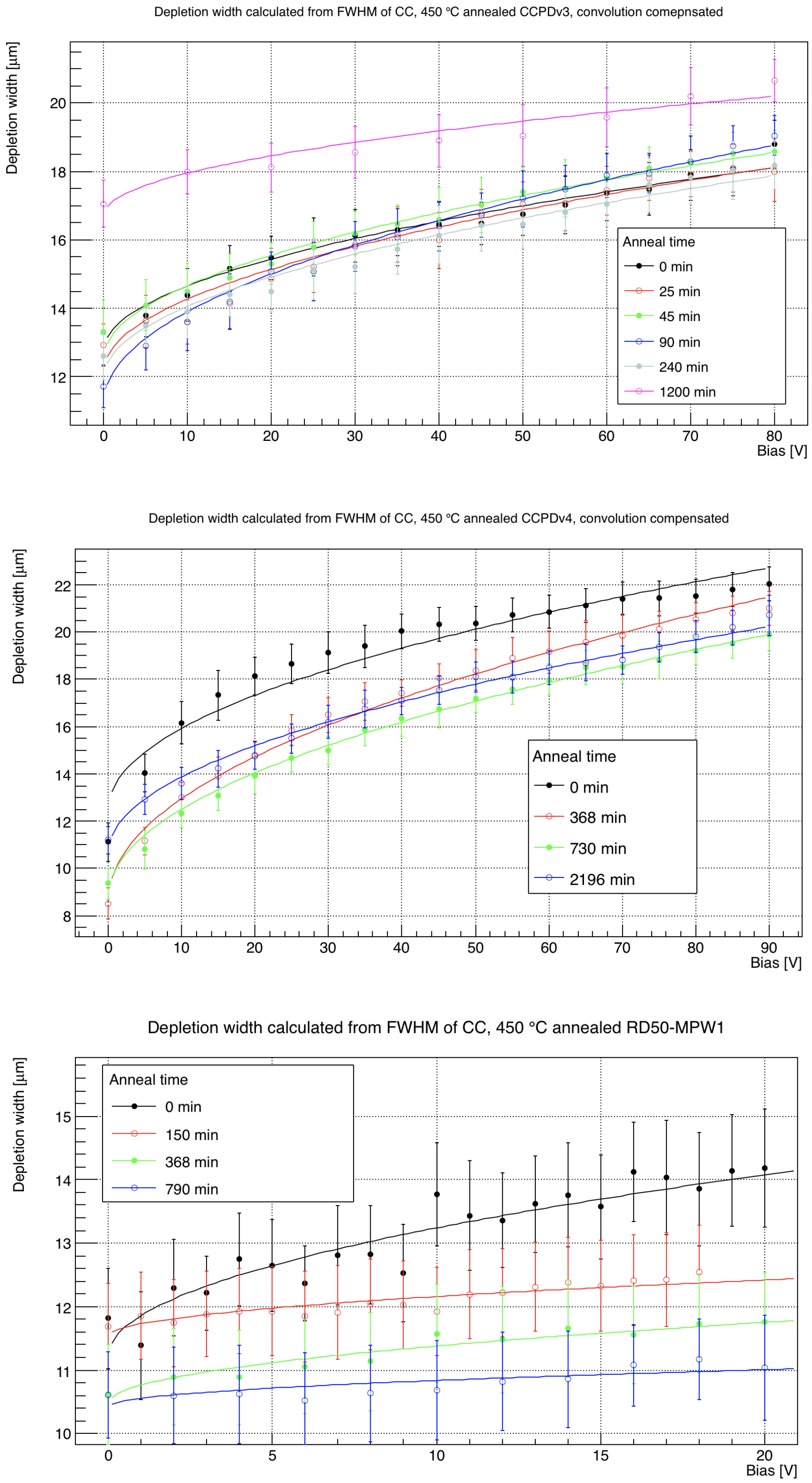

Figure 7.2.3: Depletion width as a function of bias voltage in CCPDv3 (top), CCPDv4 (middle), and RD50-MPW1 (bottom). Laser beam convolution was taken into account in the CCPDv3 and CCDPv4 sample sets. Due to the limited signal, no subtraction of simulated convolution was applied in the RD50-MPW1 samples.

annealed sample showing a slight flattening of the CC curve as a function of integration time at peak CC. This discrepancy in diffusion contribution to CC between CCPDv4

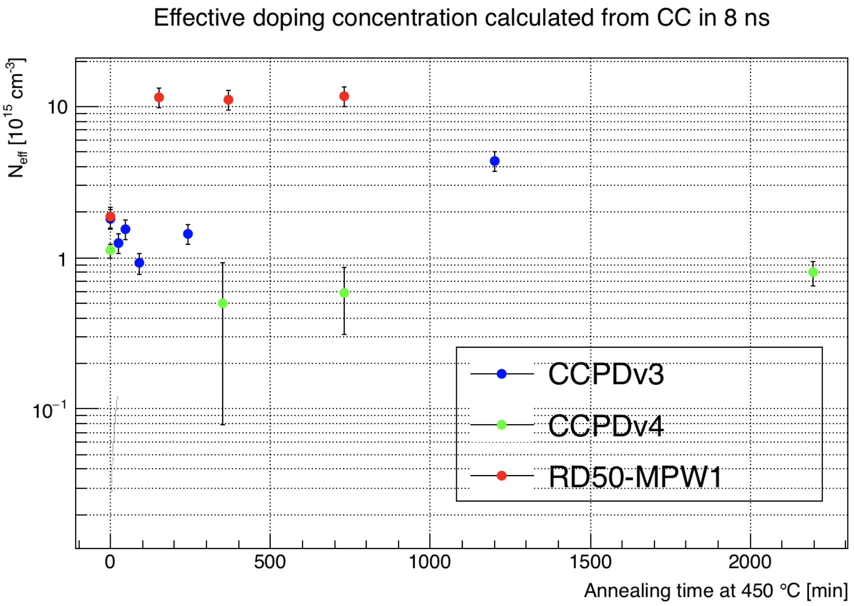

Figure 7.2.4: N_{eff} as a function of annealing time at 450 °C, calculated by fitting equation 5.5.2 to the calculated depletion widths in 7.2.3

and RD50-MPW1 suggests significantly discrepency in bulk material between the two prototypes. The increase in leakage current and decrease diffusing charge carriers, without any apparent type inversion in MPW1 is peculiar and further studies would need to be carried out to understand this. Firstly, a SIMS measurement of Oxygen and Boron concentration would be useful to estimate TD introduction rates. Secondly, similarly as suggested in section 6.5.2, to get a better understanding the concentration of introduced TDs DLTS and TSC measurements would be of interest for future studies, both of which can measure the TDs directly.

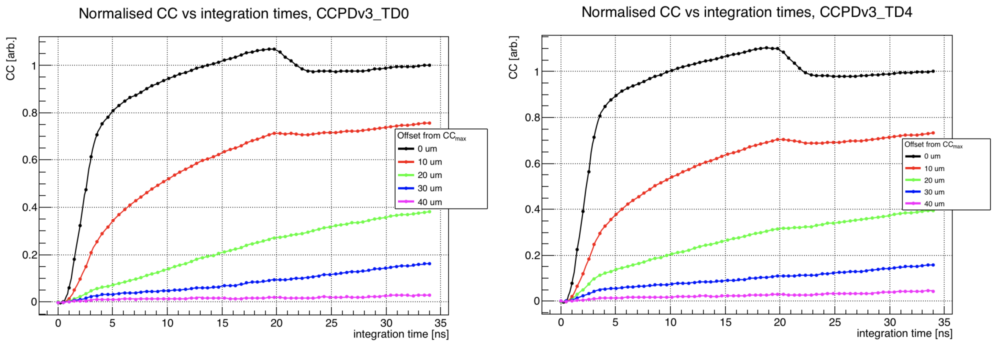

Figure 7.2.5: Normalised CC as a function of integral time, CCPDv3. *Left*: Non-annealed CCPDv3. *Right*: CCPDv3 annealed at 450 °C for 240 minutes. The dip at 20 ns corresponds to signal reflection due to impedance mismatch.

More studies would need to be conducted to determine whether thermal donor intro-

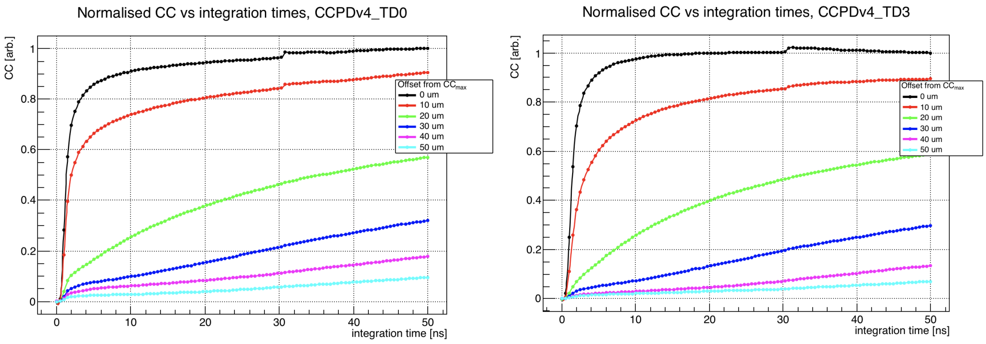

Figure 7.2.6: Normalised CC as a function of integral time, CCPDv4. *Left*: Non-annealed CCPDv4. *Right*: CCPDv4 annealed at 450 °C for 2196 minutes.

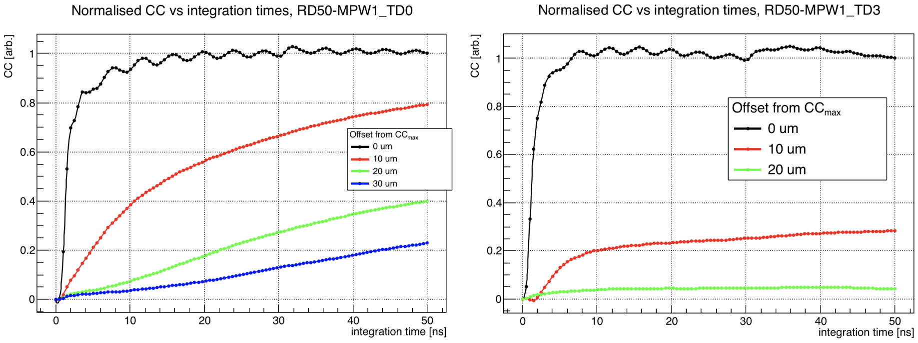

Figure 7.2.7: Normalised CC as a function of integral time, RD50-MPW1. *Left*: Non-annealed RD50-MPW1. *Right*: RD50-MPW1 annealed at 450 °C for 2196 minutes.

duction could be used as a viable method for post-processing alteration of resistivity in HV-CMOS. However, the findings presented above point out a few clear difficulties in accurately manipulating the N_{eff} to a specific value. Firstly, the oxygen concentration has to be determined to a high accuracy, not only in a sample from the same set, but in the specific sample used due to radial difference of concentration on Cz wafers. Even for CCPDv3 (and most probably CCPDv4) where the oxygen concentration is known, the measured depletion widths also show large deviation from the theorised values. As mentioned, this could be due to difference in oxygen concentration along radial wafer position during production of the chip. However, this could also be result of deviating oxygen diffusivity as a result of formation of oxygen dimers and trimers due to elevated temperatures during production. Generally, foundries do not disclose their manufacturing processes in detail, practically eliminating the chance of knowing the heat treatment history of HV-CMOS chips produced at a commercial foundry. It might be possible to still achieve reasonable results even if oxygen diffusivity estimates are slightly wrong but the oxygen concentration is known, in case high resistivity samples are used. This is due to the fact that high resistivity samples require very short annealing times to reach a desired N_{eff} lowering the effect of wrongly estimated parameters. With lower resistivity samples require longer annealing times, any deviation in values used to calculate the resulting N_{eff} will affect the end result in greater scale. Due to this reason, it is concluded that TD introduction as a method of engineering the N_{eff} in low resistivity HV-CMOS chips is not viable.

Chapter 8

Conclusion

The work conducted in this thesis has been done with the aim of investigating the viability of silicon sensors based on the HV-CMOS technology using low resistivity substrate as potential detectors in future large HEP experiments. Many of these experiments will impose high requirements on the tracking performance, requiring high spatial granularity and fast readout speeds. Sensors using HV-CMOS technology has been shown to perform competitively, and superiorly in certain aspects, compared to conventional silicon-based pixel detectors. Using a fully monolithic CMOS pixel detector has the potential to reduce the production cost significantly. Furthermore, using active pixels, there is potential to eliminate the need to use special silicon wafers with high resistivity, and instead use the standard process with standard resistivity wafers, allowing for productions on shared MPWs and cost reductions.

Four different HV-CMOS prototypes produced on standard resistivity wafers were used in this study. Two prototypes, the CCPDv3 and CCPDv4, were produced by AMS using their aH18 CMOS technology on their 20 Ωcm standard substrate wafers. The two other samples were the RD50-MPW1 and RD50-MPW2 developed within the framework of RD50, both produced by LFoundry using their 150 nm High-Voltage CMOS process on their 10 Ωcm standard resistivity wafer.

The CCPDv3, RD50-MPW1, and RD50-MPW2 were used to investigate the radiation tolerance of standard resistivity HV-CMOS. In order to do this, the CCPDv3 were irradiated at LANSCE with 800 MeV protons up to an equivalent fluence of $1.28 \cdot 10^{16} n_{eq}/cm^2$. The RD50-MPW1 chips were irradiated in the Bern Cyclotron Proton Irradiation Facility with 18 MeV protons up to $5 \cdot 10^{14} n_{eq}/cm^2$. Lastly, the RD50-

MPW2 chips were irradiated in the TRIGA Mk II nuclear reactor at IJS with neutrons to an equivalent fluence of $2 \cdot 10^{15} n_{eq}/cm^2$.

Both proton-irradiated sample sets show a significant increase in charge collection at higher fluences. The 18 MeV irradiated RD50-MPW1 has 6 times increase in integrated charge collection at $5 \cdot 10^{14} n_{eq}/cm^2$. The 800 MeV CCPDv3 set, also show a large increase in charge collection above $7 \cdot 10^{14} n_{eq}/cm^2$, and the charge collection and signal strength is significantly higher even after the highest fluence point, $1.28 \cdot 10^{16} n_{eq}/cm^2$, compared to the non-irradiated sample. From a radiation tolerance aspect, these chips show good potential for future high energy experiments like the HL-HLC and possibly as a candidate for the pixel detector in the FCC. At around $10^{15} n_{eq}/cm^2$ fluence, the low-resistivity HV-CMOS sensors appear to perform better than the their high resistivity counterparts, attributed to the fact of delayed complete acceptor removal in low resistivity silicon. The major limitation of the low resistivity chips, in addition to the expected low charge collection in the non-irradiated case, is a decrease in charge collection in the 10^{13} to $10^{14} n_{eq}/cm^2$ range. It is seen in the CCPDv3 sample were CC falls to just under 60% of CC in the non-irradiated sample after $6.83 \cdot 10^{13} n_{eq}/cm^2$ and to around 70% after $1 \cdot 10^{14} n_{eq}/cm^2$ in the RD50-MPW1. Previous investigation with limited fluence points found 18 MeV-proton-irradiated CCPDv4 to have a significant reduction in hit efficiency after receiving $1.3 \cdot 10^{14} n_{eq}/cm^2$ fluence [14]. The findings here then suggests the hit efficiency is possibly even lower at lower fluence. This would severely limit the effectiveness of these detectors in a radiation environment where fluence in this range is expected. This conclusion is further emphasised by the results of the neutron irradiated RD50-MPW2, where a large decrease in CC is seen with increasing fluence, even at fluences where the depletion width is visibly increasing.

These findings also diminish the prospects of using irradiation as a post processing method for increasing the efficiency of the low resistivity HV-CMOS detectors. While proton irradiation, in particular in the 18 MeV range, shows a large increase in depletion width and collected charge, the costs outweigh the costs of using non-standard resistivity while simultaneously imposing a larger leakage current. On the other hand, neutron irradiation, while being a cheaper alternative, is seen to reduce the charge collection in low-resistivity RD50-MPW2 making them perform worse.

Initial measurements of the leakage current show increasing leakage current with increased fluence, in all samples apart from the RD50-MPW1, similar to expectation.

However, the RD50-MPW1 prototypes show exponential increase with leakage current before any irradiation, and decreasing leakage current with fluence. The leakage current before irradiation was partly explained by a conductive material added as a surface structure by LFoundry. The decrease following irradiation is hypthetically introduced defects acting as recombination centres between these structures. However, further,detailed IV studies at multiple temperatures should be carried out to better understand the behaviour.

In order to calculate and evaluate the N_{eff}, a new method combining the compensation for laser and depletion width convolution and the fit of eq. 5.5.2 was utilised. Prior to this study, the compensation for the convolution had been used once before [31], but never in conjunction with the method of extracting N_{eff} from fitting eq. 5.5.2. While this method was found to produce N_{eff} values closer to what is expected from the given resistivities compared to not taking the convolution into account, in future studies it is recommended that this method should be more rigorously calibrated using low resistivity planar diodes with well known depletion regions. If calibrated further, it would be recommended to take the convolution into account when evaluating the N_{eff}, in samples with depletion widths within 3 times that of the laser waist. However, with the emergence of the TPA-TCT [107], future investigations of low resistivity detectors, or detectors with small features of interest, would greatly benefit from using a TPA-TCT setup over conventional eTCT.

Furthermore, it is found that the change in N_{eff} is described accurately by the acceptor removal model[1]. The low resistivity HV-CMOS sensors follow the trend of smaller acceptor removal constant, *c*, for larger initial doping concentration, as is seen in various detector technologies using silicon in figure 6.5.7. Interestingly, the RD50-MPW1 sample set irradiated with 18 MeV protons appears to suggest that low energy proton irradiation yields a higher *c*. Due to the limited data in the energy region, it cannot be excluded that this high value is a result of some effect exclusive to the RD50-MPW1 prototype, as it has only been studied by neutron irradiation before. Still it could be of interest to further study the acceptor removal effect as a function of proton energy, as lower energy appears to induce greater acceptor removal.

Future work on irradiation studies of low resistivity HV-CMOS should include DLTS and TSC measurements. This would allow measurements of the introduction rate of

---

[1] Eq. 3.4.11

certain defects. Therefore, it would be recommended to include simple planar diodes in the prototype wafer, as experiment showed that the depleted volume of the test structure is too small to yield any significant signals with either of the techniques.

In addition to the irradiation campaigns, thermal donor introduction was considered as a potential post-processing method to increase the resistivity of standard substrate HV-CMOS. This had been done before in high-resistivity p-type MCz silicon diodes, where after an initial decrease in N_{eff} the diode underwent space charge sign inversion due to significantly high concentrations of thermal donors [41, 101]. Three HV-CMOS sample sets were annealed at 450 °C at increasing time intervals to investigate the behaviour. The first and second set, using CCPDv3 and CCPDv4 chips respectively, showed little to no sign of change following exposure to 450 °C. Oxygen concentration measurement was done on a separate CCPDv3, revealing the concentration to be approximately $6.91 \cdot 10^{17}$ cm^{-3}. Following the introduction rate postulated by Wada's findings in [106], it is suggested that even a slight deviation from measured oxygen concentration results in large deviation in introduced thermal donors. The third set of samples used the RD50-MPW1. Unfortunately no measurement of oxygen concentration was possible prior to annealing and thus annealing times were calculated from an oxygen concentration assumed to be similar to the CCPDv3 measurement. Depletion widths in the three annealed samples were found to be decreasing with increased annealing time, however, no type inversion had taken place here either as the depletion region was still observed growing from the deep n-well to bulk interface. Still, diffusion contribution to the signal was gradually reduced with increasing annealing times, suggesting introduction of defects acting as recombination centres. To better understand the apparent lack of TD introduction, similarly to the irradiation, future work should include measurements done with DLTS and TSC to verify the presence and concentration of introduced TD.

While further investigation is of interest, ultimately, the TD introduction is not seen as a viable method for increasing the active region in HV-CMOS particle detectors. This is mainly due to two reasons. With oxygen concentration varying radially in the silicon wafer, measurements would be required for each individual chip. Secondly, commercial foundries are highly protective of their production methods, making it hard to determine the annealing history of the chips, and thus estimating the oxygen diffusivity. While measuring the oxygen concentration in each chip is challenging, it is possible. However, the uncertain diffusivity makes it virtually impossible.

However, while there is a loss in CC at lower fluences making the standard substrate HV-CMOS a non-optimal candidate in a HEP tracker that expects extended times around these fluences, it is deemed a good alternative to high resistivity versions for quick prototyping where it is inconvenient to use a non-standard substrate. This could be in the case of a small scale prototype sharing an MPW with other projects making the substrate resistivity inflexible, or budget constraints where the non-standard substrate option for the prototype would incur additional costs.

Appendices

Appendix A

SIMS

A SIMS measurement was carried out on one CCPDv3 sample at ITE[1], using a CAMECA IMS 6F SIMS device. The device uses a primary ion beam and continuous sputtering SIMS was done to achieve a depth profile of concentrations for O, C, and B. The sputtering was done on the backside of the chip, as it is unprocessed and gives direct access to the silicon bulk. The exact measured concentrations are found in figure A.0.1, and the average values in table A.0.1 below. The measured carbon and oxygen concentrations are typical for Cz silicon. The measured boron concentration is slightly lower than expected for 20 Ωcm, $6.30{\cdot}10^{14}$ cm^{-3}. The measured concentration translates to approximately 24 Ωcm.

O [cm^{-3}]	C [cm^{-3}]	B [cm^{-3}]
$6.91 \pm 1.05 \cdot 10^{17}$	$2.10 \pm 0.44 \cdot 10^{16}$	$5.59 \pm 1.19 \cdot 10^{14}$

Table A.0.1: Table containing avergae values of measured concentrations along the depth in the CCPDv3 chip. Averages are excluding the first 5μm of measured values.

---

[1] Institute of Electron Technology, Poland

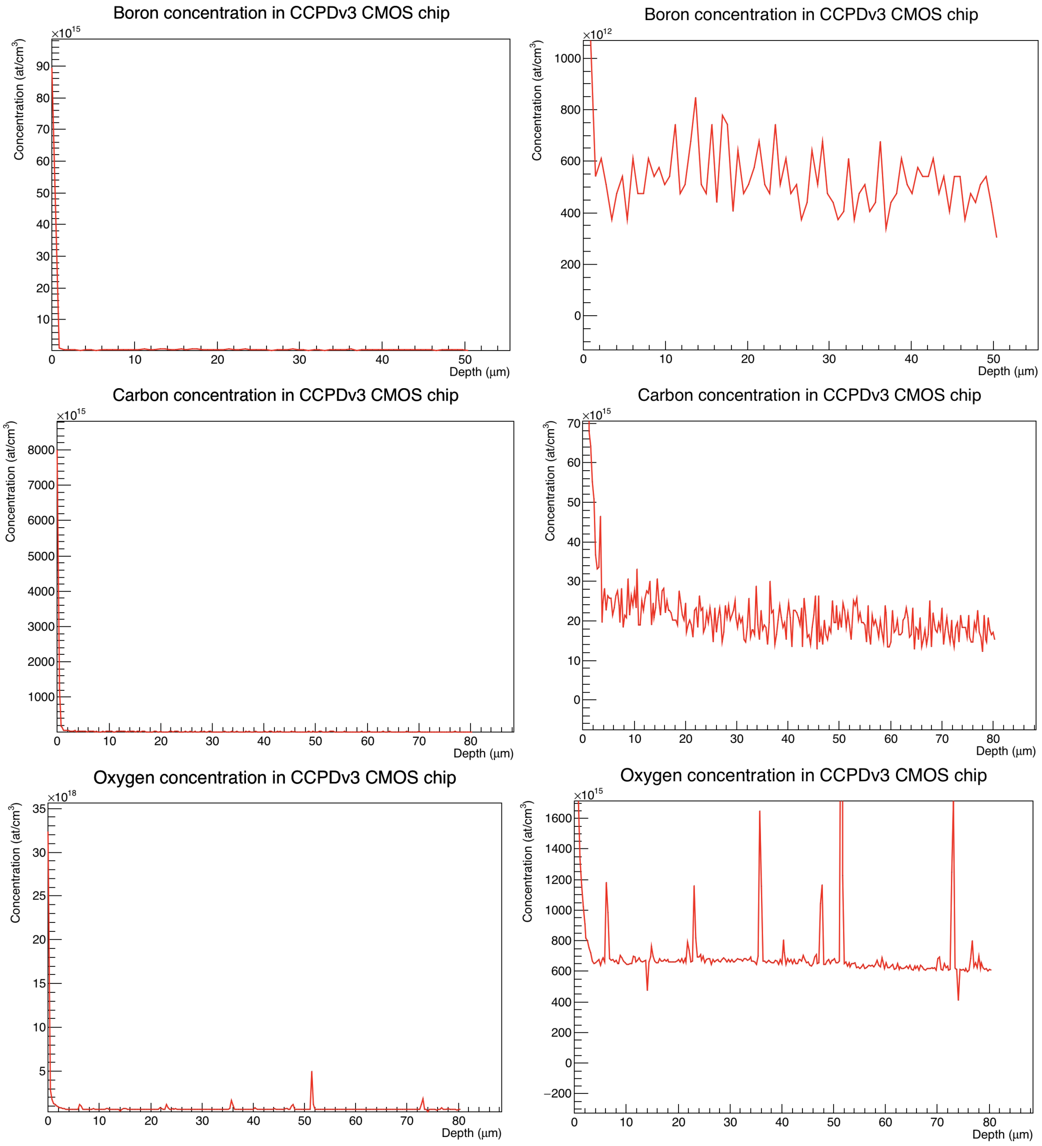

Boron concentration in CCPDv3 CMOS chip

Boron concentration in CCPDv3 CMOS chip

Carbon concentration in CCPDv3 CMOS chip

Carbon concentration in CCPDv3 CMOS chip

Oxygen concentration in CCPDv3 CMOS chip

Oxygen concentration in CCPDv3 CMOS chip

Figure A.0.1: Concentration of O, C, and B in the CCPDv3 chip, measured with SIMS.

Appendix B

$\mathrm{N}_{\mathrm{eff}}$ calculation comparisons

As explained in section 5.5.3, the method for calculating $\mathrm{N}_{\mathrm{eff}}$ is an extension to a previous method, and has not been tested before. This appendix aims at showing the suitability of this method for low resistivity HV-CMOS. The filled dots in the figures B.0.1 through B.0.3, are the same values as used in the results section 6.5.2. The hollow dots are calculated by fitting eq. 5.5.2 directly to the FWHM calculated from the CC profile along sensor depth. The fit is still limited to FWHMs lower than the 75% of junction width.The fitted eq. 6.5.1 only serves as an eye guide and the fitting parameters are omitted here.

It is seen that without taking the convolution into account, the $\mathrm{N}_{\mathrm{eff}}$ is greatly overestimated in all non- or lowly irradiated samples. Non-irradiated $\mathrm{N}_{\mathrm{eff}}$ values found are between 3.7 to $8.6 \cdot 10^{15} cm^{-3}$, much higher than initial doping concentrations estimated from resistivity, 0.64 to $1.35 \cdot 10^{15} cm^{-3}$. The non-irradiated CCPDv3 shows the smallest difference going from 4.1 to $2.9 \cdot 10^{15} cm^{-3}$ after taking the convolution into account. While it is an improvement, it is still slightly over 4 times larger than the expected value, $0.67 \cdot 10^{15} cm^{-3}$. This overestimation is potentially due to inflated charge collection at low bias resulting from the geometrical feature of the deep n-well. The high fluence samples show no difference, as is expected when depletion width is much larger than beam width.

The RD50-MPW1 and RD50-MPW2 samples show a larger change in $\mathrm{N}_{\mathrm{eff}}$, where RD50-MPW1 goes from $6.8 \cdot 10^{15} cm^{-3}$ to $2.6 \cdot 10^{15} cm^{-3}$, and RD50-MPW2, 3 μm structure goes from $8.5 \cdot 10^{15} cm^{-3}$ to $2.5 \cdot 10^{15} cm^{-3}$, after taking the convolution into account. This shows a significant improvement, however, it should be noted that the $\mathrm{N}_{\mathrm{eff}}$ is still estimated to be just short of twice the value of what is expected $1.35 \cdot 10^{15} cm^{-3}$. However, due to the lack of SIMS measurements on either of these chips it cannot be ruled out not to be accurate. On the other hand, the RD50-MPW2, 8 μm structure, with its higher maximum bias show a change from $3.7 \cdot 10^{15} cm^{-3}$ to $1.13 \cdot 10^{15} cm^{-3}$, which equals 12 Ωcm, close to the stated 10 Ωcm.

As expected the highly irradiated samples that show a significant increase in depletion width show little change between the two methods, as the difference between convolution and expected depletion width becomes negligible when the depletion region is greater than 30 μm, considering the beam widths around 10 - 12 μm.

Evidently, taking the convolution into account gives a more accurate estimate of the N_{eff}, but it is still relatively inaccurate in some cases. A big factor might be the overestimation of depletion width at low biases due to the geometrical structure of the deep n-well, causing the fit to underestimate the $\omega_{dep} \propto \sqrt{V}$ relationship. Higher accuracy can be achieved using a TPA-TCT[1], setup which can reach a beam waist less than 2 μm [107].

---

[1] Twp Photon Absorption TCT

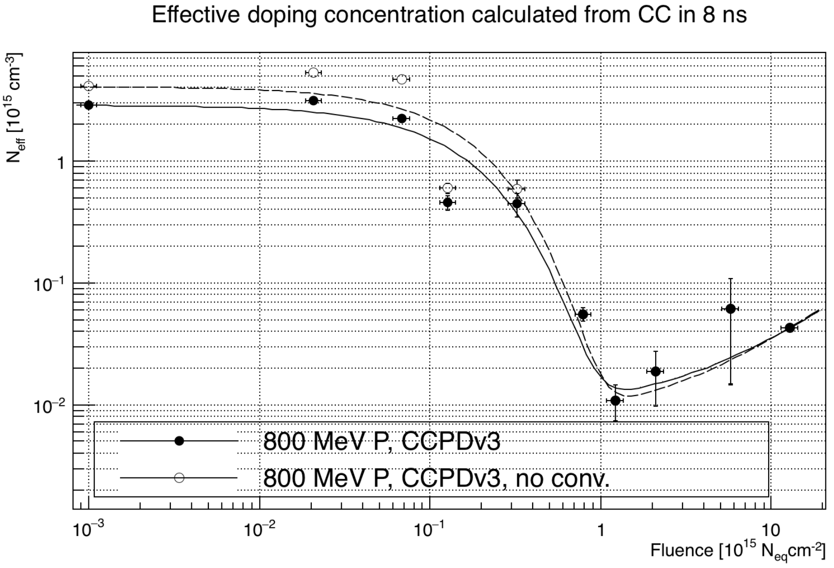

Figure B.0.1: N_{eff} as a function of fluence, CCPDv3 sample set. No conv. in legend means that convolution was not taken into account when calculating N_{eff}. The other entry is the method use in the results chapter, and explained in section 5.5.3.

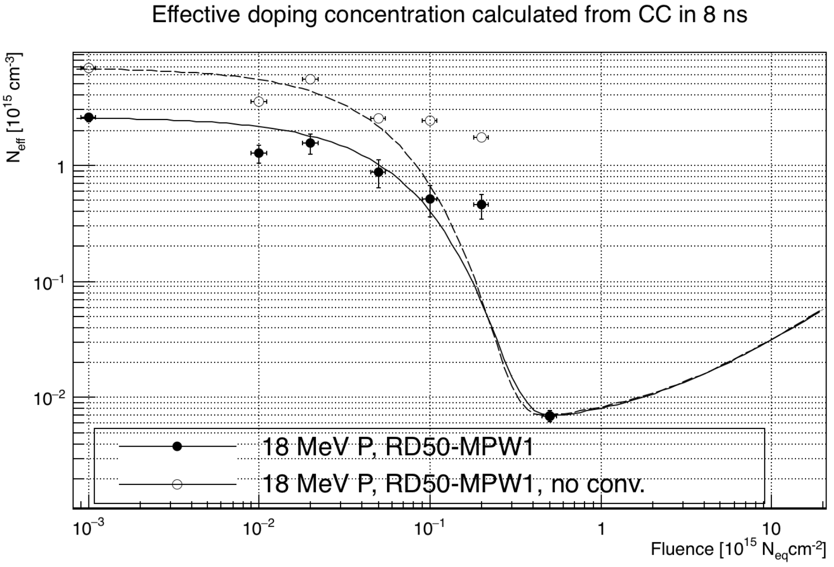

Figure B.0.2: N_{eff} as a function of fluence, RD50-MPW1 sample set. No conv. in legend means that convolution was not taken into account when calculating N_{eff}. The other entry is the method use in the results chapter, and explained in section 5.5.3.

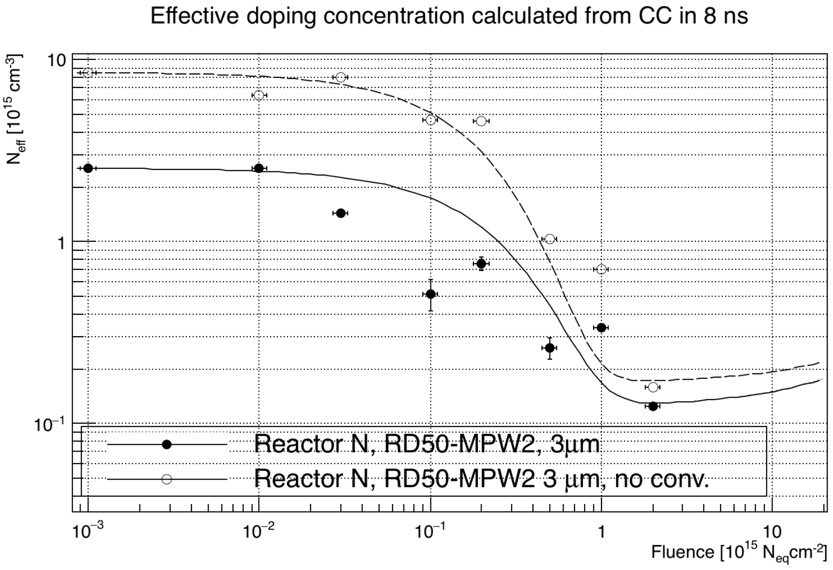

Figure B.0.3: N_{eff} as a function of fluence, RD50-MPW2, 3 μm sample set. No conv. in legend means that convolution was not taken into account when calculating N_{eff}. The other entry is the method use in the results chapter, and explained in section 5.5.3.

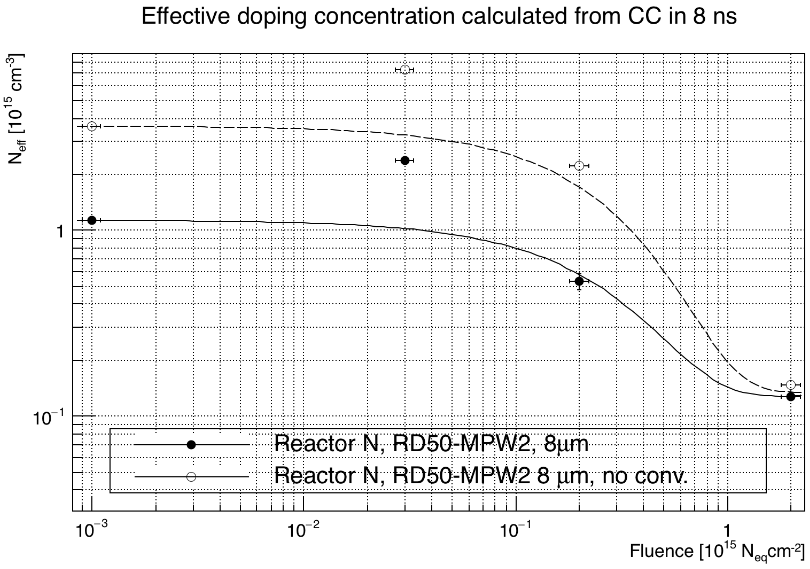

Figure B.0.4: N_{eff} as a function of fluence, RD50-MPW2, 8 μm sample set. No conv. in legend means that convolution was not taken into account when calculating N_{eff}. The other entry is the method use in the results chapter, and explained in section 5.5.3.

Bibliography

[1] G. Aad et al. “Observation of a new particle in the search for the Standard Model Higgs boson with the ATLAS detector at the LHC”. In: *Physics Letters B* 716 (Sept. 2012).

[2] Pertti A Aarnio et al. “Damage observed in silicon diodes after low energy pion irradiation”. In: *Nuclear Instruments and Methods in Physics Research Section A: Accelerators, Spectrometers, Detectors and Associated Equipment* 360.3 (1995), pp. 521–531.

[3] A Affolder et al. “Charge collection studies in irradiated HV-CMOS particle detectors”. In: *Journal of instrumentation* 11.04 (2016), P04007.

[4] I. mandic et al. “First measurements with silicon detectors irradiated above $3e17n/cm^2$”. In: 32nd RD50 workshop. June 2018.

[5] P Allport et al. “Experimental determination of proton hardness factors at several irradiation facilities”. In: *Journal of Instrumentation* 14.12 (2019), P12004.

[6] *ATLAS Inner Detector Technical design report.* 1997.

[7] *ATLAS Insertable B-Layer Techincal Design Report.* 2010.

[8] *ATLAS Technical design report.* 1999.

[9] Martin Auger et al. “Accelerator and detector physics at the Bern medical cyclotron and its beam transport line”. In: *Nukleonika* 61.1 (2016), pp. 11–14.

[10] JF Bak et al. “Large departures from Landau distributions for high-energy particles traversing thin Si and Ge targets”. In: *Nuclear Physics B* 288 (1987), pp. 681–716.

[11] SJ Bates et al. “Pion-induced damage in silicon detectors”. In: *Nuclear Instruments and Methods in Physics Research Section A: Accelerators, Spectrometers, Detectors and Associated Equipment* 379.1 (1996), pp. 116–123.

[12] Ties Behnke et al. “The international linear collider technical design report-volume 1: Executive summary”. In: *arXiv preprint arXiv:1306.6327* (2013).

[13] Mathieu Benoit et al. “Results of the 2015 testbeam of a 180 nm AMS High-Voltage CMOS sensor prototype”. In: *Journal of Instrumentation* 11.07 (2016), P07019.

[14] M Benoit et al. “Testbeam results of irradiated ams H18 HV-CMOS pixel sensor prototypes”. In: *Journal of instrumentation* 13.02 (2018), P02011.

[15] Hans Bichsel. “Straggling in thin silicon detectors”. In: *Reviews of Modern Physics* 60.3 (1988), p. 663.

[16] M Bruzzi et al. “Thermal donor generation in Czochralski silicon particle detectors”. In: *Nuclear Instruments and Methods in Physics Research Section A: Accelerators, Spectrometers, Detectors and Associated Equipment* 568.1 (2006), pp. 56–60.

[17] M Buckland. “Analysis and simulation of HV-CMOS assemblies for the CLIC vertex detector”. In: Technology and Instrumentation in Particle Physics 2017. May 2017.

[18] G Casse et al. “Comparison of charge collection efficiency of segmented silicon detectors made with FZ and MCz p-type silicon substrates”. In: *Nuclear Instruments and Methods in Physics Research Section A: Accelerators, Spectrometers, Detectors and Associated Equipment* 591.1 (2008), pp. 178–180.

[19] Emanuele Cavallaro et al. “Studies of irradiated AMS H35 CMOS detectors for the ATLAS tracker upgrade”. In: *Journal of Instrumentation* 12.01 (2017), p. C01074.

[20] *CERN Document Server.*

[21] Robert E Chaney and Charles J Varker. “The dissolution of fused silica in molten silicon”. In: *Journal of Crystal Growth* 33.1 (1976), pp. 188–190.

[22] A Chilingarov. “Temperature dependence of the current generated in Si bulk”. In: *Journal of instrumentation* 8.10 (2013), P10003.

[23] V Cindro. “Transnational acces to TRIGA Mark II reactor”. In: AIDA meeting. 2018.

[24] G Claus et al. “Particle tracking using CMOS monolithic active pixel sensor”. In: *Nuclear Instruments and Methods in Physics Research Section A: Accelerators, Spectrometers, Detectors and Associated Equipment* 465.1 (2001), pp. 120–124.

[25] RD50 CMOS collaboration. *Internal collaboration meeting.* 2020.

[26] The ATLAS collaboration. “Modelling radiation damage to pixel sensors in the ATLAS detector”. In: *Journal of Instrumentation* 14 (2019).

[27] F. Derue. “B-physics overview in ATLAS”. In: *Nuclear Physics B - Proceedings Supplements* 174 (2007), pp. 159–164.

[28] P Dias de Almeida et al. “Characterization of acceptor removal in silicon pad diodes irradiated by protons and neutrons”. In: 32nd RD50 Workshop. June 2018.

[29] W Dulinski et al. *Diamond detectors for future particle physics experiments.* Tech. rep. 1994.

[30] Armin Fehr. “The Bern Cyclotron Proton Irradiation Facility”. In: Joint Annual Meeting of SPS and ÖPG. 2017.

[31] M Fernández García, M Moll, and D Muenstermann. “Radiation hardness studies of proton and neutron irradiated HVCMOS”. In: 27rth RD50 Workshop. 2015.

[32] M Fernández García et al. “Radiation hardness studies of neutron irradiated CMOS sensors fabricated in the ams H18 high voltage process”. In: *Journal of Instrumentation* 11.02 (2016), P02016.

[33] Matthew Franks. *Internal RD50 Design Meeting.* 2018.

[34] M Franks et al. “Design optimisation of depleted CMOS detectors using TCAD simulations within the CERN-RD50 collaboration”. In: 14th Trento Workshop. 2019.

[35] Markus Friedl. “The CMS silicon strip tracker and its electronic readout”. PhD thesis. Vienna, Tech. U., 2001.

[36] CS Fuller and RA Logan. “Effect of heat treatment upon the electrical properties of silicon crystals”. In: *Journal of Applied Physics* 28.12 (1957), pp. 1427–1436.

[37] M Garcia-Sciveres et al. “The FE-I4 pixel readout integrated circuit”. In: *Nuclear Instruments and Methods in Physics Research Section A: Accelerators, Spectrometers, Detectors and Associated Equipment* 636.1 (2011), S155–S159.

[38] E Gatti, G Padovini, and V Radeka. “Signal evaluation in multielectrode radiation detectors by means of a time dependent weighting vector”. In: *Nuclear Instruments and Methods in Physics Research* 193.3 (1982), pp. 651–653.

[39] Martin A Green. “Self-consistent optical parameters of intrinsic silicon at 300 K including temperature coefficients”. In: *Solar Energy Materials and Solar Cells* 92.11 (2008), pp. 1305–1310.

[40] Marius Grundmann. *Physics of semiconductors.* Vol. 11. Springer, 2010.

[41] Jaakko Härkönen et al. “Proton irradiation results of p+/n-/n+ Cz-Si detectors processed on p-type boron-doped substrates with thermal donor-induced space charge sign inversion”. In: *Nuclear Instruments and Methods in Physics*

Research Section A: Accelerators, Spectrometers, Detectors and Associated Equipment 552.1-2 (2005), pp. 43–48.

[42] Frank Hartmann and Jochen Kaminski. “Advances in tracking detectors”. In: *Annual Review of Nuclear and Particle Science* 61 (2011), pp. 197–221.

[43] A Henry et al. “”New donors” in silicon: A quantum well controlled conductivity”. In: *Applied physics letters* 49.19 (1986), pp. 1266–1268.

[44] Bojan Hiti. “Radiation Hardness of CMOS detector prototypes for ATLAS Phase-II ITk upgrade”. PhD thesis. Ljubljana U., 2020.

[45] B Hiti et al. “Charge collection in irradiated HV-CMOS detectors”. In: *Nuclear Instruments and Methods in Physics Research Section A: Accelerators, Spectrometers, Detectors and Associated Equipment* 924 (2019), pp. 214–218.

[46] B Hiti et al. “Charge collection properties in an irradiated pixel sensor built in a thick-film HV-SOI process”. In: *Journal of Instrumentation* 12.10 (2017), P10020.

[47] Eero Holmström, Antti Kuronen, and Kai Nordlund. “Threshold defect production in silicon determined by density functional theory molecular dynamics simulations”. In: *Physical Review B* 78.4 (2008), p. 045202.

[48] Frank Honniger. “Radiation damage in silicon. Defect analysis and detector properties”. In: (2008).

[49] M Huhtinen and PA Aarnio. “Pion induced displacement damage in silicon devices”. In: *Nuclear Instruments and Methods in Physics Research Section A: Accelerators, Spectrometers, Detectors and Associated Equipment* 335.3 (1993), pp. 580–582.

[50] Mika Huhtinen. “Simulation of non-ionising energy loss and defect formation in silicon”. In: *Nuclear Instruments and Methods in Physics Research Section A: Accelerators, Spectrometers, Detectors and Associated Equipment* 491.1-2 (2002), pp. 194–215.

[51] Daniel Hynds. *Silicon pixel R&D; for the CLIC detector*. Tech. rep. 2016.

[52] Abu Syed Md. Jannatul Islam. *Float Zone & Bridgman Crystal Crystal Growth Techniques*. 2019. URL: `https://www.slideshare.net/syedsumon/float-zone-bridgman-techniquessyed-kuet`.

[53] Canali Jacoboni et al. “A review of some charge transport properties of silicon”. In: *Solid-State Electronics* 20.2 (1977), pp. 77–89.

[54] W Kaiser. “Electrical and optical properties of heat-treated silicon”. In: *Physical Review* 105.6 (1957), p. 1751.

[55] Katharina Kaska and Robert Blumstr. “Characterization of radiation damage in detectors made from different silicon materials”. PhD thesis. Ph. D. dissertation, Faculty Phys., Tech. Univ. Wien, Wien, Austria, 2014.

[56] Charles Kittel and Paul McEuen. *Introduction to solid state physics.* Vol. 8. Wiley New York, 1976.

[57] Glenn F Knoll. *Radiation detection and measurement.* John Wiley & Sons, 2010.

[58] Gregor Kramberger. “Signal development in irradiated silicon detectors”. PhD thesis. Stefan Inst., Ljubljana, 2001.

[59] Gregor Kramberger. “Solid state detectors for high radiation environments”. In: *Detectors for Particles and Radiation. Part 2: Systems and Applications.* Springer, 2011, pp. 210–250.

[60] G Kramberger et al. “Annealing effects on operation of thin Low Gain Avalanche Detectors”. In: *Journal of Instrumentation* 15.08 (2020), P08017.

[61] G Kramberger et al. “Effective trapping time of electrons and holes in different silicon materials irradiated with neutrons, protons and pions”. In: *Nuclear Instruments and Methods in Physics Research Section A: Accelerators, Spectrometers, Detectors and Associated Equipment* 481.1-3 (2002), pp. 297–305.

[62] G Kramberger et al. “Inital acceptor removal in p-type silicon”. In: 2015.

[63] Olaf Krasel. “Charge collection in irradiated silicon detectors”. 2004.

[64] Maximo S Lazo, David M Woodall, and Patrick J McDaniel. “Silicon and silicon dioxide neutron damage functions”. In: *Proc. Fast Burt React. Workshop.* Vol. 1. 1987.

[65] V Lidroos et al. *Handbook of silicon based mems materials and technologies, Micro & Nano Tecnhologies Series.* 2010.

[66] Jens Lindhard, Morten Scharff, and Hans E Schiøtt. *Range concepts and heavy ion ranges.* Munksgaard Copenhagen, 1963.

[67] Gunnar Lindstroem et al. “Developments for radiation hard silicon detectors by defect engineering - results by the CERN RD48 (ROSE) Collaboration”. In: *Nuclear Instruments and Methods in Physics Research Section A: Accelerators, Spectrometers, Detectors and Associated Equipment* 465 (June 2001), pp. 60–69.

[68] Gunnar Lindström. “Radiation damage in silicon detectors”. In: *Nuclear Instruments and Methods in Physics Research Section A: Accelerators, Spectrometers, Detectors and Associated Equipment* 512.1-2 (2003), pp. 30–43.

[69] G Lindström et al. “Radiation hard silicon detectors - developments by the RD48 (ROSE) collaboration”. In: *Nuclear Instruments and Methods in Physics Research Section A: Accelerators, Spectrometers, Detectors and Associated Equipment* 466.2 (2001), pp. 308–326.

[70] CA Londos et al. “Effect of oxygen concentration on the kinetics of thermal donor formation in silicon at temperatures between 350 and 500 C”. In: *Applied physics letters* 62.13 (1993), pp. 1525–1526.

[71] Gerhard Lutz et al. *Semiconductor radiation detectors*. Springer, 2007.

[72] B Majeed et al. “Microbumping technology for hybrid IR detectors, 10μm pitch and beyond”. In: *2014 IEEE 16th Electronics Packaging Technology Conference (EPTC)*. IEEE. 2014, pp. 453–457.

[73] I Mandic and et al et. “E-TCT measurements with passive CMOS pixel detectors on RD50-MPW1 chips from LFoundry”. In: 33rd RD50 Workshop. 2018.

[74] I Mandic and et al et. “Irradiation study with passive CMOS pixel detector structures on RD50-MPW2 chips”. In: 37th RD50 Workshop. 2020.

[75] Igor Mandić et al. “Neutron irradiation test of depleted CMOS pixel detector prototypes”. In: *Journal of Instrumentation* 12.02 (2017), P02021.

[76] H McDuff et al. *Proton Irradiation Beam Profile Measurements*. 2013. URL: `http://physics.unm.edu/NUPAC_NMCPP/atlas_pixel/research/pages/documents/Beam_Profile_UNM.pdf`.

[77] Torbjørn Mehl et al. “Oxygen-related defects in n-type Czochralski silicon wafers studied by hyperspectral photoluminescence imaging”. In: *Energy Procedia* 124 (2017), pp. 107–112.

[78] M Moll. “Acceptor removal - Effects of displacement damage involving the shallow acceptor doping in p-type silicon devices”. In: Vertex 2019. Oct. 2019.

[79] Michael Moll. “Radiation damage in silicon particle detectors: Microscopic defects and macroscopic properties”. PhD thesis. DESY, 1999.

[80] Michael Moll, E Fretwurst, G Lindström, et al. “Leakage current of hadron irradiated silicon detectors–material dependence”. In: *Nuclear Instruments and Methods in Physics Research Section A: Accelerators, Spectrometers, Detectors and Associated Equipment* 426.1 (1999), pp. 87–93.

[81] LI Murin and VP Markevich. “Thermal double donors in silicon: a new insight into the problem”. In: *Early stages of oxygen precipitation in silicon*. Springer, 1996, pp. 329–336.

[82] Sofía Otero Ugobono. “Characterisation and Optimisation of Radiation-Tolerant Silicon Sensors with Intrinsic Gain”. PhD thesis. Santiago de Compostela U., 2018.

[83] A Ourmazd, W Schröter, and A Bourret. “Oxygen-related thermal donors in silicon: A new structural and kinetic model”. In: *Journal of applied physics* 56.6 (1984), pp. 1670–1681.

[84] Ivan Perić. “A novel monolithic pixelated particle detector implemented in high-voltage CMOS technology”. In: *Nuclear Instruments and Methods in Physics Research Section A: Accelerators, Spectrometers, Detectors and Associated Equipment* 582.3 (2007), pp. 876–885.

[85] Ivan Perić et al. “The FEI3 readout chip for the ATLAS pixel detector”. In: *Nuclear Instruments and Methods in Physics Research Section A: Accelerators, Spectrometers, Detectors and Associated Equipment* 565.1 (2006), pp. 178–187.

[86] Ioana Pintilie et al. “Radiation-induced point-and cluster-related defects with strong impact on damage properties of silicon detectors”. In: *Nuclear Instruments and Methods in Physics Research Section A: Accelerators, Spectrometers, Detectors and Associated Equipment* 611.1 (2009), pp. 52–68.

[87] *Private email exchange with STANDA.*

[88] R Radu et al. “Kinetics of cluster-related defects in silicon sensors irradiated with monoenergetic electrons”. In: *Journal of Applied Physics* 123.16 (2018), p. 161402.

[89] Simon Ramo. “Currents induced by electron motion”. In: *Proceedings of the IRE* 27.9 (1939), pp. 584–585.

[90] C Scharf, F Feindt, and R Klanner. “Influence of radiation damage on the absorption of near-infrared light in silicon”. In: *Nuclear Instruments and Methods in Physics Research Section A: Accelerators, Spectrometers, Detectors and Associated Equipment* 968 (2020), p. 163955.

[91] André Schöning et al. “MuPix and ATLASPix–Architectures and Results”. In: *arXiv preprint arXiv:2002.07253* (2020).

[92] E Fred Schubert. *Doping in III-V semiconductors.* E. Fred Schubert, 2015.

[93] Torsten Schulz. “Investigation on the long term behaviour of damage effects and corresponding defects in detector grade silicon after neutron irradiation”. PhD thesis. Hamburg U., 1996.

[94] Shyam Singh, Rajeev Singh, and BC Yadav. “Thermal donor formation in CZ-silicon with reference to dimers, trimers and V–O interaction”. In: *Physica B: Condensed Matter* 404.8-11 (2009), pp. 1070–1073.

[95] V. Sola. “Next-Generation Tracking System for Future Hadron Colliders”. In: The 28^{th} international workshop on vertex detectors. Oct. 2019.

[96] Helmuth Spieler. *Semiconductor detector systems.* Vol. 12. Oxford university press, 2005.

[97] M Stavola et al. “Diffusivity of oxygen in silicon at the donor formation temperature”. In: *Applied Physics Letters* 42.1 (1983), pp. 73–75.

[98] *Technical design report for the ATLAS Inner Tracker Pixel Detector.* 2017.

[99] N Alipour Tehrani et al. “Capacitively coupled hybrid pixel assemblies for the CLIC vertex detector”. In: *Nuclear Instruments and Methods in Physics Research Section A: Accelerators, Spectrometers, Detectors and Associated Equipment* 823 (2016), pp. 1–8.

[100] S Terzo et al. “Characterisation of AMS H35 HV-CMOS monolithic active pixel sensor prototypes for HEP applications”. In: *Journal of Instrumentation* 14.02 (2019), P02016.

[101] E Tuovinen et al. “Intentional thermal donor activation in magnetic Czochralski silicon”. In: *Materials science in semiconductor processing* 10.4-5 (2007), pp. 179–184.

[102] R Turchetta. “CMOS monolithic active pixel sensors (MAPS) for scientific applications”. In: (2003). DOI: `10.5170/CERN-2003-006.28`. URL: `https://cds.cern.ch/record/712036`.

[103] R Turchetta et al. “A monolithic active pixel sensor for charged particle tracking and imaging using standard VLSI CMOS technology”. In: *Nuclear Instruments and Methods in Physics Research Section A: Accelerators, Spectrometers, Detectors and Associated Equipment* 458.3 (2001), pp. 677–689.

[104] E Vilella Figueras, RD50 Collaboration, et al. “Recent depleted CMOS developments within the CERN-RD50 framework”. In: *The 28th International Workshop on Vertex Detectors. 13-18 October.* 2019, p. 19.

[105] E. Vilella et al. “Status of HV-CMOS developments within the RD50 collaboration”. In: 32nd RD50 Workshop. June 2018.

[106] Kazumi Wada. “United model for formation kinetics of oxygen thermal donors in silicon”. In: *Physical Review B* 30.10 (1984), p. 5884.

[107] Moritz Wiehe et al. “Development of a Tabletop Setup for the Transient Current Technique Using Two Photon Absorption in Silicon Particle Detectors”. In: *IEEE Transactions on Nuclear Science* (2020).

[108] Raymond N Williams and Ewan M Lawson. “The plasma effect in silicon semiconductor radiation detectors”. In: *Nuclear Instruments and Methods* 120.2 (1974), pp. 261–268.

[109] Martin Jacob Woudstra. “Precision of the ATLAS Muon Spectrometer”. PhD thesis. Amsterdam U., 2002.

[110] Chenfan Zhang et al. “Development of RD50-MPW2: a high-speed monolithic HV-CMOS prototype chip within the CERN-RD50 collaboration”. In: *Topical Workshop on Electronics for Particle Physics*. 2019, p. 45.

[111] Jing Zhang, Jun-Chao Ren, and Ding Liu. “Effect of crucible rotation and crystal rotation on the oxygen distribution at the solid-liquid interface during the growth of Czochralski monocrystalline silicon under superconducting horizontal magnetic field”. In: *Results in Physics* 13 (2019), p. 102127.